UNCLASSIFIED

AD NUMBER

AD904938

NEW LIMITATION CHANGE

TO

Approved for public release, distribution unlimited

FROM

Distribution authorized to U.S. Gov't. agencies only; test and evaluation; Oct 1972. Other requests shall be referred to AFWL [LRT], Kirtland AFB, NM, 87117.

AUTHORITY

AFWL ltr, 4 Jun 1976.

THIS PAGE IS UNCLASSIFIED

AFWL-TR-72-82

AFWL-TR-
72-82

AD904938

HYDROGEN FLUORIDE LASER TECHNOLOGY STUDY (CCN)

T. A. Jacobs et al.

TRW Systems Group

TECHNICAL REPORT NO. AFWL-TR-72-82

October 1972

AIR FORCE WEAPONS LABORATORY
Air Force Systems Command
Kirtland Air Force Base
New Mexico

Distribution limited to US Government agencies only because test and evaluation information is discussed in the report (Oct 72). Other requests for this document must be referred toAFWL (LRT), Kirtland AFB, NM, 87117.

AFWL-TR-72-82

AIR FORCE WEAPONS LABORATORY
Air Force Systems Command
Kirtland Air Force Base
New Mexico 87117

When US Government drawings, specifications, or other data are used for any purpose other than a definitely related Government procurement operation, the Government thereby incurs no responsibility nor any obligation whatsoever, and the fact that the Government may have formulated, furnished, or in any way supplied the said drawings, specifications, or other data, is not to be regarded by implication or otherwise, as in any manner licensing the holder or any other person or corporation, or conveying any rights or permission to manufacture, use, or sell any patented invention that may in any way be related thereto.

DO NOT RETURN THIS COPY. RETAIN OR DESTROY.

AFWL-TR-72-82

HYDROGEN FLUORIDE LASER TECHNOLOGY STUDY (CCN)

T. A. Jacobs et al.
TRW Systems Group

TECHNICAL REPORT NO. AFWL-TR-72-82

Distribution limited to US Government agencies only because test and evaluation information is discussed in the report (Oct 72). Other requests for this document must be referred to AFWL (LRT), Kirtland AFB, NM, 87117.

FOREWORD

This report was prepared by the TRW Systems Group, Redondo Beach, California, under Contract F29601-71-C-0070. The research was performed under Program Element 62601F, Project 3326, Task 0.

Inclusive dates of research were 9 November 1971 through 9 March 1972. The report was submitted 21 August 1972 by the Air Force Weapons Laboratory Project Officer, Captain William E. Thompson III (LRT).

The following personnel are also authors of this report: J. E. Broadwell; D. L. Hook; R. F. Wuerker; and F. N. Mastrup.

This technical report has been reviewed and is approved.

William E. Thompson, III

WILLIAM E. THOMPSON III
Captain, USAF
Project Officer

Raymond L. Oglukian

RAYMOND L. OGLUKIAN
Major, USAF
Chief, Advanced Technology Branch

Donald L. Lamberson

DONALD L. LAMBERSON
Colonel, USAF
Chief, Laser Division

ABSTRACT

In the course of performing the work discussed in this report, the basic feasibility of Rayleigh Scattering, Raman Scattering and Holographic Interferometry as HF/DF laser cavity diagnostic techniques was investigated. A new HF/DF chemical laser system designated CL III was designed, fabricated and underwent preliminary testing to evaluate reactant mixing of parallel, fully developed H_2 and F supersonic flows in the lasing cavity and scaling to higher power while maintaining good potential for pressure recovery.

(Distribution Limitation Statement B)

CONTENTS

Section		Page
I	INTRODUCTION AND SUMMARY	1
II	LASER CAVITY DIAGNOSTIC EVALUATION	5
	Rayleigh/Raman Scattering Diagnostic Techniques	5
	Holographic Interferometry Diagnostic Technique	23
III	LASER SYSTEM DESIGN	34
	CL III Cavity Injector Description	35
	Laser System Description	42
	Design Analyses	50
IV	EXPERIMENTAL EVALUATION	74
	Test Summary and Diagnostics	74
	Analysis of Diagnostic Data	78
	Power Measurements	87
V	CONCLUSIONS	90
	REFERENCES	92

ILLUSTRATIONS

Figure		Page
1	Rayleigh/Raman Scattering Geometry	8
2	Rayleigh/Raman Scattering Apparatus Schematic	14
3	Rayleigh Scattering Signal Strength vs Species Pressure at 22°C	16
4	Raman Scattering Signal Strength vs Species Pres Pressure at 22°C	17
5	Schematic Showing Xenon-Laser/Infrared/Visible Light Mapper Experiment	19
6	Functional Block Diagram	20
7	Schematic of Mach Zehnder Interferometer Used in Diagnosing Gas Flow	25
8	TRW Holocamera Apparatus Developed Under NASA Contract	31
9	Schematic Diagram of the Optical Train of the Transmission Holocamera Shown in Figure 8	32
10	Alternate Parallel Stream Mixing Concept	34
11	TRW CL III Combustion Driven Chemical Laser Cavity Injector	39
12	Partially Assembled CL III Injector	40
13	CL III Injector Assembly	40
14	CL III Cavity Injector Showing Nozzle Exit and Vortex Generators	40
15	CL III Propellant Schematic	43
16	Photograph Showing Plumbing of CL III Combustor Cavity Injector	44
17	CL III Laser Coolant Water Schematic	46
18	Installation of CL III Laser in Cavity Box	47
19	Closeup of CL III Laser in Cavity Box	47
20	Mirror Mount	48
21	20% Hole Outcoupled Flat Mirror	48

ILLUSTRATIONS (Continued)

Figure		Page
22	Mirror Enclosure Mounting	49
23	TRW Cone Calorimeter Installation	50
24	Cavity Fuel Injector, Throat Area vs ψ	52
25	Cavity Fuel Injector Parametric Studies	53
26	Cavity Oxidizer Injector, Throat Area vs ψ	54
27	Oxidizer Cavity Injector Parametric Studies	55
28	Cavity Oxidizer Injector (N_2 Diluent) Throat Area vs ψ	56
29	Cavity Oxidizer Parametric Studies, N_2 Diluent	57
30	Effect of Velocity Ratio on Spreading Rate	60
31	Typical Hypothetical Spreading Angles	62
32	CL II Heat Loss/Total Weight Flow Correlation	64
33	Cavity Injector Sidewall Thermal Model	68
34	Cavity Injector Throat Thermal Model	69
35	Cavity Injector Backwall Thermal Model	70
36	Mechanical Properties of OFHC After Braze Cycle	71
37	Fatigure Cycle Life of OFHC Copper, Post-Braze Cycle	72
38	IR Intensity Distribution—Test 319, Set 1	97
39	IR Intensity Distribution—Test 319, Set 1 (every 10th scan line)	98
40	IR Intensity Distribution—Test 319, Set 2	99
41	IR Intensity Distribution—Test 319, Set 2 (every 10th scan line)	100
42	IR Intensity Distribution—Test 320, Set 1	101
43	IR Intensity Distribution—Test 320, Set 1 (every 10th scan line)	102
44	IR Intensity Distribution—Test 320, Set 2	103

ILLUSTRATIONS (Continued)

Figure		Page
45	IR Intensity Distribution—Test 320, Set 2 (every 10th scan line)	104
46	IR Intensity Distribution—Test 321, Set 1	105
47	IR Intensity Distribution—Test 321, Set 1 (every 10th scan line)	106
48	IR Intensity Distribution—Test 321, Set 2	107
49	IR Intensity Distribution—Test 321, Set 2 (every 10th scan line)	108
50	IR Intensity Distribution—Test 322, Set 1	109
51	IR Intensity Distribution—Test 322, Set 1 (every 10th scan line)	110
52	IR Intensity Distribution—Test 322, Set 2	111
53	IR Intensity Distribution—Test 322, Set 2 (every 10th scan line)	112
54	IR Intensity Distribution—Test 323, Set 1	113
55	IR Intensity Distribution—Test 323, Set 1 (every 10th scan line)	114
56	IR Intensity Distribution—Test 323, Set 2	115
57	IR Intensity Distribution—Test 323, Set 2 (every 10th scan line)	116
58	Schematic IR Intensity Profile in CL III Flow Field	77
59	IR Intensity Profiles, Test 319	79
60	IR Intensity Profiles, Test 321	79
61	IR Intensity Profiles, Test 322	80
62	IR Intensity Profiles, Test 323	80
63	Visible Light Photo of Test 341	81
64	IR Scan of Test 319 in Video Mode	81
65	Visible Light Photo of Test 342	82
66	IR Scan of Test 321 in Video Mode	82

ILLUSTRATIONS (Continued)

Figure		Page
67	Visible Light Photo of Test 341, Side View	83
68	Visible Light Photo of Test 342, Side View	83
69	Concentration Profile Across Mixing Zone	85
70	Typical H_2 Heater Nozzle Cross Section Schematic	88

TABLES

Table		Page
I	TRW Xenon Laser	15
II	Raman/Rayleigh Signal Strengths (amp/torr)	17
III	Optics Parameters	18
IV	Calibration Factors	21
V	Interferometer Constants of Gases of Interest to HF Chemical Lasers	27
VI	Average Fringe Shift Expected in an HF Chemical Laser at 0.6943μ	29
VII	Potential CL III Operating Conditions	38
VIII	Boundary Layer and One-Dimensional Mixing Calculation Results (150 psia combustor pressure)	94
IX	Boundary Layer and One-Dimensional Mixing Calculation Results (75 psia combustion pressure)	95
X	Chemical Laser Design Study	63
XI	Estimated Heat Losses for CL II, Case I (Btu/sec)	66
XII	Summary of CL III Test Results	96
XIII	Summary of Principal Diagnostics Taken in Initial Test Series and Significant Flow Conditions	75

NOMENCLATURE

Except where otherwise noted in the text, the symbols used have the meaning, value and units as given below.

a_o	Velocity of sound $\sqrt{\frac{\gamma RT}{N}}$	cm/sec
A	Area of cross section or component	cm^2, $in.^2$
C	Velocity of light (3×10^{10})	cm/sec
e	Denotes the exponential function	
e	Electron charge (1.6×10^{-19})	coulomb
G	Detector gain	
h	Planck constant (6.62×10^{-27})	erg sec
H_f	Heat of formation	Kcal/mole
I	Emission intensity	watt/cm^2-sterad
K	Gladstone Dale constant	cm^3
ℓ	Length along line of sight	
L	Length	
$\dot{m}$	Mass flow rate	gm/sec
M	Mach number	
n	Refractive index	
$\dot{n}$	Molar flow rate	moles/sec
N	Molecular weight or number density	gm/mole
p	Pressure	
p_c	Combustion chamber pressure	psia
p_i	Partial pressure	
p_L	Laser cavity static pressure	torr
Q	Heat transfer rate	btu/sec
R	Laser molar flow ratio (definition specific to subscript) or gas constant	

S	Fringe shift parameter	fringes/cm-atmos
S_λ	System response at wavelength λ	volts/watt cm^{-2} $ster^{-1}$
t	Throat Width	
T	Temperature	^oK
u	Velocity	cm/sec
V	Velocity	ft/sec
x, y, z X, Y, Z	Spatial co-ordinates	cm
α	Fractional F_2 dissociation	
α	Mixing angle	
α_i	Polarizability	
β	Combustion chamber diluent ratio	
γ	Ratio of specific heats	
γ	Molecular anisotropy factor	
δ	Boundary layer thickness	
δ^*	Boundary layer displacement thickness	
δ_t	Boundary layer thermal thickness	
Δ	Denotes the difference of two relatable quantities	
ϵ	Emissivity	
θ	Angular notation	
λ	Wavelength	cm
μ	Viscosity	
ρ	Mass density	
ρ_n	Depolarization factor	
σ	Scattering coefficient	
χ	Mole fraction	
ψ	Combustion chamber diluent ratio	

ω	Solid angle notation	
[HF]	Concentration of species	moles/cm^3
<>	Mean value of parameter evaluated across flow section	

Subscripts:

B	Boundary layer
c	Plenum chamber parameter
e	External to boundary layer
ex	Exit conditions
L	At nozzle exit or cavity
m	Properties of mixture
o	Reference condition
s	Standard conditions
t	Translational, total, or throat parameter
w	At nozzle wall

Superscripts:

*	At nozzle throat or excited species
-	Averaged or mean conditions
'	Modified definition

SECTION I

INTRODUCTION AND SUMMARY

This report presents the results of progress made on several key tasks which were added to the basic "HF Laser Technology Study," Contract No. F29601-71-C-0070. These tasks include:

Task I: Investigate the feasibility of the following diagnostic techniques for possible application to HF/DF laser cavity evaluation:

- Rayleigh scattering measurements from a high power Xe-laser to determine local cavity density distribution.
- Raman scattering measurements from a high power Xe laser to determine scattering strength and practicality of this technique for determining F_2 and H_2 cavity concentrations.
- Holographic interferometry techniques to determine the optical quality of the lasing media as far as density gradients are concerned.

Task II: Design and fabricate a new laser system (CL III) which is configured to produce fast mixing of reactants in the laser cavity in an understandable manner.

Task III: Provide testing at the TRW Capistrano Test Site to evaluate the performance of the new CL III laser system. The testing will study, principally, the lasing zone produced by the new cavity injector in an attempt to understand how turbulent mixing affects the HF lasing potential. Infrared mapping, visible light photography and closed cavity power measurement will be employed to study mixing and lasing characteristics.

In performing the above tasks, significant progress was made in better understanding the laser medium and its influence on hardware design and testing methods. The basic feasibility of Rayleigh/Raman scattering techniques to measure concentrations of molecular hydrogen and molecular fluorine in HF/DF laser cavities was established through analyses and laboratory experiments. By using a xenon UV laser and modifying existing scanner equipment, detection sensitivities on the order of 4×10^{-2} torr could be achieved for the above indicated species. However, helium appears not to be detectable with current apparatus.

Holographic interferometry appears to be a viable cavity diagnostic technique when employed on larger chemical laser devices where the optical path length is on the order of 1 meter. However, the method has marginal utility, i.e., it produces extremely small fractions of a fringe, when used in conjunction with current, smaller chemical laser systems unless modifications are made to existing interferometry devices and techniques to extend the state of the art. This is caused principally by the relatively short optical path length and very low density gases in the lasing region of the smaller laser devices.

The CL III laser hardware designed and fabricated in conjunction with this program represented a first attempt to deal with the problem of rapid mixing and scaling of the HF/DF chemical laser to a high power device while at the same time achieving good downstream pressure recovery potential. Initial parametric analyses were performed over a wide range of operating conditions. A baseline design was then selected and detailed fluid mechanical, thermal and stress analyses were performed. The following criteria were employed in the design:

- Provision to allow varying velocities of the H_2 and F jets as well as a range of nozzle exit temperature and diluent ratios
- Capability of supplying preheated H_2 at high Mach number and velocity
- Combustion pressures in excess of 100 psia to provide a flow field consistent with pressure recovery requirements
- Cavity injector nozzles designed to account for boundary layer buildup; the area ratios increasing as dictated by an analysis of boundary layer thickness
- Nozzle area ratios designed to closely match the exit pressure to the expected cavity pressure
- The lasing zone confined within a suitable lasing cavity to prevent entrainment and recirculation of ground state HF into the supersonic flow stream.

The CL III hardware as designed utilizes two combustion chambers, one for producing atomic fluorine and the other for preheating molecular hydrogen. Deuterium and fluorine mixed with appropriate quantities of helium or nitrogen diluent are injected into each combustor to produce

the required high temperature gas flows. A single 1.5 by 8-inch nozzle bank employing 23 nozzles is connected to the two combustion chambers by separate plenums. Thus, alternate adjacent nozzles flow F- and H_2-containing streams. Exit velocity ratios of F to H_2 varying from 0.59 to 2.6 can be obtained with this hardware by varying the combustor conditions.

Twenty-five tests were performed at the Capistrano Test Site using the CL III hardware. These tests involved checkout of the CL III cavity injector and separate combustor hardware followed by a series of test runs to evaluate the effects of varying F and H_2 stream velocities within the range indicated above. IR mapping and orange glow photography were used as laser cavity diagnostics in this initial test series. Several runs were made to assess laser power using hole outcoupled mirrors.

The output power of the device was disappointingly low, less than 500 watts. Three fundamental causes have been identified.

First, analyses of the CL III cavity diagnostic data revealed that very little IR or visible radiation emission occurred directly downstream of the hydrogen nozzles in any of the runs observed. On the other hand, the intensity within the fluorine jets began to rise almost immediately. The intensity then leveled out at the fluorine jet centerline approximately 2-1/2 inches downstream of the nozzle exit plane and remained nearly constant for at least another 3 inches downstream. The conclusion drawn from these data was that the gross rate of mixing within the fluorine jet was approximately equal to that predicted from previous subsonic experiments. However, microscale mixing within the turbulent zone is not well known and could be sufficiently slow to cause the observed extended reaction zone thus adversely affecting the lasing action.

Second, in a post-test calibration, the fluorine sonic flow control orifice was found to be in error by approximately five percent leading to excessive F_2 flow into the hydrogen heater combustor. The excess F_2 undoubtedly reacted with H_2 injected downstream ahead of the nozzle throat, leading to the introduction of relatively large quantities of ground state HF with the H_2 stream into the laser cavity. This situation was further aggravated by combustor injector flow maldistribution. Based

upon empirical observation of the quantity of ground state HF introduced into the prior CL II device when operated in the HF/HF mode, and the calculated quantity introduced as a result of the CL III calibration problems, it is believed that sufficient ground state was injected to account for the low powers observed. Additional testing is required to confirm this hypothesis.

Third, in this initial test series the maximum hydrogen temperature achieved in the nozzle plenum was less than 1100°K to avoid any possibility of HF/DF isotope exchange. This resulted in a laser cavity static temperature after mixing, but prior to the lasing reaction of only 150°K. Extrapolation of measured kinetics data taken at 350°K to the 150°K condition, revealed that production to deactivation rates of HF* were unfavorable for lasing.

Further work is required to thoroughly assess each of the above-mentioned factors. Subsequent testing with chemiluminescent spectroscopy diagnostics is recommended under the HF Technology Follow-On Contract No. F29601-72-C-0077, and the Reactive Flow Study Contract No. F29601-72-C-0021, to understand and correct the deficiencies observed in the initial test series and to further investigate the CL III laser system.

SECTION II

LASER CAVITY DIAGNOSTIC EVALUATION

Measurement of laser cavity flow field characteristics such as local kinetic temperature, pressure, velocity, local species concentration and species excitation is essential in deriving the understanding required for guiding the design of scaled up advanced HF/DF chemical lasers. The first task of the subject program entailed feasibility evaluation and conduct of laboratory tests, where applicable, of cavity flow field visualization and property diagnostic techniques which had not been previously applied to chemical lasers. The three new possible cavity diagnostic techniques considered were:

- Rayleigh scattering using a xenon laser for local cavity bulk number density measurements
- Raman scattering using a xenon laser to measure cavity molecular species concentrations (H_2 and F_2)
- Holographic interferometry to assess the spatial distribution of cavity density gradients

The following sections present a detailed discussion of the physical concepts involved with each diagnostic technique, previous experience with the techniques, and an evaluation of the applicability of the technique for a field-test apparatus for high power chemical lasers.

1. RAYLEIGH/RAMAN SCATTERING DIAGNOSTIC TECHNIQUES

In previous chemical laser cavity measurement programs (Ref. 1), diagnostics by chemiluminescence and resonance absoprtion spectroscopy and by IR-intensity mapping of the entire flow field have yielded valuable and extensive insight into HF-laser cavity flow field structure, HF excited state and ground state distributions. This progress in understanding brought about by the early diagnostics has led to new questions which cannot be approached by the diagnostic techniques described above. More specifically, the above-indicated measurements are not suited to provide data on local concentrations of homonuclear molecules such as F_2, H_2, D_2. Even for heteronuclear molecules HF and DF, the chemiluminescent or absorption data yield line-of-sight integrated

population densities (molecules/cm^2) as direct observables. Further measurements or assumptions are required in order to reduce these data to truly local species densities.

Coherent scattering of laser radiation by molecules has been shown to be a practical tool for measurement of local molecular species concentrations applicable both to homonuclear and heteronuclear molecules. By proper arrangement of exciting and observing optics coherent scattering is also principally capable of providing truly local concentration measurements. The general disadvantage of coherent scattering is the usually very low scattering cross section, requiring powerful laser radiation for an exciting light source. Such laser sources have become available during the last decade. Other difficulties with all coherent scattering techniques are interference problems, generally requiring very careful optical design to achieve acceptable signal/noise values. Both problems with scattering measurements have been largely solved during the last years to the point where it is quite reasonable to expect sensitivities adequate for detecting species concentrations substantially below 1 torr partial pressures; this makes the scattering technique of interest in the diagnostics of laser cavities.

Coherent scattering of visible and ultraviolet light by atoms and molecules is related to the property of polarizability of the atomic or molecular electron cloud. Rayleigh scattering intensities are directly proportional to the square of the average polarizability. In the case of molecules, the polarizability may change during the vibrational and rotational motion of the molecules giving rise to a vibrational and rotational Raman effect. Contrary to the case of Rayleigh scattering, Raman scattering produces wavelength shifts which are clearly characteristic of the molecule. Raman scattering is therefore particularly useful for species concentration measurements. If the exciting wavelength is chosen close to (but not identical to) a molecular electronic resonance, Raman scattering intensities are observed to increase substantially; in this case the effect is frequently referred to as Resonance Raman Effect (RRE).

Coherent scattering intensities are directly proportional to laser power and inversely proportional to the fourth power of the exciting wavelength. This wavelength dependence of coherent scattering intensities

affects in a significant way the choice of the exciting laser. For non-resonance coherent scattering, a useful figure of merit for comparing different lasers is

$$P/\lambda^4 \tag{1}$$

where P is the laser power and λ is laser wavelength. Resonance wavelengths for laser cavity species H_2, D_2, HF, H, D, He and F are all substantially below 0.2μ whereas available lasers of acceptable power output and reliability oscillate at wavelengths in excess of 0.3μ. The above cited laser figure of merit is therefore applicable for choosing the best laser for the above indicated species. Comparing all available lasers considering wavelength, power, stability, compactness and ruggedness, two lasers appear most applicable; these are the xenon UV laser ($\lambda = 0.3645\mu$) and the nitrogen laser ($\lambda = 0.3315\mu$). The difference in figure of merit of these two lasers is negligible considering presently available power levels. Because of TRW's experience with Xe-lasers we chose to base all our work on this particular laser.

The specific objective of the Rayleigh/Raman scattering diagnostic techniques evaluation was to assess the utility of this method for determining local laser cavity bulk and species number densities. Rayleigh scattering strengths are expected to be useful for measuring local bulk densities, particularly if relative gas compositions are well known. Raman scattering as a technique is specific to the scattering molecule and can therefore be used to measure local specie densities. Of special interest is the measurement of F_2 and H_2 in laser cavities.

a. Theoretical Background and Calibration Equations

The following discussion of the theoretical aspects of the scattering phenomena is presented in two parts; the first relating to Rayleigh scattering; the second relating to Raman scattering. Special consideration is given to developing the calibration equations necessary for use in a field test diagnostic apparatus. The exciting laser of interest is Xe, $\lambda = 0.3645\mu$, although most of the formalism presented below will generally apply to other wavelengths as well.

(1) Rayleigh Scattering Intensities

Rayleigh scattering intensities depend upon molecular polarizabilities, the exciting wavelength, the direction of scattering, and, in a fairly complex fashion, on the state of polarization of the incident beam.

In the treatment of Rayleigh scattering, the approach of S. Chandrasekhar (Ref. 2) is followed. Consider an incident beam of light characterized by a set of Stokes parameters $\{I_{\parallel}, I, U, V\}$ forming a four vector. The scattered radiation (I'), intensity and polarization can be determined from

$$\epsilon' \, d\omega' = \left(\sigma \frac{d\omega'}{4\pi}\right)(R)(I) \, d\omega \text{ watt/particle} \tag{2}$$

where the meaning of ϵ' is the four vector emissivity of the scattered radiation; $d\omega'$ is the solid angle subtended by the detector optics; (R) is the scattering tensor (4 by 4 matrix); (I) is the four vector incident intensity (watt/cm^2 sterad); and $d\omega$ is the divergence (solid angle) of the incident xenon laser beam. The scattering geometry is illustrated in Figure 1.

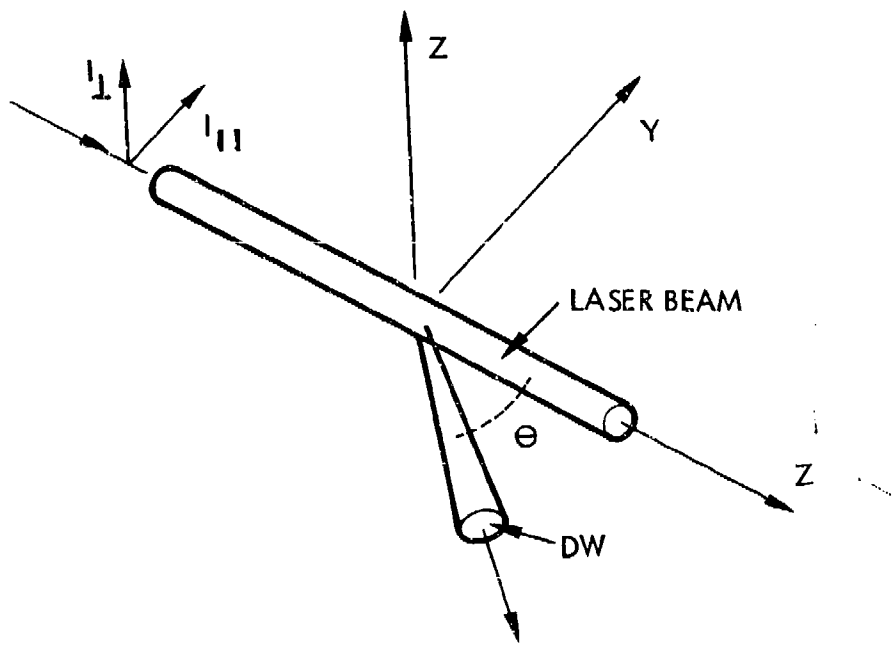

Figure 1. Rayleigh/Raman Scattering Geometry

The scattering matrix R is

$$(R) = \frac{3}{2(1+2\gamma)} \begin{pmatrix} \cos^2\theta + \gamma \sin^2\theta & \gamma & 0 & 0 \\ \gamma & 1 & 0 & 0 \\ 0 & 0 & (1-\gamma)\cos\theta & 0 \\ 0 & 0 & 0 & (1-3\gamma)\cos\theta \end{pmatrix} \tag{3}$$

where γ is a factor related to the molecular anisotrophy. For isotropic scattering, as in the case of most atoms, the anisotrophy factor is zero. It can further be shown that for anisotropic scattering, $\gamma \leq 1/3$. The scattering coefficient σ in equation (2) for anisotropic scattering can be written as

$$\sigma_i = \frac{128\pi^5}{3\gamma^4} \alpha_i^2 \frac{3(2+\rho_n)}{6-7\rho_n} \text{ cm}^2/\text{particle} \tag{4}$$

where the depolarization factor ρ_n is defined by

$$\rho_n = \frac{2\gamma}{1+\gamma} \tag{5}$$

and α_i is the polarizability. Because of the restrictions on values for γ it can be readily verified that the range of possible values for the depolarization factor ρ_n is given by

$$0 \leq \rho_n \leq \frac{1}{2}$$

Assume a Xe laser beam power P (watts) and laser beam cross sectional area A. Then

$$(I\, d\omega) = \frac{P}{A} \text{watt/cm}^2$$

Assume further that the radiometer optics views a length of the laser beam ℓ defining a viewing volume of

$$V = A \cdot \ell \text{ cm}^3$$

Let n_i be the local number density of species i. The total number of scatterers in the viewing volume is therefore $V \cdot n_i$ molecules. The total power scattered into the viewing optics is therefore

$$P' \, d\omega' = \sigma_i \frac{d\omega}{4\pi} \cdot n_i \cdot \ell \, (R) \cdot (P) \text{ watt} \tag{6}$$

The viewing optics solid angle $d\omega'$ can be readily determined from the radiometer aperture area and the distance and ℓ is dictated by the desired spatial resolution. Equation (6) fully describes both the polarization and power of the Rayleigh scattered radiation. For practical consideration, equation (6) can be significantly simplified provided we assume henceforth that all observations are conducted with linearly polarized laser light at scattering angles of 90 degrees. For this special case, the scattering matrix reduces to

$$(R) = \frac{3}{2(1 + 2\gamma)} \begin{pmatrix} \gamma & \gamma & 0 & 0 \\ \gamma & 1 & 0 & 0 \\ 0 & 0 & 0 & 0 \\ 0 & 0 & 0 & 0 \end{pmatrix}$$

In this case the parallel and perpendicular component of the scattered radiation are

$$P'_{\parallel} \, d\omega' = \sigma_i \frac{d\omega}{4\pi} \cdot n_i \cdot \ell \frac{3}{2(1 + 2\gamma)} (P_{\parallel} + P_{\perp})\gamma \text{ watt} \tag{6a}$$

$$P'_{\perp} \, d\omega' = \sigma_i \frac{d\omega}{4\pi} \cdot n_i \cdot \ell \frac{3}{2(1 + 2\gamma)} (\gamma P_{\parallel} + P_{\perp}) \text{ watt} \tag{6b}$$

where $P_{\parallel}$ and $P_{\perp}$ are the parallel and perpendicular components of the incident laser power and $P'_{\parallel}\, d\omega'$ and $P'_{\perp}\, d\omega'$ the corresponding components of the scattered radiation. The total Rayleigh scattered laser power is

$$P'\, d\omega' = (P'_{\parallel} + P'_{\perp})\, d\omega'$$

$$= \sigma_i \frac{d\omega'}{4\pi} n_i \cdot \ell \frac{3}{2(1+2\gamma)} \{(\gamma+1)P_{\perp} + 2\gamma P_{\parallel}\} \text{ watt} \tag{6c}$$

Specializing further to the case where the laser beam plane of polarization is arranged such that $P_{\parallel} = 0$ and $P_{\perp} = P$, then

$$P'\, d\omega' = \sigma_i \frac{d\omega'}{4\pi} n_i \cdot \ell \cdot \frac{3(\gamma+1)}{2(1+2\gamma)} P \text{ watt} \tag{6d}$$

It is practical to introduce into equation (6d) observables such as pressures, temperatures, receiver optics transmission T_{λ} and detector sensitivity, S_{λ} (amps/watt). The observable scattering signal current follows then as

$$i_i = A_i \frac{p_i}{p_s} \frac{T_s}{T_i} \cdot P \cdot \ell \cdot d\omega'\, T_{\lambda} S_{\lambda} \text{ amps} \tag{7}$$

where i_i is the Rayleigh signal strength (amps of PM-tube) and the constant A_i is

$$A_i = \frac{\sigma_i}{4\pi} N_o \frac{3(\gamma+1)}{2(1+2\gamma)} \; ; \; N_o = 2.69 \times 10^{19} \text{ molecules/cm}^3$$

p_i is the partial pressure of species i, T_i the temperature and p_s and T_s are standard pressure and temperature. Specifically, at a reference pressure and temperature p_o and T_o the signal current is

$$\frac{i_o}{p_o} = \frac{A_i}{p_s} \frac{T_s}{T_o} \cdot (P \cdot \ell\, d\omega'\, T_{\lambda} S_{\lambda})_o \text{ amps/torr} \tag{8}$$

equation (8) can be conveniently used as a calibration equation. Using our convention for choosing the plane of polarization of the incidence beam and the angle of observation, the Rayleigh scattering signal in a laser cavity from a given species is

$$i = p \frac{T_o}{T} \frac{(P \cdot \ell \, d\omega' \, T_\lambda S_\lambda)}{(P \cdot \ell \, d\omega' \, T_\lambda S_\lambda)_o} \frac{i_o}{p_o} \text{ amps} \tag{9}$$

where the subscripts o refer to the known calibration following equation (8).

(2) Raman Scattering Intensities

Raman scattering is of particular interest to the detection of F_2, H_2, and HF in laser cavities. Although Raman scattering intensities are generally significantly lower than Rayleigh scattering and exhibit characteristic wavelength off-sets from the incident radiation, these two coherent scattering phenomena are closely related and depend on similar physical parameters. Without any further detailed discussion, it is therefore evident that the same calibration equation (8) can be used for Raman scattering signal strength predictions provided the calibration factor i_o/p_o now refers to Raman scattering strength rather than to Rayleigh scattering.

Contrary to the case of Rayleigh scattering, the Raman scattering produces a spectrum specific of the scattering molecule. We are here primarily interested in the vibrational Raman spectrum. The Stokes lines appear at longer wavelengths than the exciting wavelength, corresponding to subtracting the energy of a vibration-rotation quantum from the incident photon. Correspondingly, the anti-Stokes line photons have energy larger than the exciting photons by the amount of a vibration-rotation quantum. Anti-Stokes lines can only be observed if the scattering gas contains molecules in excited states. Therefore, measuring intensity ratios of Stokes to anti-Stokes lines provides data on ratios of excited state to ground state populations.

Assuming exciting laser radiation at frequency γ_o and power P (watts) incident on a concentration n_i (cm^{-3}) then the Raman scattered intensity $P_2' \, d\omega'$ watts at frequency ($_o$ -) and into a solid angle d ' at right angles with the laser beam direction is given by

$$P_2' \, d \; ' = 8\pi^4 P(\nu_o - \nu)^4 \cdot n_i \cdot \ell \cdot \frac{h}{8\pi^2 \mu c \omega} \left(\alpha'^2 + \frac{7}{45} \gamma'^2 \right) \cdot d\omega' \text{ watts}$$

where ℓ is the length of the observed laser beam, μ, ω are the reduced mass and vibrational frequency for the scattering molecules, and α', γ' are the derivatives of the spherical and anisotropic polarizabilities, respectively. This formula assumes the laser radiation to be plane polarized and the vibration-rotation structure of the Raman spectrum to be unresolved. Predominantly, then the equation gives the total intensity of the Q branch of the Raman spectrum.

b. Laboratory Measurements of Raman/Rayleigh Scattering Strength

The Raman/Rayleigh scattering efficiencies for the species F_2, H_2, and He were measured relative to N_2 as a reference in the laboratory experimental apparatus shown schematically in Figure 2. The laser source is a TRW developed pulsed xenon laser emitting a strong UV line at 0.3645μ. The laboratory data were obtained with the laser paramet rs as given in Table I.

This laser has also been operated at pulse repetition rates up to 200 pps for an average power of 0.3 watt, and it is anticipated that the system is capable of more than 1 watt average power with minor modification.

Output of the laser is continuously monitored by means of a dielectric beam splitter (98 to 2 percent) which transmits part of the laser beam to a photodiode with suitable neutral density and bandpass filters. The complete photodiode monitor system was calibrated directly against a standard tungsten radiation source.

The reflected component of the laser beam is focused into a scattering test chamber containing the species of interest and is collected by a Wood's horn light trap. As shown in Figure 2, the laser beam passes

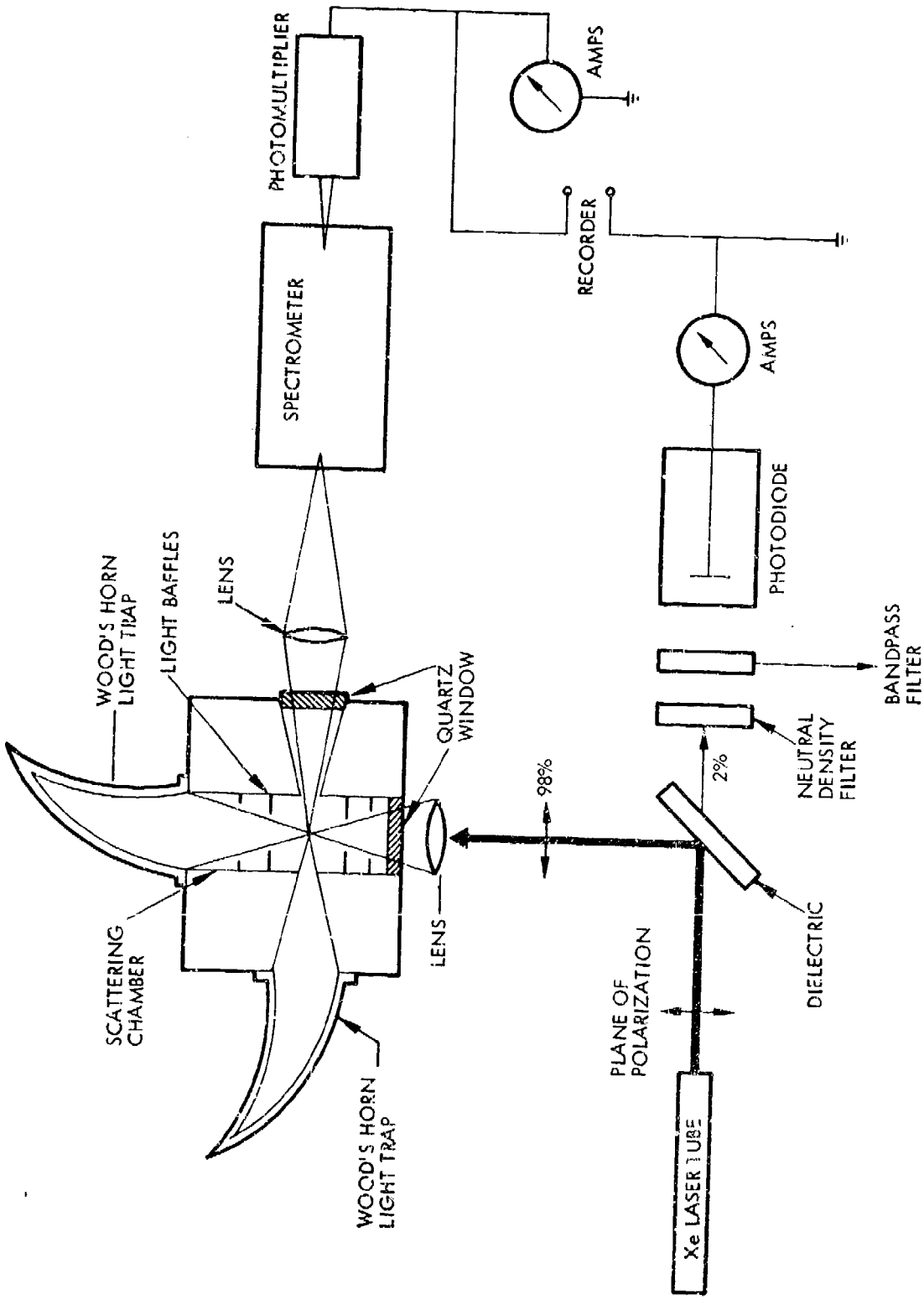

Figure 2. Rayleigh/Raman Scattering Apparatus Schematic

Table I. TRW Xenon Laser

Wavelength	0.3645μ
Peak Pulse Power	3 kw
Pulse Length	0.5 μsec
Pulse Repetition Rate	50 pps
Average Power	0.075 watt
Beam Diameter	5 mm
Plane Polarized (vertical)	–

vertically through the scattering chamber with the plane of polarization in the plane of the schematic drawing. However, the scattering chamber and spectrometer optics are shown rotated 90 degrees so that the Raman/Rayleigh scattered intensities are, in fact, measured in the direction normal to the laser beam and the plane of polarization.

Light scattered from the laser beam is focused onto the entrance slit of the single pass spectrometer and the scattered intensity is measured by means of a low noise photomultiplier (EMI 62565). The second Wood's horn opposite to the spectrometer and the light baffles in the laser beam path are to reduce the background light intensity (at 0.3645μ) caused by surface reflections to a minimum. It has been estimated that the background intensity contributed from all sources other than the gas scattering molecules is equivalent to 1 part in 10^{11} of the input laser intensity.

For the laboratory measurements, both the beam monitor and scattered signal currents were measured as conventional dc currents using a time constant of the order of 1 second to integrate the laser beam and scattered light pulses. In this mode of operation the sensitivity for Raman intensities measurements is limited by the photomultiplier dark current and electronics noise. However, it is readily shown that the scattering efficiencies can be determined at relatively high laboratory species concentrations, and that an improvement in signal-to-noise ratio of the order 10^4, and hence in species sensitivity, can be obtained by adopting the pulsed photon counting rate with synchronous detection.

For each species of interest the photodiode monitor current and scattered signal current were measured in terms of dc ampere as a function of pressure. For the species N_2, H_2 and He the pressures ranged from a value sensibly zero to 70 psia. Repeat tests generally agreed to within 5 percent in each case; Figures 3 and 4 show good linearity in the relationship of the Rayleigh and Raman scattered signal currents, respectively, as a function of the test chamber pressure. Error bars show the estimated confidence in these results. In all cases the data were normalized to a constant laser monitor current of 3×10^{-7} amperes corresponding to the typical operating parameters given in Table I.

In the case of F_2, the pressures used ranged from zero to 4 psia which was sufficient to obtain scattered signal strength comparable to the

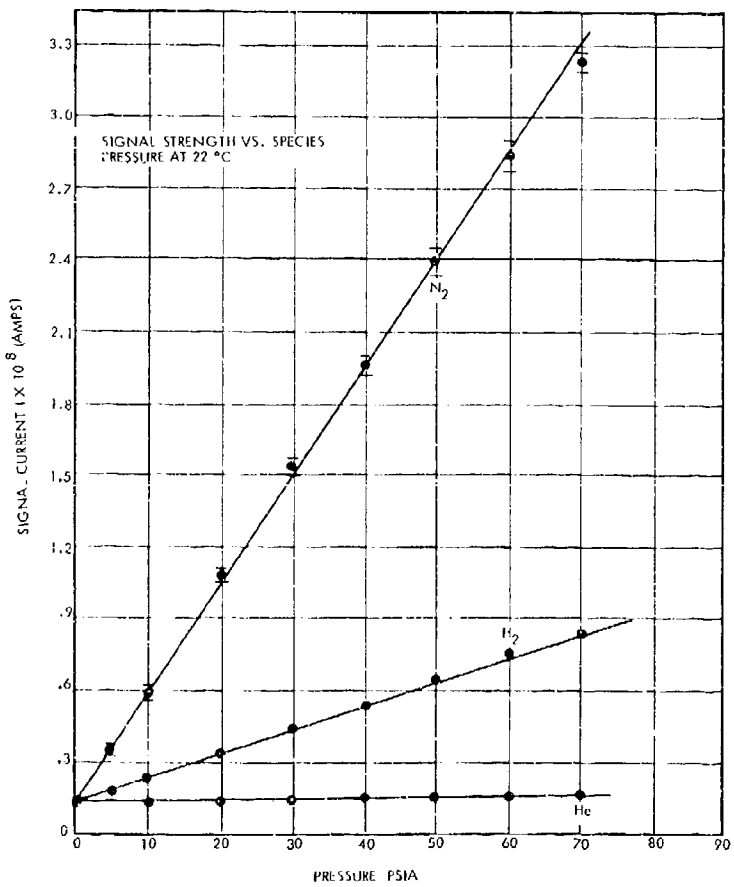

Figure 3. Rayleigh Scattering Signal Strength vs Species Pressure at 22°C

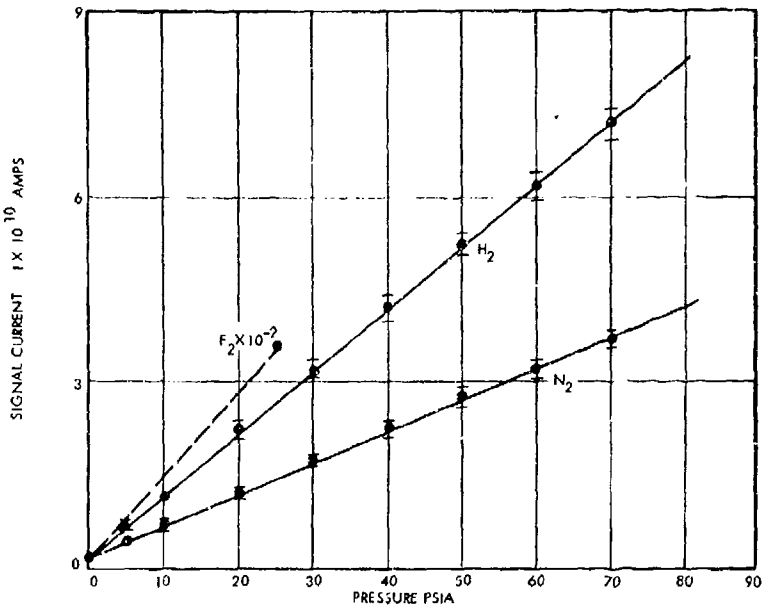

Figure 4. Raman Scattering Signal Strength vs Species Pressure at 22°C

other species at the high pressures. The enhanced scattering efficiency of the F_2 molecule is attributable to the resonance Raman effect which had been anticipated in view of the proximity of the F_2 absorption band to the xenon laser wavelength.

Table II summarizes the Raman/Rayleigh scattering data in the form of the expected signal current for a species concentration equivalent to 1 torr at normal room temperature (22°C).

Table II. Raman/Rayleigh Signal Strengths (amp/torr)

Species	Raman	Rayleigh
Hydrogen	1.9×10^{-13}	1.9×10^{-11}
Nitrogen	10.0×10^{-14}	8.7×10^{-11}
Helium	–	9.7×10^{-13}
Fluorine	$\sim 2.6 \times 10^{-11}$	

These data are specific to the optical system used in the laboratory measurements for which the parameters are given in Table III.

c. Chemical Laser Cavity Measurement Sensitivity

The laboratory data presented earlier can be used to determine directly the sensitivity of a Rayleigh/Raman scattering system for potential use on a CL-III or other chemical laser cavity. The envisioned system consists of the existing IR scanner modified with a radiometer spectrometer detector and a 1-watt UV Xe-laser as shown schematically in Figure 5. A functional block diagram of the complete diagnostic measurement system is presented in Figure 6. The desired spatial resolution is 1 mm in the cavity. From equation (8) the sensitivity for detecting a species i in the laser cavity by Rayleigh or Raman scattering is

$$(i/p) = \frac{(P \cdot \ell \cdot d\omega' \, T_\lambda S_\lambda)}{(P \cdot \ell \cdot d\omega' \, T_\lambda S_\lambda)_o} \cdot \frac{T_o}{T_s} \cdot (i/p)_o \text{ amp/torr}$$

Here the calibration factors $(i/p)_o$ amp/torr are those determined from the calibration experiment and listed in Table II.

The laser power used in the calibration experiment was 0.075 watt. Using numerical values from Table IV one computes

$$(P \cdot \ell \cdot d\omega' \, T_\lambda S_\lambda)_o = 26 \text{ amp} \cdot \text{cm} \cdot \text{sterad}$$

Xe laser and radiometer salient parameters for the current chemical laser cavity using existing hardware are as follows.

Table III. Optics Parameters

Scattering Length	ℓ	3.3 mm
Collection Angle	$d\omega'$	0.087 ster
Overall Transmission	T_λ	0.25
Detector Sensitivity	S_λ	48,000 amp/watt

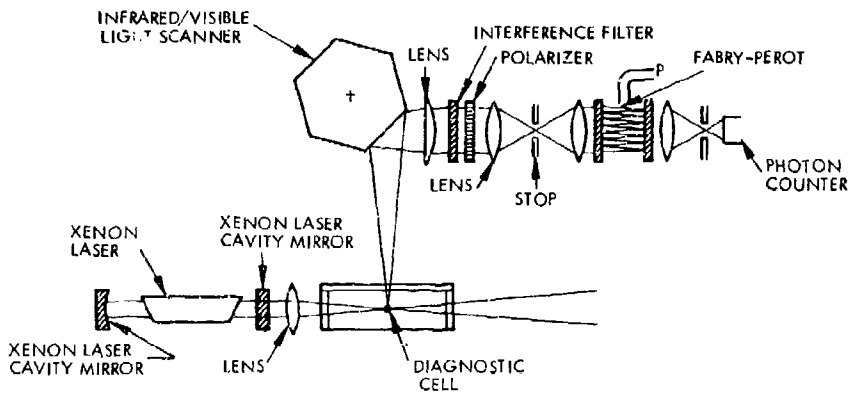

Figure 5. Schematic Showing Xenon-Laser/Infrared/Visible Light Mapper Experiment for Measuring Rayleigh and Raman Scattering Intensities

The radiometer collection solid angle follows from the scanner lens area (10 cm^2) and observation plane distance of 1 meter. The scanner radiometer system is therefore characterized by

$$(P \cdot \ell \cdot d\omega' \, T_\lambda S_\lambda) = 1.2 \text{ amp} \cdot \text{cm} \cdot \text{sterad}$$

The scanner sensitivity factor is given by

$$i/p \approx \frac{1}{20} \cdot \frac{T_o}{T} \cdot (i/p)_o \text{ amp/torr} \tag{10}$$

In equation (10), T_o = 300°K, T is laser cavity local temperature and calibration factors $(i/p)_o$ are from Table 2. For detection of F_2 by Raman scattering, sensitivities near 1.3×10^{-12} amp/torr. Raman signal strength for H_2 is expected to be 1×10^{-14} amp/torr for the same radiometer optics. However, using Rayleigh scattering strengths, one would expect 1×10^{-12} amp/torr for hydrogen. From Table II it is evident that the helium contributes little to bulk scattering. Therefore, the Rayleigh scattering is expected to be insensitive to helium concentrations.

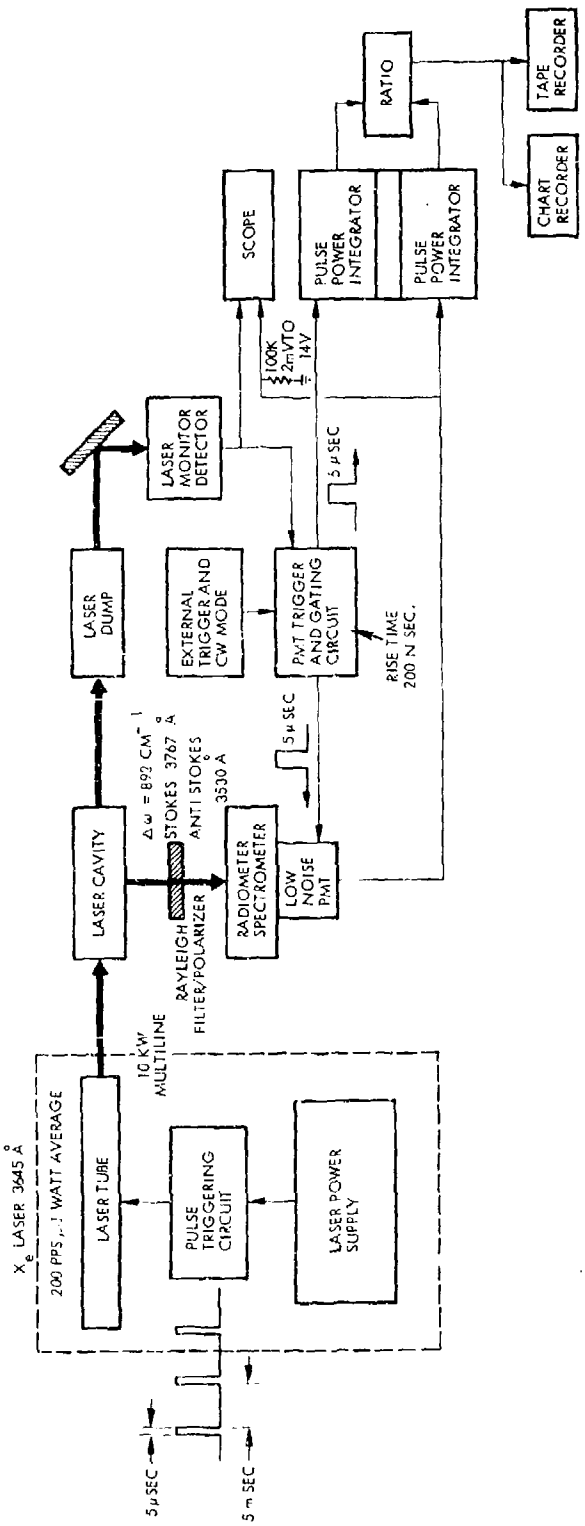

Figure 6. Functional Block Diagram

Table IV. Calibration Factors

Xe laser power	$P = 1$ watt
Radiometer collection angle	$d\omega' = 10^{-3}$ sterad
Spatial resolution	$\ell = 1$ mm
Overall transmission	$T_\lambda = 0.25$
Detector sensitivity	$S_\lambda = 48{,}000$ amp/watt

In order to assess the signal-to-noise problem and permissible sampling rate, consider an available electronic photon detection system using a sensor, gated synchronously with the laser pulses as has been schematically shown in Figure 6. Dark counts for a channeltron photomultiplier (type 7500-5303) are approximately 10 counts/second. Since the Xe-laser is pulsed at a repetition rate of 200 pps with 0.5 μsec individual pulse length, the on-time of the gated tube is 10^{-4} seconds; the effective background count rate is therefore approximately 10^{-3} counts/second. The expected signal/background count rate is therefore very high; however, the absolute signal count rate is fairly low for the existing system. If we define the limit of detectability as that species partial pressure at 300°K reference temperature which generates 3 counts per sampling time Δt, we find the following relation for instrument sensitivity:

$$\Delta t\, P_{limit} = 3\,\frac{eG}{i/P} = \frac{4.8 \times 10^{-13}}{i/P}\ \text{torr} \cdot \text{sec}$$

where $e = 1.6 \times 10^{-19}$ coulomb and G is PM detector gain (10^6). For hydrogen, the limiting sensitivity based on the 3 counts/sampling time criterion is:

$$\text{hydrogen } (P \cdot \Delta t) = 0.48 \text{ torr} \cdot \text{sec (Rayleigh)}$$

$$\text{hydrogen } (P \cdot \Delta t) = 48. \text{ torr} \cdot \text{sec (Raman)}$$

Similarly, for the detection of F_2 by Raman scattering the limit is

$$\text{molecular fluorine } (P\,\Delta t) = 0.37 \text{ torr} \cdot \text{sec (Raman)}$$

It is relatively straightforward to improve the sensitivity of the measurement by up to three orders of magnitude. A factor of 10 sensitivity improvement can be obtained by increasing the power of the existing scanner by an order of magnitude. This can be accomplished by installing a 4.5-inch Cassegrain collector which would conserve the basic mechanical structure of the existing scanner radiometer but require a modest redesign of the scanner head to accommodate the larger more powerful optics. Another factor of 10 improvement can be gained from increasing the available laser power by a factor of 10 by placing the laser cavity internally to the xenon laser cavity. The combined effect of increase in collector and laser power should yield sensitivity increase by a factor of 100, i.e.,

hydrogen $P \cdot \Delta t \approx 5 \times 10^{-3}$ torr-sec (Rayleigh)

hydrogen $P \cdot \Delta t = 0.5$ torr-sec (Raman)

molecular fluorine $P\Delta t \approx 4 \times 10^{-3}$ torr-sec (Raman)

An alternate approach of gaining a factor of 10 in sensitivity is to decrease the radiometer distance to 0.32 meter. This could be accomplished by incorporating an attachment to the existing scanner. A substantial reduction in scanner collector lens distance from the plane of observation is quite practical for Rayleigh/Raman scattering since this experiment does not suffer from parallax effects. Assuming the sensitivities quoted above and employing a reasonable sampling rate of 10 data points/sec (0.1 second sampling time), the expected measuring sensitivity for hydrogen by Rayleigh scattering is 0.05 torr and for molecular fluorine is 0.04 torr by Raman scattering. The sensitivity for detection of hydrogen by Raman scattering is 5 torr for identical sampling times (0.1 sec) and optics parameters. This sensitivity is too low to be of interest for a practical laser cavity diagnostic device.

In conclusion, Rayleigh/Raman scattering is a feasible technique to measure concentrations of molecular hydrogen and molecular fluorine in HF/DF laser cavities with typical sampling rate of 10 data points per second. This can be achieved by using an xenon UV laser ($\lambda = 0.3645\mu$) and by modifying an existing scanner for the task of serving as a laser

Rayleigh/Raman scattering scanning radiometer. Typical detection sensitivity of such an instrument would be approximately 4×10^{-2} torr for the indicated species. Helium in HF laser cavities appears not to be detectable with apparatus of practical design. Additionally, the detection of molecular hydrogen by Raman scattering techniques is marginal at partial pressure levels to be expected in HF/DF laser cavities. Other techniques, such as a high energy electron beam, must be used to detect helium. On the basis of the data available, we recommend a careful evaluation of the xenon laser Rayleigh/Raman scattering technique with a high energy electron beam technique as an alternate approach.

2. HOLOGRAPHIC INTERFEROMETRY DIAGNOSTIC TECHNIQUE

Interferometry is one of the more fundamental and basic methods for the measurement of small optical path length changes (Ref. 3 and 4). Measurement is in terms of the wavelength of light to a precision, in most cases, of a small fraction of a wavelength. Changes which can be measured interferometrically can either be the result of physical motions of a reflecting surface, or the result of refractive index changes. In gaseous media, the refractive index relative to vacuum is directly proportional to the gas density (Ref. 5).

Interferometry is a consequence of the wave nature of light. Specifically it is a result of the fact that light can interfer with itself. A phase difference of 180 degrees between two beams of light of equal intensity results in cancellation or destructive interference. Zero or phase shift of multiples of the wave-length of light results in constructive reinforcement. All interferometers display the difference in optical path between the two interfering beams in terms of a fringe pattern. Dark fringes connote regions of destructive interference. Each fringe traces the loci of a constant optical path change.

Interferometry is routinely used in the testing of optical equipment and surfaces, the making of highly precise distance measurements (the meter is defined in terms of the wavelength of red cadium line), and more recently the testing of mechanical structures.

Prior to the advent of the visible laser, a wide variety of specialized interferometers were available. The more famous classical interferometers include the Mach Zehnder, Twyman Green, Michelson, etc. Multiple beam interferometers, such as the Tolansky, have been used to measure distances of the order of 1/100 wavelength of light (Ref. 6). The Mach Zehnder interferometer is the type most commonly used in the study and measurement of aerodynamic and gas density phenomena. It has only recently been suplanted by laser holographic interferometers.

Since this report is concerned only with measurement of path length variation in a HF/DF chemical laser, the consideration of the Mach Zehnder interferometer is heuristically valuable. It suffices to explain the elements of interferometry. Following this discussion, the applicability of interferometry to the study of the optical region of a chemical laser is considered. Of importance is the estimation of the amount of phase shift produced by operational flows of HF/DF chemical lasers. Such an estimate establishes the applicability of the technique. Finally, the type of interferometer most suitable to measurements in a chemical laser will be considered. A promising candidate is the transmission holographic interferometer illuminated with a pulsed ruby laser. This type of interferometer was developed at TRW and a portable version is in laboratory stock. It has other features which recommend its choice over the Mach Zehnder.

a. Mach Zehnder Interferometer

A Mach Zehnder interferometer is shown schematically in Figure 7. In this interferometer, the input monochromatic beam is divided into two components. One component, the "test beam", passes through the volume of interest, shown as the flow from a nozzle bank. The other component, the "comparison beam," passes around the event. In may many cases the comparison beam is passed through a cell identical with the one in the test beam. This later feature makes true differential measurements possible. A second beam splitter recombines the test and comparison beams, permitting the two to interfere with one another. The resulting interference pattern portrays the retardations of the test beam relative to the comparison beam in terms of an interference pattern.

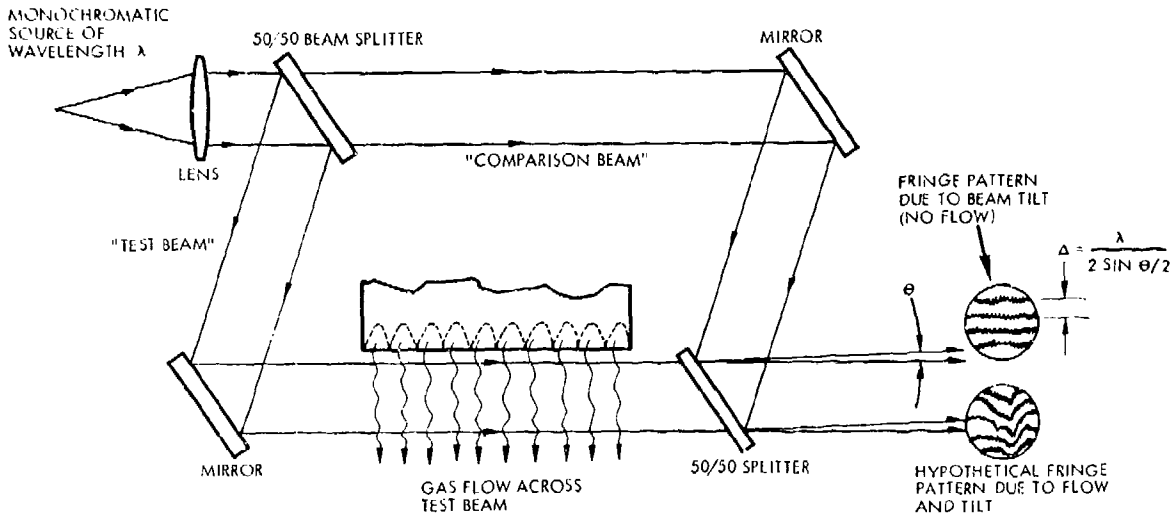

Figure 7. Schematic of Mach Zehnder Interferometer used in Diagnosing Gas Flow

A simple interference pattern is produced whenever the two beams pass through one another at a small grazing angle. Such a pattern is shown in Figure 7. The fringe spacing Δ can be shown to be related to the angle of tilt θ of the two beams according to the equation (11):

$$\Delta = \frac{\lambda}{2 \sin \frac{\theta}{2}} \quad , \tag{11}$$

where λ is the wavelength of the light passed through the interferometer. Such a fringe pattern, in the parlence of interferometry, is called a "finite fringe pattern." In a Mach Zehnder interferometer, parallelism of the fringe pattern caused by beam tilt, is also a testimony of the optical flatness and homogenuity of the elements of the interferometer.

Careful adjustment of the mirrors decreases the number of finite fringes to zero. Such a pattern is called a "zero order fringe pattern." In practice it is very difficult to achieve since the mirrors have to be aligned to at least a tenth of a wavelength. Typically Mach Zehnder interferometers are used with a finite fringe pattern. Variations in the density of the gas in the test beam path produce fringes in the output beam pattern. Neighboring fringes denote a change in phase of a full wavelength. The phase change suffered by each wave is the change in path divided by the wavelength of light. This ratio expresses the relative phase change in terms of wavelengths. A hypothetical pattern has been traced in Figure 7.

b. Phase Shift and Interferometer Sensitivity

In any transmission interferometer (like the one shown in Figure 7) path change is only varied by changes in gas density. Optical path, however, is the product of the index of refraction and the physical path. Since the gas density can vary locally, the product must be integrated to get the net path variation along individual portions of the test beam. In the most general case the phase change in terms of the wavelength of light passed through the interferometer is:

$$S = \frac{1}{\lambda} \int (n_2 - n_1)\, dz \tag{12}$$

where n_2 refers to the index of refraction along the test beam, and n_1 is the index of refraction along the identical comparison beam. Values for the refractive index of different gases are available in the handbooks (Ref. 7). Values of interest to the HF chemical laser have been reproduced in Table V. Also included in the table are values of the Gladstone-Dale constant and the interferometric sensitivity of the gas at the wavelength value of a ruby laser (0.6943 micron). In all calculations, it is assumed that the index of refraction of a gas, relative to that of vacuum (i.e., $n_{vac} = 1$), is directly proportional to the gas density N, namely,

$$n - 1 = K N$$

The constant of proportionality K is called the Gladstone-Dale constant. It can be interpreted as the refractive index of a molecule per cubic centimeter of volume. Its units are cubic centimeters. This constant is computed by dividing the difference between the index of refraction of the gas and that of vacuum by the Loschmidt number (the number of molecules per unit volume of an ideal gas at $0^{\circ}C$ and at normal atmospheric pressure $N_o = 2.68719 \times 10^{19}$ molecules/cm^3).

Table V. Interferometer Constants of Gases of Interest to HF Chemical Lasers

Gas	n_o Refractive Index at 0°C, 760 mm Hg, 0.589μ*	K Gladstone Dale Constant cm^3	S/ℓ Po Interferometer Sensitivity in Waves per Cm, per Atmosphere at 0° at 0.6943μ
Dry Air	1.0002926**	1.0889×10^{-23} cm^3	3.8
N_2	1.000297	1.105×10^{-23} cm^3	-
O_2	1.000516	1.920×10^{-23} cm^3	-
H_2 and D_2	1.000132	0.491×10^{-23} cm^3	-
F_2	1.000108	0.402×10^{-23} cm^3	-
F	1.000054	0.201×10^{-23} cm^3	-
He	1.000036	0.134×10^{-23} cm3	-
HF	1.0001	-	-

*Wavelength sodium D lines are 0.588953 and 0.5895923μ, respectively.
**Variation in index with wavelength for air is small; n_{blue} = 1.0002825 while n_{red} = 1.0002754.

For mixtures of gases the resultant index is the sum of the individual constituents:.

$$n - 1 = \sum K_i N_i \tag{14}$$

Multiplication of equation (14) by the total density of molecules enables one to express the change in index in terms of the mole fractions (χ_i) of the individual constituents; that is,

$$n - 1 = N \sum K_i \left(\frac{N_i}{N}\right) = N \sum K_i \chi_i \tag{15}$$

Substitution of equation (15) into equation (12) shows in principle how an interferogram yields gas density. The above equations and the values listed in Table V enable a calculation of the path variation expected when an operating HF/DF chemical laser is put into the test beam. In this case the following expression can be derived from equation (12):

$$S = \left(\frac{K_o N_o}{\lambda}\right)\left(\frac{N}{N_o}\right)\frac{(\Sigma K_i \chi_i)_1}{K_o}\left[\frac{(\Sigma K_i \chi_i)_2}{(\Sigma K_i \chi_i)_1} - 1\right] L \qquad (16)$$

where

subscripts 1 and 2 refer to the comparison and test scenes, respectively, and a "uniform" slab of gas is considered

$P_1 = P_2$ (comparison and test cavity pressures are equal)*

$T_1 = T_2$ (comparison and test cavity temperatures are equal)*

χ_i = the mole fraction of the ith specie

N = the number density of the gas in the cavity

N_o = Loschmidt's number (2.7×10^{19} particles/cc) i.e., number density at standard conditions

K = particle refractivity, cm^3 (recall that $n - 1 = KN$)

K_o = particle refractivity for nitrogen

L = the length of the optical path

λ = radiation wavelength.

In each case the wavelength will be that of a ruby laser. The subscript 1 refers to a chamber identical to the test chamber but placed in the comparison beam path and containing nonflowing gas or a vacuum. The subscript 2 refers to the test chamber. Later it will be seen that for a holographic interferometer the test and comparison waves are simply separate

*This assumption is not crucial to the final results as will be shown later.

exposures of the hologram. Several example cases have been calculated using the flow compositions typical of early chemical laser devices (e.g., CL-I). Two operating conditions are considered; operation with pure nitrogen as the diluent (Case I), and operation with helium as diluent (Case II). In addition the effects of helium and nitrogen in the comparison chamber were also calculated. For these calculations, the active volume or cavity length was taken to be 1 meter in physical length and the operating pressure was 10^{-2} atmospheres (7.6 torr). The results are tabulated in Table VI.

Table VI. Average Fringe Shift Expected in an HF Chemical Laser at 0.6943μ

Case	χ_{H_2}	χ_{HF}	χ_{He}	χ_{N_2}	$(\chi_{N_2})_c$*	$(\chi_{He})_c$	L (cm)	P_L (atm)	S Fringe No.	$(\frac{\Delta N}{N})_{min}$
1	0.62	0.05	0	0.33	1.0	0	100	10^{-2}	-1.9	0.04
	0.62	0.05	0	0.33	0	0	100	10^{-2}	+2.6	
2	0.62	0.05	0.33	0	0	1.0	100	10^{-2}	+0.9	0.07
	0.62	0.05	0.33	0	0	0	100	10^{-2}	+1.47	

*( )c Refers to comparison chamber.

The next to last column lists the predicted maximum amount of fringe shift. Inspection shows that the greatest number is produced when comparison is made against a vacuum or when $(\chi_{N_2})_c$ and $(\chi_{He})_c$ are zero. For a 100-centimeter physical path length, the number of fringes is sufficient to test for optical uniformity as well as visualize aspects of the flow. This is more credible when one recalls that conventional interferometric devices are sensitive to path changes of 1/10 of a wavelength of light.

Differentiation of equation (16) enables calculation of the minimum sensitivity of the interferometer under the same cases listed in Table VI;

$$\frac{\Delta N}{N} = \frac{\Delta S}{\left(\frac{K_o N_o}{\lambda}\right) \frac{\left[\Sigma K_i \chi_i\right]_2}{K_o} \left(\frac{N}{N_o}\right) L} \tag{17}$$

Note that the expression does not depend on comparison beam conditions. Values of the minimum density variation are listed in the last column of Table VI. They show that for a 100-centimeter-long HF/DF laser cavity, the minimum density variations are 4 and 7 percent, respectively, for the two conditions considered, assuming a minimum decernable fringe shift of $1/10\lambda$.

For a laser cavity of 20 centimeters length (e.g., CL III) the gross changes are effectively one-fifth those of the 100-centimeter cavity. Minimum density sensitivity is five times less. An interferometric measurement then appears more marginal; however, sensitivity could be increased by using light of shorter wavelength. One very attractive approach is to use a modified ruby laser as the interferometer illuminator. Not only is the ruby laser of short duration (0.05 microsecond typically) but the output wavelength can be converted into ultraviolet light by the process of frequency doubling. The short duration essentually freezes any aerodynamic phenomena. Radiation of half the wavelength doubles the sensitivity of any interferometer. Experiments have already been conducted using simultaneously both the primary red radiation (0.6943 micron) and the doubled ultraviolet (0.3472 micron) radiation from a ruby laser to illuminate a simple holographic interferometer (Ref. 8). The experiments verifies the ability to make such interferometric measurements. The doubled frequency light from a ruby laser is in a region of the spectra where many optical materials become absorptive. Quartz windows and lenses are necessary.

Multiple beam interferometers offer an additional method of increasing the sensitivity of the interferometric examination process. The Tolansky interferometer has already been mentioned (Ref. 6). Work has also been done, under sponsorship of NASA, on increasing the sensitivity of the holographic process (Ref. 9).

Shocks and turbulences will further increase the fringe shifts over the values given in Table VI.

c. Interferometer Selection for HF/DF Laser Cavities

The previous section showed that information about the optical homogeneity and gas density variations in a large HF chemical laser could result from a visible interferometric examination. The choice then is one of finding the best interferometer for the application. Presently the choice is

dictated by availability. TRW has developed and gained considerable experience in the area of holographic interferometry. One such interferometer is readily available. It was originally developed for the recording of transmission holograms of liquid rocket engine combustion (Ref. 10). It has also been used for the recording of double exposure holographic interferograms of aerodynamic phenomena, and more recently, to record path length variations in atmospheric electrically excited CO_2 gas lasers (Ref. 11).

A photograph of this interferometer is shown in Figure 8 and Figure 9 shows a schematic of the optical train. Figure 8 shows the holocamera with the illuminating ruby laser mounted on the main support column. More recently the Q switched laser has been mounted separately. The holocamera is portable and has a relatively large scene volume. As shown in the above illustrations, the scene volume will accept a laser cavity 22 inches (55 centimeters) long. The scene volume can be easily increased. Removal of one of the focusing lenses permits lengthing the holocamera, and increases the scene volume length to 48 inches (120 centimeters).

The optics in the existing system are unfortunately absortive at 0.34 micron. As a result the holocamera can only be used at the functional wavelength of the ruby laser (0.6943μ).

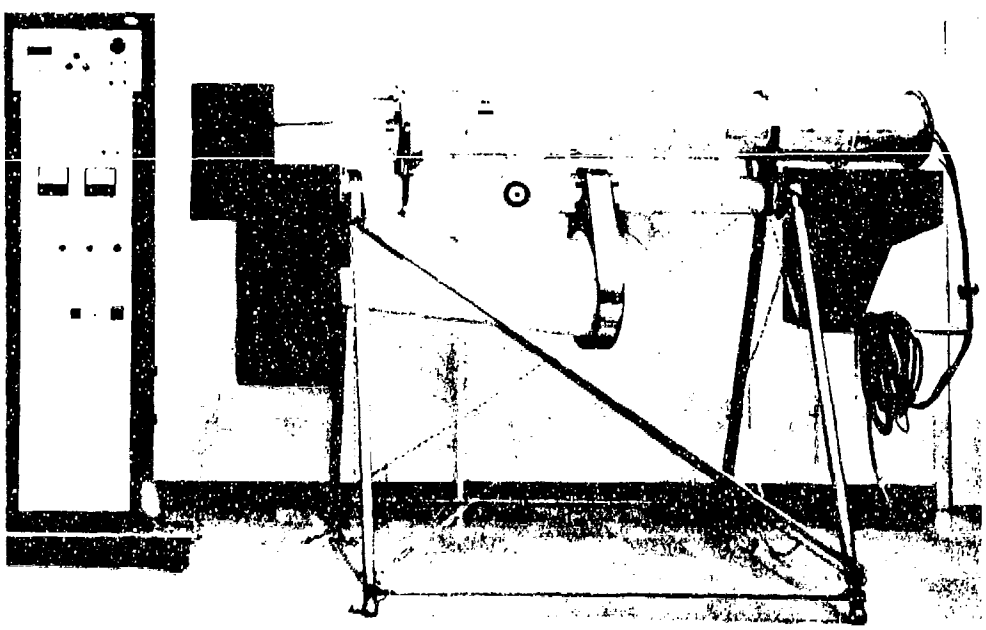

Figure 8. TRW Holocamera Apparatus Developed Under NASA Contract (Courtesy NASA)

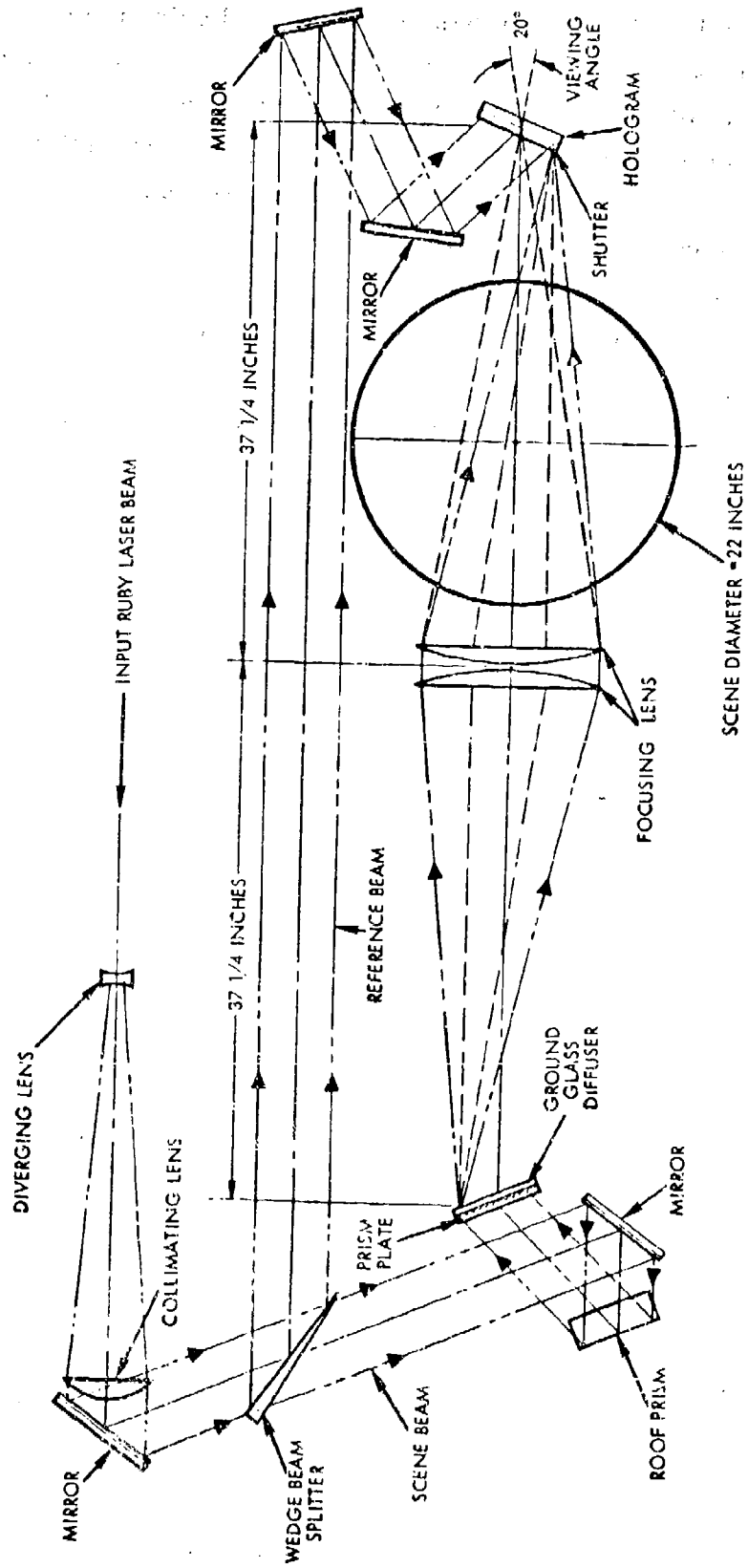

Figure 9. Schematic Diagram of the Optical Train of the Transmission Holocamera Shown in Figure 8

Holographic interferograms are recorded by the double exposure process. The first exposure records the "comparison scene". The second exposure records the test scene with its accompanying nonuniformities. The reconstruction of the hologram recreates the two wavefronts simultaneously with the result that the interference phenomenon is seen. The result is no different from that which would be obtained from a zero order fringe Mach Zehnder interferometer. Holographic interferometers of the type shown in Figure 9 are truely differential interferometers, as a result they are not (unlike the Mach Zehnder) dependent upon precision optics or windows. Further, they permit the incorporation of a ground glass diffuser in the scene path. This ground glass makes possible a continuous variety of viewing angles, permitting sampling of the optical path length changes over the continuum of angles permitted by the focusing lense set and hologram size. In contrast, a Mach Zehnder interferometer gives only one view through the gasesous pheneomena.

In conclusion, holographic interferometry appears to be a viable cavity diagnostic technique when employed on larger chemical laser devices where the optical path length is on the order of 1 meter. However, the method has marginal utility, i.e., it produces extremely small fractions of a fringe, when used in conjunction with current, smaller chemical laser systems unless modifications are made to existing interferometry devices and techniques to extend the state of the art. This is caused principally by the relatively short optical path length and very low density gases in the lasing region of the smaller laser devices.

SECTION III

LASER SYSTEM DESIGN

The second task in the subject program involved the design and fabrication of an advanced chemical laser system, designated CL III.

Important considerations in a total chemical laser system design included power and weight of the cavity pumping equipment. It is advantageous to operate at high cavity pressure and high injector nozzle throat Reynolds numbers (approximately 2700 as compared to 300 characteristic of the earlier CL II device) so that the boundary layers are thin, thus preserving total pressure recovery potential. Both of the above requirements lead to designs in which the reactant mixing process is likely to be the rate-limiting step in the laser pumping chemical reaction. The ratio of this pumping rate to the deactivation rate is a parameter which has a major influence on laser efficiency and power output. It is, therefore, essential that the mixing be rapid, implying that the process should be turbulent.

Furthermore, since reactant mixing with the least possible loss in total pressure while maintaining high axial velocity is desired, a configuration consisting of alternate parallel streams of fuel and oxidizer is suggested. The arrangement is shown schematically in Figure 10. The mixing angle, α, is a mesaure of the rapidity of mixing and depends, at subsonic speeds at least, on the velocity difference between the two streams (see Section III. 3. b (2). The greater the velocity difference,

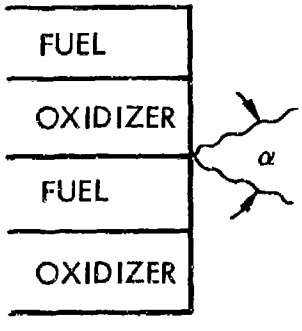

Figure 10. Alternate Parallel Stream Mixing Concept

the greater the spreading angle. Unfortunately, the total pressure loss also increases with this difference.

Because of the necessity for a compromise in the two effects just discussed and also because of the lack of experimental information on mixing at supersonic speeds, it was decided to design an advanced cavity injector that could achieve a large range of conditions that influence mixing.

In the following sections, the CL III cavity injector concept is first described followed by a discussion of the related laser system hardware. The design analyses performed in arriving at the CL III laser configuration are then presented.

1. CL III CAVITY INJECTOR DESCRIPTION

The CL III cavity injector represents a first attempt to deal with the problems of parallel stream mixing and scaling the HF/DF chemical laser to a high power device while retaining good pressure recovery potential. The design reflects application of the conclusions regarding advanced laser design contained in reference 1 and summarized as follows:

(1) Preclude ground state entrainment from the lasing zone

(2) Enhance turbulent jet mixing by gas injection velocity control

To date, small scale chemical laser cavity injectors have depended upon large viscous boundary layers in a hot atomic fluorine stream and a free-jet H_2 stream to provide large velocity gradients to induce the turbulent mixing processes. These small scale, low Reynolds number devices do not lend themselves readily to scaling to higher powers, particularly where pressure recovery from the supersonic flow stream is required. A flexible cavity injector design was required which could provide a range of flow conditions for the study of turbulent mixing processes at high Reynolds number and the interaction of such a high Reynolds number flow with the laser optics and pressure recovery devices. Based upon the premise that the chemical laser mixing processes are turbulent as opposed to laminar diffusion, an injector design which could provide large relative velocity differences between H_2 and F streams was conceived.

The design concept presented herein is based upon observation, analysis, and testing of the TRW CL II chemical laser system under ARPA/AFWL Chemical Laser Technology Contract. Other sources of design data included a literature search of empirical and analytical data of parallel stream mixing criteria, cold flow nozzle tests, boundary layer analysis programs and pressure recovery considerations.

a. Design Objectives

The ideal chemical laser system would supply a uniform supersonic flow of fluorine atoms, helium or N_2 diluent, and hydrogen, instantaneously mixed at a stoichiometric mixture ratio and at a static temperature which optimizes production/deactivation rate ratios. The population inversion of the HF^* molecules would be formed at the entrance to the optical cavity in a uniform flow field free of shocks and pressure gradients. Supersonic velocities would be sufficiently high to lengthen the region of population inversion such that a high power beam could be extracted without undue loading on the cavity mirrors.

Obviously, the ideal cavity injector cannot be attained within the current state of the art. The CL III laser was designed to study methods of increasing turbulent mixing processes, effects of nozzle exit temperature, and net mixed velocity on lasing efficiency. The following basic design criteria were established:

- The device should be flexible, allowing for different operating modes which provide widely varying velocities of the H_2 and F jets as well as a range of nozzle exit temperatures and dilution ratios.
- The device should be capable of supplying preheated H_2 at high mach number and velocity. DF combustion will be used to preheat the H_2 stream.
- Combustion pressures should be in excess of 100 psia to provide a flow field consistent with pressure recovery requirements. Nozzle viscous boundary layers should be reduced to values constituting a small percentage of the flow.
- The nozzles should be designed to account for boundary layer buildup, area ratios increasing as dictated by an analysis of boundary layer thickness.

- The nozzle area ratio should be designed to closely match the exit pressure to the expected cavity pressure.
- The lasing zone should be confined within a suitable lasing cavity to preclude entrainment of ground state HF into the supersonic flow stream.

b. Parametric Design Study

A parametric analysis was performed to provide data on the required combustor DF flows, diluent division between H_2 and F combustors, operating temperatures, throat area, nozzle parameters and cavity injection velocity. Approximately 100 thermochemistry and isentropic nozzle flow computations were performed. These computations were then corrected for boundary layer and heat loss considerations. The resulting parametric operating curves are presented later in this section.

From these analyses, the CL III design was selected which provides the capability of operation over a wide range of varying conditions. Table VII presents several of the possible sets of operating conditions including the predicted nozzle exit velocity and velocity ratios for a combustor chamber pressure of 75 psia.

c. Design Description

The CL III cavity injector concept is shown in the three-dimensional cutaway of Figure 11 and the hardware assemblies are shown in Figures 12 through 14. The device includes two combustors, two cold gas injectors for D_2, F_2 and diluent, and a single nozzle bank. The top combustor shown in Figure 11 atomic fluorine is the source. D_2, F_2 and diluent are mixed to produce the desired initial temperature and quantity of fluorine atoms. The combustor supplies 11 separate plenums and fluorine injection nozzles. The combustor centerline is perpendicular to the nozzle flow axis. This right angle canted nozzle configuration is common in rocket engine applications where space and geometry constraints dictate.

The bottom combustor supplies D_2 and F_2 under stoichiometric conditions and diluent as a preheating gas source for H_2. The H_2 injection occurs at the entrance to the throat convergence section through five 0.010 inch orifices per H_2 plenum in each of 12 separate plenums.

Table VII. Potential CL III Operating Conditions

Potential Test Condition	Injector	Combustor Conditions							Nozzle			
		$\dot{m}_{D_2}$ (gm/sec)	$\dot{m}_{F_2}$ (gm/sec)	$\dot{m}_{He}$ (gm/sec)	$\dot{m}_{N_2}$ (gm/sec)	$\dot{m}_{H_2}$ (gm/sec)	P_c (psia)	Temperature (°K)	Vex (ft/sec)	Pex (psia)	Tex (°K)	Velocity Ratio $\frac{V_{ex}(F)}{V_{ex}(H_2)}$
1	H_2	1.41	26.6	17.6	0	4.0	75	1000	9,720	0.988	98	0.66
	F	1.60	34.2	0	0	0	66	1700	6,440	0.963	204	
2	H_2	1.66	15.8	17.2	0	3.0	75	1300	10,260	0.0973	126	0.63
	F	1.60	34.2	0	0	0	66	1700	6,440	0.963	204	
3	H_2	1.60	15.2	10.4	0	1.2	75	1870	11,010	0.0973	181	0.58
	F	1.60	34.2	0	0	0	66	1700	6,440	0.0963	204	
4	H_2	1.60	15.2	10.4	0	1.2	75	1870	11,010	0.0973	181	0.57
	F	1.20	22.8	0	17.6	0	67	1800	6,300	0.1069	248	
5	H_2	1.41	13.3	17.6	0	4.0	75	1000	9,460	0.897	84	0.95
	F	1.82	26.8	6.8	0	0	75	2000	8,980	0.0943	189	
6	H_2	0	0	0	98.1	3.6	75	300	2,870	0.1240	48	2.58
	F	1.92	37.2	4.2	0	0	75	1700	7,420	0.0971	172	
7	H_2	0.85	7.98	0	46.2	2.0	71	1000	5,210	0.156	185	1.59
	F	1.57	16.0	6.0	0	0	73	1700	8,270	0.123	203	
8	H_2	1.52	14.4	17.2	0	3.0	78	1000	9,630	0.116	115	0.59
	F	1.40	15.2	0	22.4	0	75	1700	5,700	0.197	339	
9	H_2	0	0	0	98.1	3.6	75	300	3,110	0.155	70	2.61
	F	1.66	34.8	6.0	0	0	75	1700	8,130	0.124	222	
10	H_2	1.52	14.4	17.2	0	3.0	75	1000	9,630	0.116	115	0.86
	F	1.66	34.8	6.0	0	0	75	1700	8,270	0.123	203	

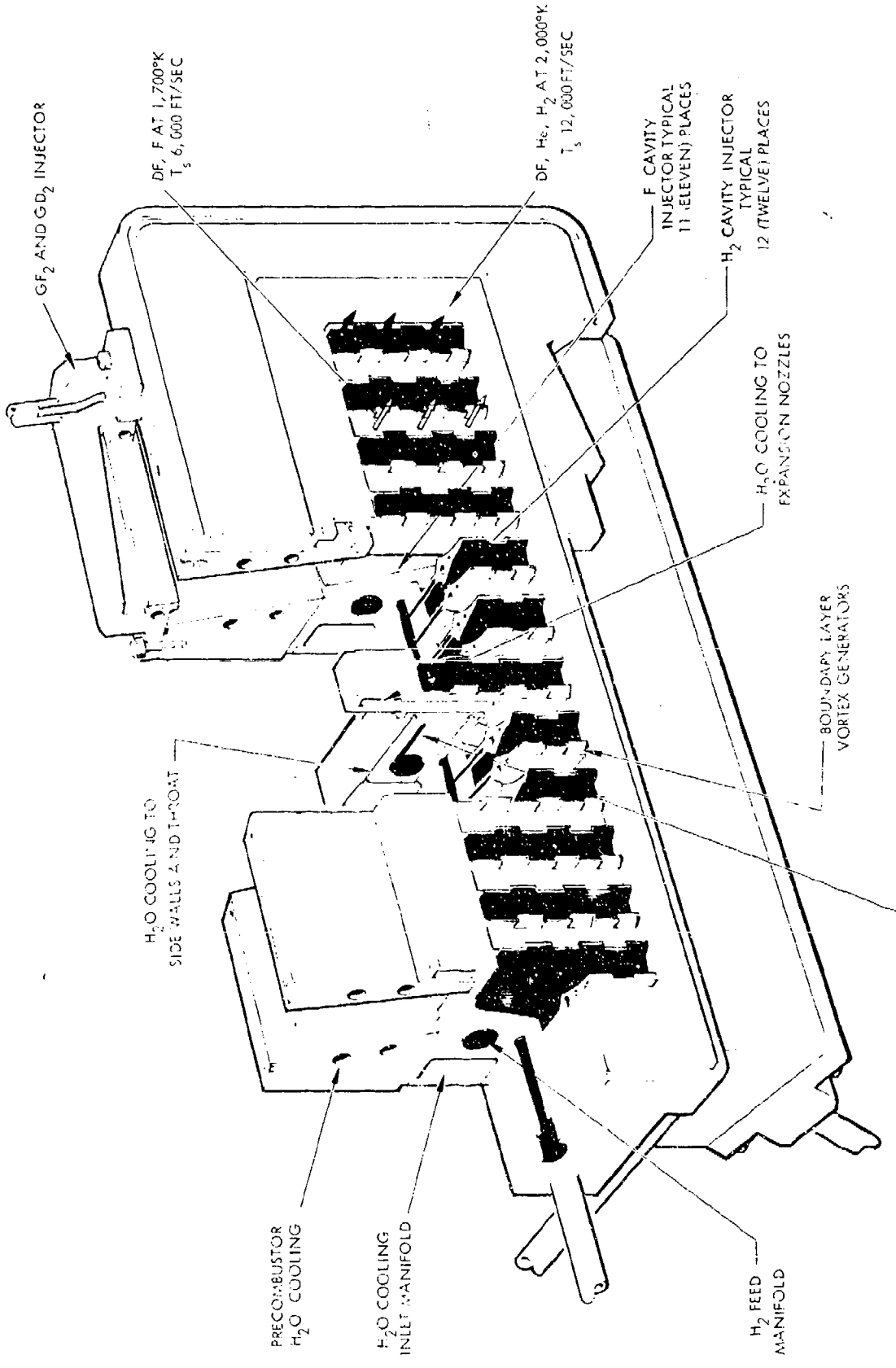

Figure 11. TRW C.L. III Combustion Driven Chemical Laser Cavity Injector

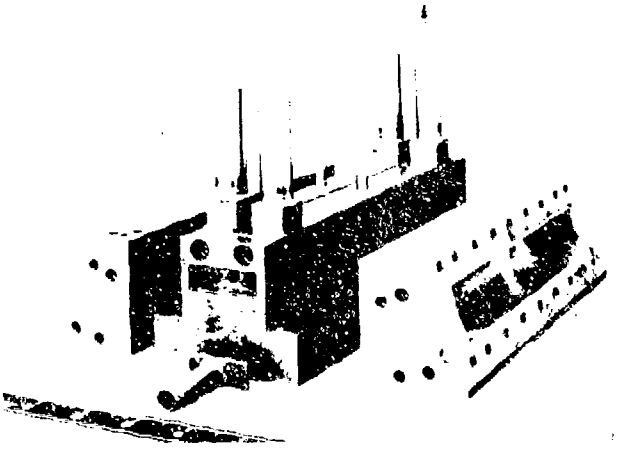

Figure 12
Partially Assembled
CL III Injector

Figure 13. CL III Injector Assembly

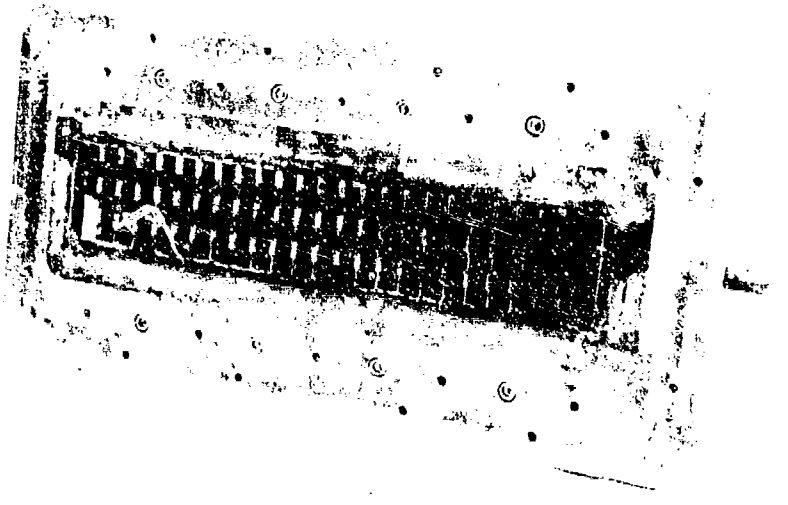

Figure 14. CL III Cavity Injector Showing Nozzle Exit and Vortex Generators

Typical chamber stay times for the H_2 are calculated to be 5 to 8 microseconds. Worst case calculations for HF/DF isotope exchange rates indicate such stay times to be conservative by approximately one order magnitude at 2000°K.

Plenum temperatures up to 2500°K are attainable for both H_2 and F injection with operating pressures up to 150 psia.

In view of the lack of experimental information on mixing at supersonic speeds, it was decided to augment the flexibility built into the basic injector design by the addition of vortex generators to the base between the two nozzles. The vortex generator configuration shown in Figure 11 generally follows that described in reference 12. There, it is shown that the generators approximately double the turbulent spreading angle, but since the experiments were done at subsonic speeds, there is uncertainty of their efficacy under the present conditions. It is recognized that vortex generation will produce some shock and expansion waves in the lasing region that may have deleterious effects on beam quality. This point needs to be investigated experimentally in more detail.

Cooling of the vortex generators, which are an integral part of the copper nozzles, is provided by a cooling passage in the copper nozzle wall supplied from a manifold at the top and bottom of the nozzle bank.

Should the generators prove ineffective or should they not be needed, the design is such that they can easily be removed.

Plenum wall and nozzle throat cooling water are supplied from manifolds located at the back side of the cavity injector main body. Cooling water is fed through the plenum walls to the nozzle throat and back out through the plenum walls to an outlet manifold.

The design requires only two mechanical seals at the injector to combustor interfaces. The combustors are high temperature brazed to the cavity injector body. The cavity injector is fabricated from a single block of copper. The nozzles and plenums are formed by EDM techniques.

The cavity injector exit is 1.5 inches in height by 8 inches long. An O-ring seal is provided for attachment to a 12 x 12 x 32 inch optical cavity box with removable top, bottom and side plates. This cavity box

provides for laser diagnostics, traversing pressure probes, stable resonator and unstable confocal oscillator attachment, and installation of pressure recovery diffuser configurations.

Control of oxidizer and fuel combustors is totally independent as well as the percentage split of diluent between combustor fuel and oxidizers. Nitrogen or helium diluent can be used in either combustor.

The percentage of total heat lost to the combustor and plenum walls was computed to be comparable to the CL II device. Ultimately, percentage heat losses can be reduced in the larger devices. In this case, however, reduction of heat loss has been sacrificed for flexibility of operation (total separation of oxidizer and fuel combustors and plenums).

The isentropic parametric design study presented in Section IV suggests a nozzle area ratio of 24/1 for both H_2 and F nozzles. When corrected for boundary layer considerations, the geometric area ratio becomes 30/1. The cavity injector was designed with two-dimensional nozzles 1.5 inches high with 0.0095-inch throat width and 0.285-inch exit width.

2. LASER SYSTEM DESCRIPTION

a. Propellant Feed System

Gaseous reactants are supplied to the CL III combustors as shown in the propellant circuit schematic of Figure 15. Plumbing of the CL III combustors and cavity injector is shown in Figure 16. The diluent circuits are plumbed to allow helium or nitrogen to be used in either combustor (i.e., helium may be used in the F_2 combustor and nitrogen in the H_2 heater combustor).

All reactants and diluents, except for fluorine, are supplied by pressurized K-bottles. The fluorine is stored as a liquid and during testing, the storage tank is pressurized with helium to expell the liquid. The liquid fluorine is then vaporized in a heat exchanger. A bank of K-bottles in the circuit is employed as an accumulator to damp out surges in the fluorine circuit caused by variations in the liquid-gas interface level in the heat exchanger.

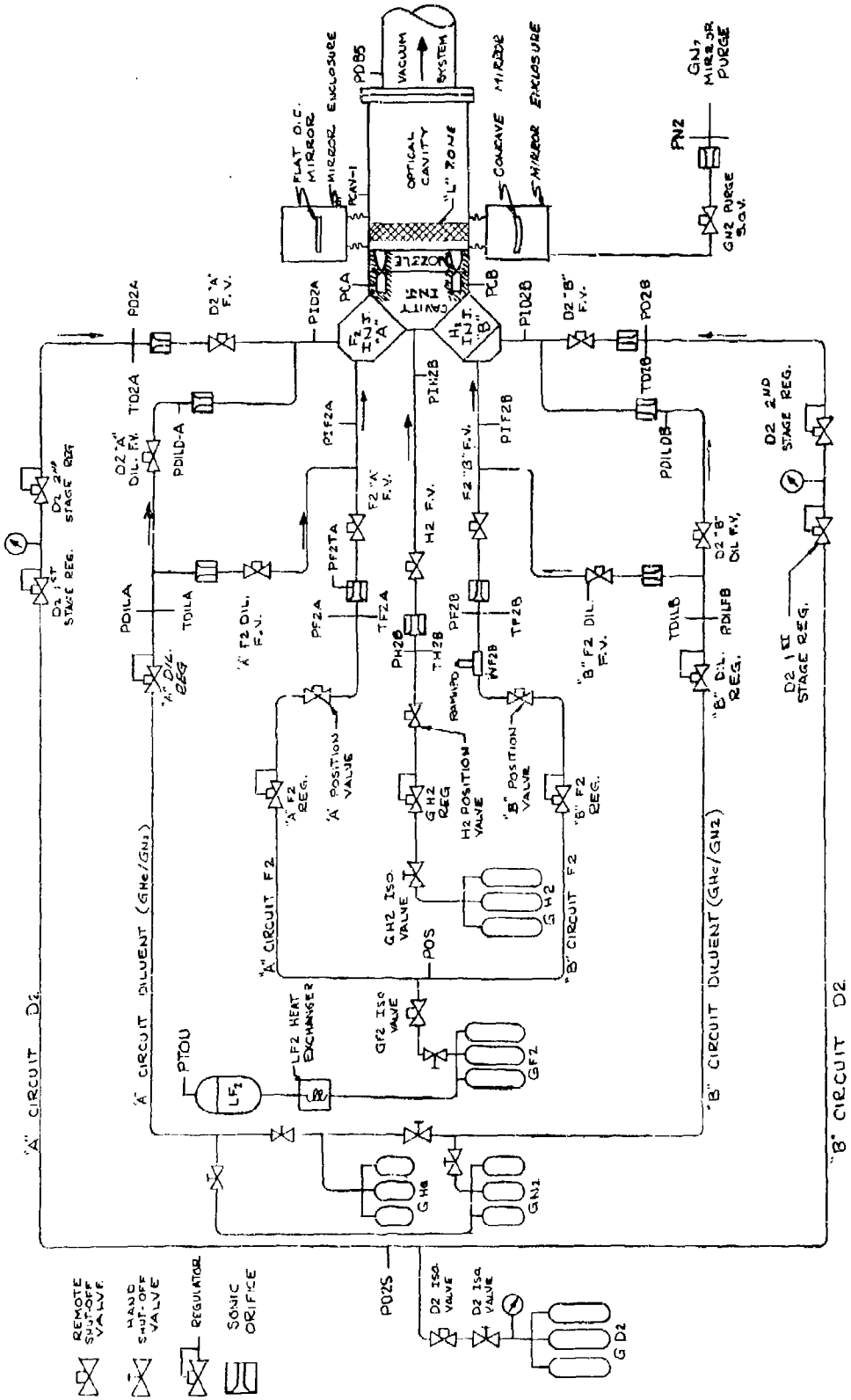

Figure 15. CL III Propellant Schematic

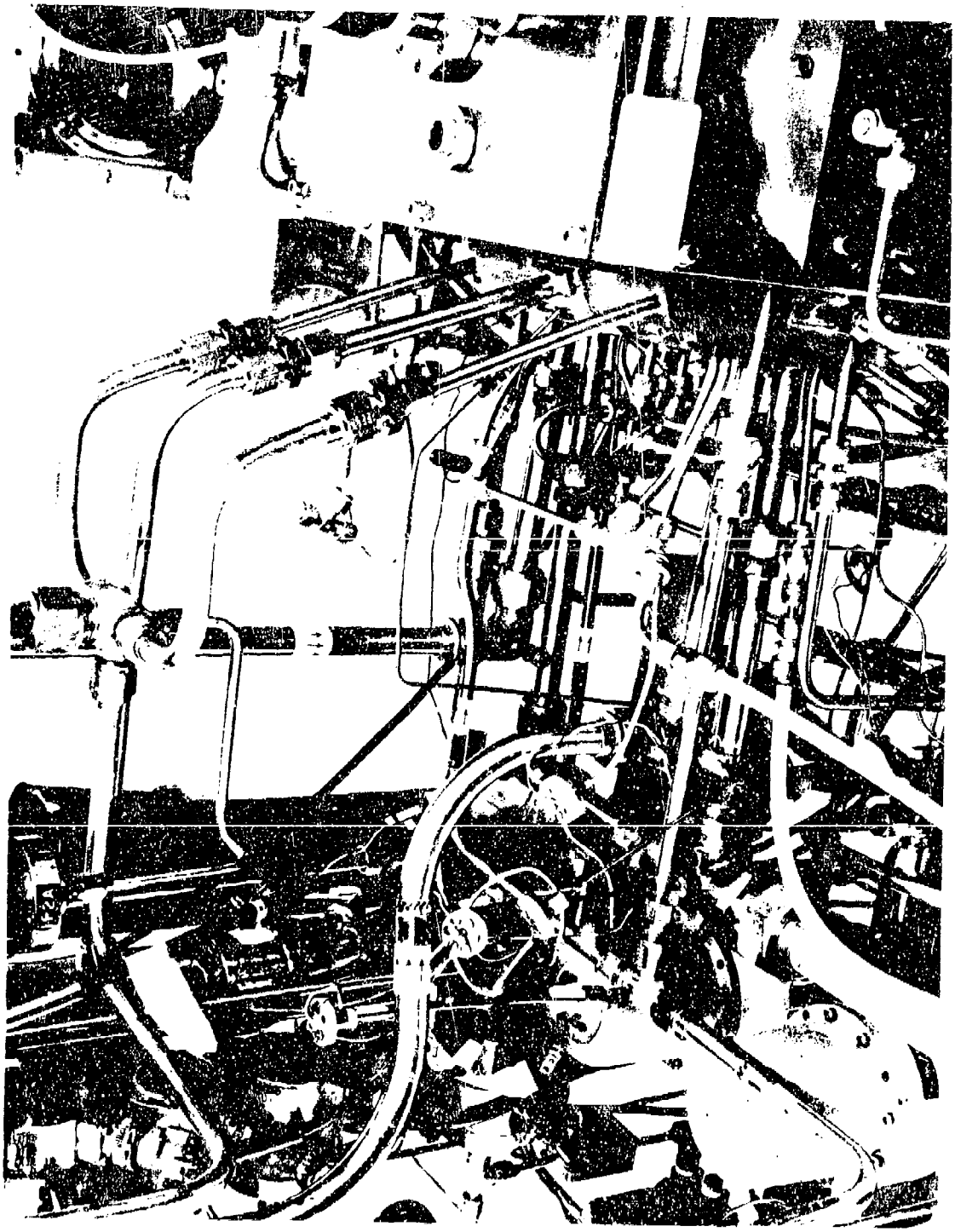

Figure 16. Photograph Showing Plumbing of CL III Combustors and Cavity Injector

Flow control and flow rate measurement are achieved by calibrated sonic control orifices in each propellant and diluent circuit. Flow rate calculations are performed employing the methods of reference 13.

b. Coolant Water Feed System

Deionized water is used for laser hardware, mirror and calorimeter cooling as shown in Figure 17. Two separate coolant circuits are employed; a high pressure system for hardware cooling and a low pressure system for calorimeter water and mirror cooling. Flow control and flow rate measurement to the hardware are achieved by calibrated cavitating venturies in each circuit fed from a common manifold.

c. Optical Cavity

Figures 18 and 19 show the installation of the CL III laser within the 12 x 12 x 32-inch cavity box. Adjustable laser cavity sidewalls for prevention of entrainment by the jet and recirculation of ground state HF from downstream are shown in place. The divergence angle of the sidewalls (or shrouds) may be altered by a mechanism external to the cavity box. The angle is set to obtain as nearly as possible a constant pressure expansion. Four pressure transducers are installed along the cavity sidewall to obtain a pressure profile through the lasing zone and slightly downstream.

d. Optics

The CL III optical system was a hole outcoupled stable cavity. The GFE spherical back mirror was 6 inches in diameter with a 3-meter spherical radius. The mount for this mirror was remotely adjustable in two planes by means of a 28 vdc driving motor and screw linkage as shown in Figure 20. A position potentiometer was attached to the horizontal adjustment motor shaft and calibrated prior to test to obtan X_c values versus potentiometer output voltage.

The second GFE mirror was a 20 percent hole outcoupled flat mirror, shown in Figure 21. This mirror was also remotely adjustable in two planes, for final adjustment of the optical axis under vacuum conditions. Deionized water was supplied to both the spherical and 20 percent outcoupled flat mirror for cooling.

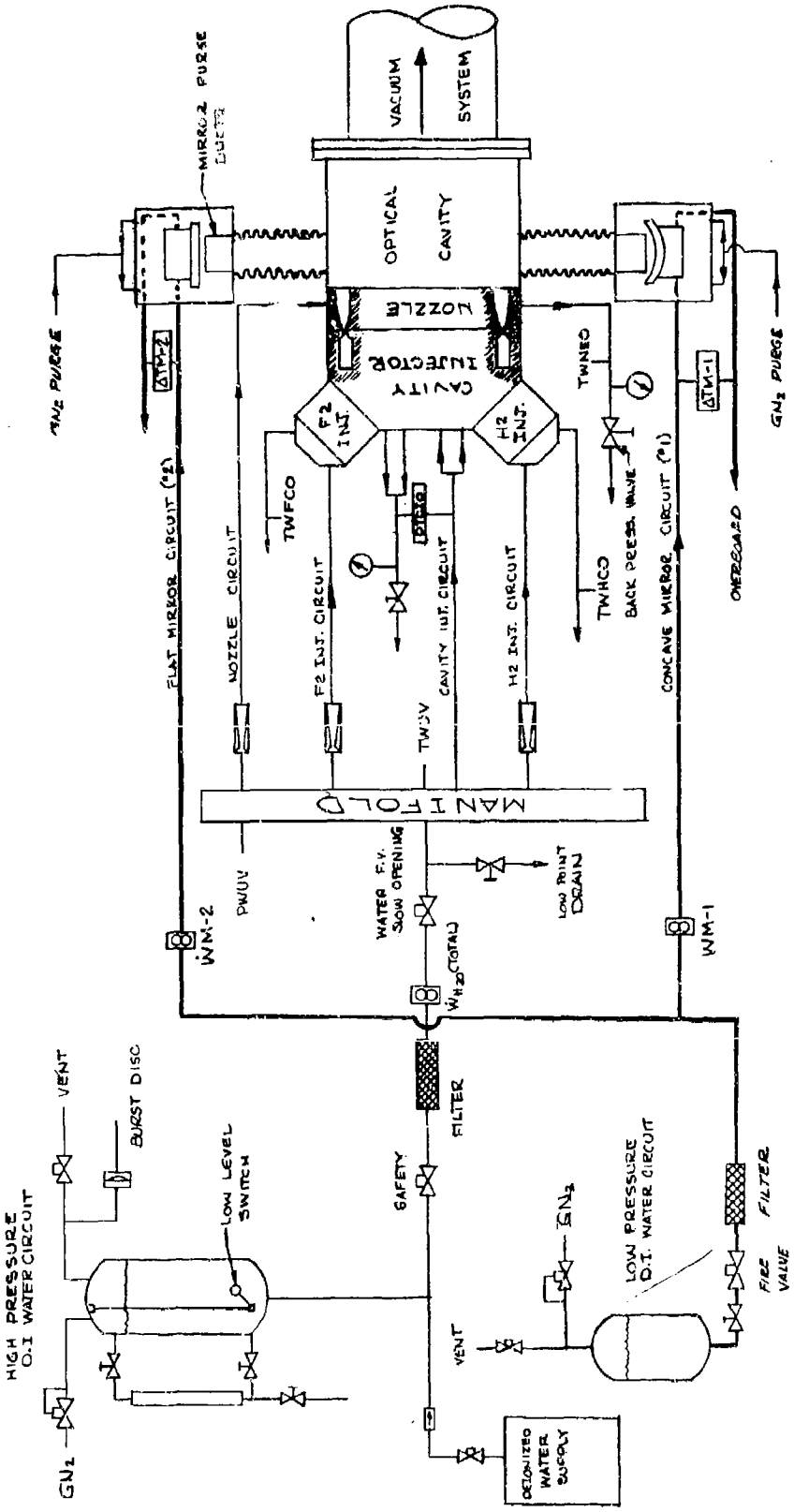

Figure 17. CL III Laser Coolant Water Schematic

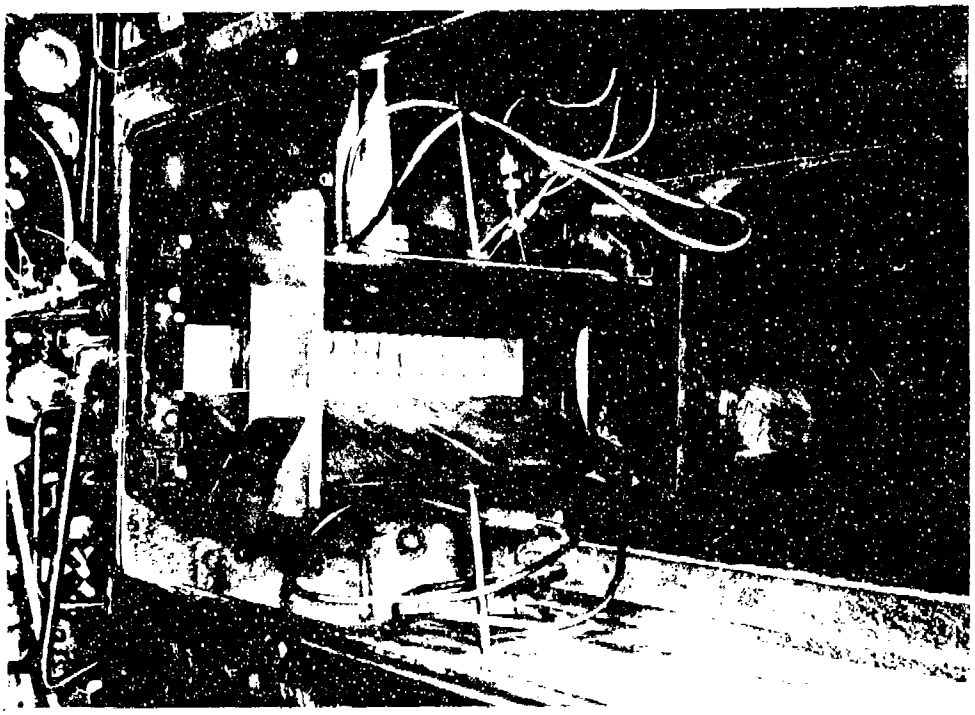

Figure 18. Installation of CL III Laser in Cavity Box

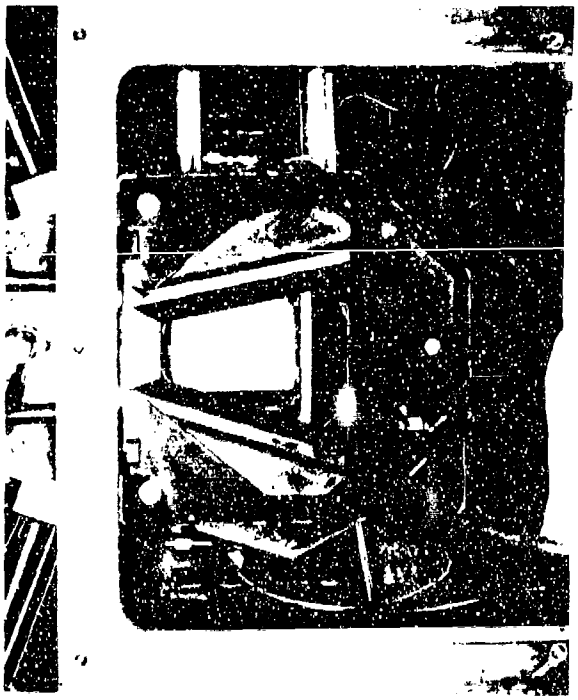

Figure 19. Closeup of CL III Laser in Cavity Box

Figure 20. Mirror Mount

Figure 21. 20% Hole Outcoupled Flat Mirror

The mirror enclosures were attached to the cavity box through metal isolation bellows and were supported by a rigid optical bench as shown in Figure 22. Dry nitrogen was used to purge the mirror enclosures and the lasing zone through the bellows. Mirror purges were set at flow rates of 2.0 to 4.0 grams per second through each enclosure.

e. Calorimeter

The TRW cone calorimeter is shown in Figure 23. The internal cone exposed to the outcoupled laser beam was fabricated from OFHC copper and blackened for low reflectance. The outer shell was fabricated from low thermal conductivity lucite to reduce heat losses from the coolant water. Flow passages around the calorimeter were wound in a helical pattern to preclude local uncooled areas on the copper cone. Straightener vanes were provided at the apex to recover pressure and avoid local cavitation of the discharge water. The calorimeter was instrumented with separate turbine flowmeters and inlet and outlet thermocouples installed to produce a ΔT measurement.

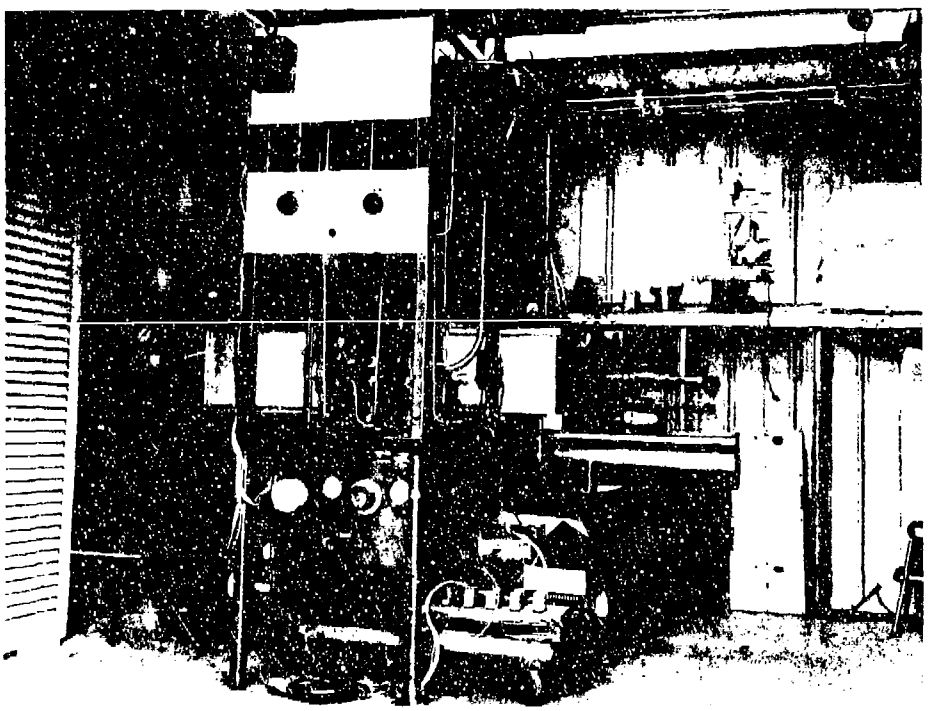

Figure 22. Mirror Enclosure Mounting

Figure 23. TRW Cone Calorimeter Installation

3. DESIGN ANALYSES

The design of the CL III laser system involved a series of parametric analyses consisting of thermochemical combustion and isentropic nozzle flow calculations followed by a fluid mechanics analysis to determine nozzle boundary layer characteristics and parallel stream mixing potentials. Finally, detailed thermal and stress analyses were performed on the selected baseline laser configuration operating under a variety of postulated test conditions.

a. Parametric Design Analyses

The design goals for the CL III laser may again be summarized as follows:

- Flexibility involving a wide range of flow conditions of both fuel and oxidizer allowing for study of effects on mixing

- Higher combustion pressures providing a flow field consistent with pressure recovery requirements and reduction of nozzle viscous boundary layers
- Nozzle exit pressures matched to laser cavity pressure. Nozzle design must include viscous boundary layer considerations
- Near stoichiometric mixture of H_2 and F in lasing cavity
- Total confinement of lasing zone gases for elimination of entrainment

The first step in the design of the actual hardware meeting the above requirements was a parametric analysis involving thermochemical combustion calculations for various values of ψ = DF + diluent/F_2 or ψ' = DF + diluent/H_2 and combustor temperatures as well as isentropic nozzle flow calculations for above conditions.

The parametric calculations were performed using well established TRW thermochemistry and nozzle flow computer programs for the H_2 combustor/injector with varying amounts of He diluent and the F combustor/injector with varying He diluent and again with N_2 diluent. Results of these calculations are presented in Figures 24 through 29.

As can be seen from the parametric curves, an aerodynamic area ratio of approximately 24/1 reasonably satisfies a wide range of ψ and ψ' for both the oxidizer and fuel cavity injectors, respectively, for a pressure ratio P_c/P_{ex} of 750 (P_c = 150 psia, P_{ex} = 10 torr). Based upon a minimum practical throat slit width of approximately 0.010, and area ratio of 30/1 (aerodynamic + displacement thickness) both fuel and oxidizer nozzles were sized identically. Using prior empirical data as a basis, a cavity diluent ratio

$$\left(\Omega = \frac{\text{total diluent + DF}}{F_2}\right)$$

of approximately 12.8 was chosen.

Several design operating points were thus selected using the above criteria. A range of operating conditions for F and H_2 cavity injectors was defined which would provide relative velocity ratios between streams ranging from 0.59 to 2.6. Absolute values of exit

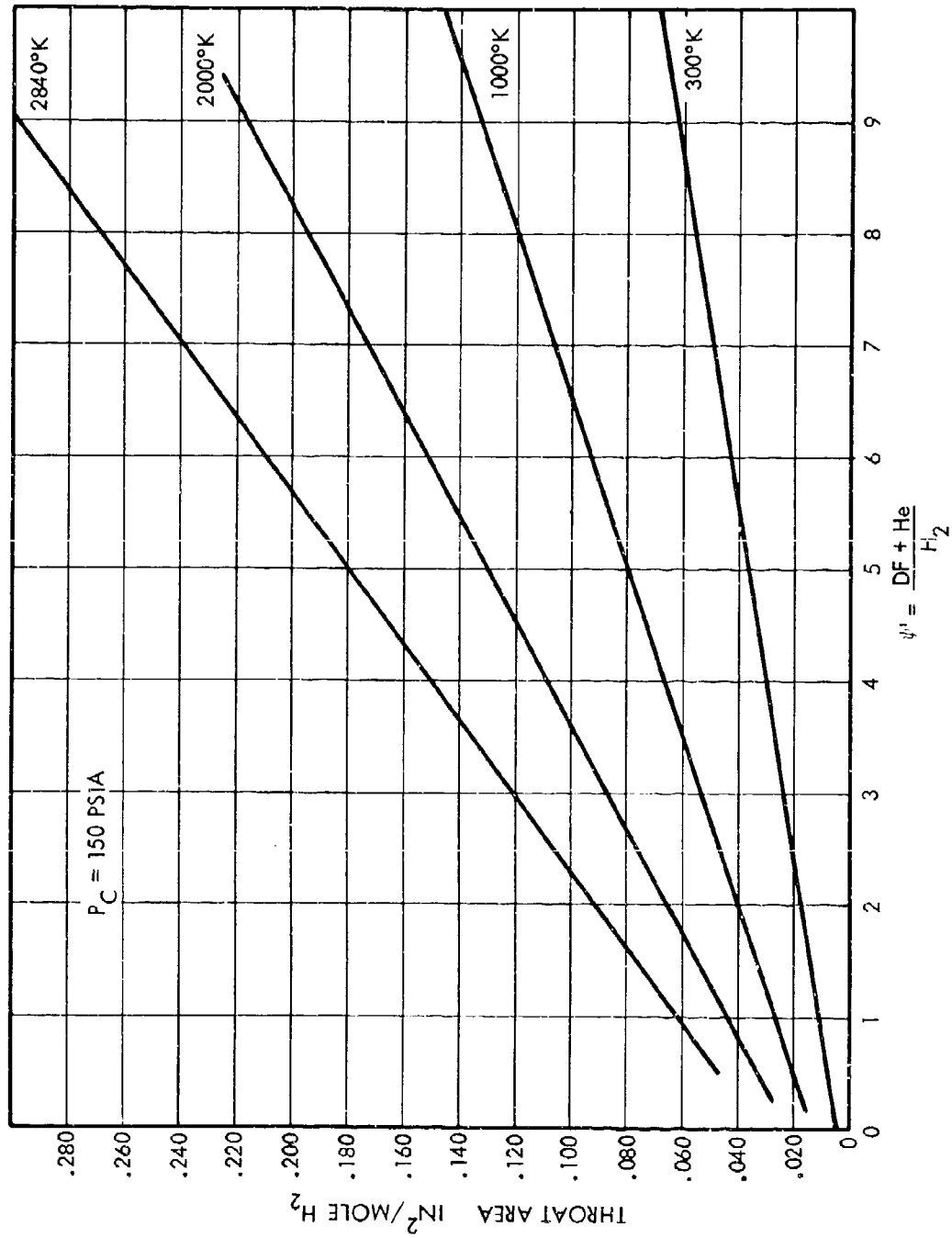

Figure 24. Cavity Fuel Injector, Throat Area vs ψ

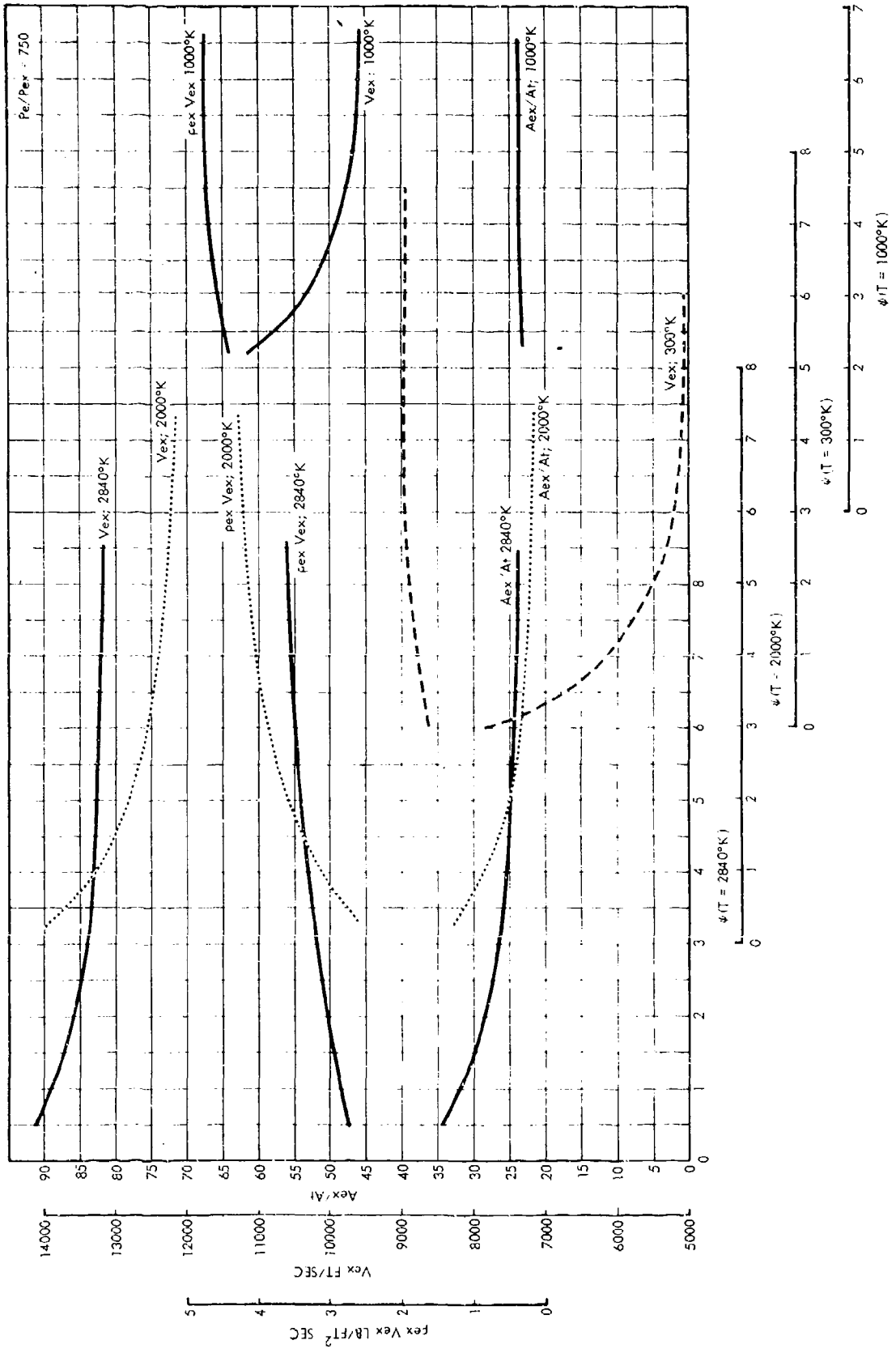

Figure 25. Cavity Fuel Injector Parametric Studies

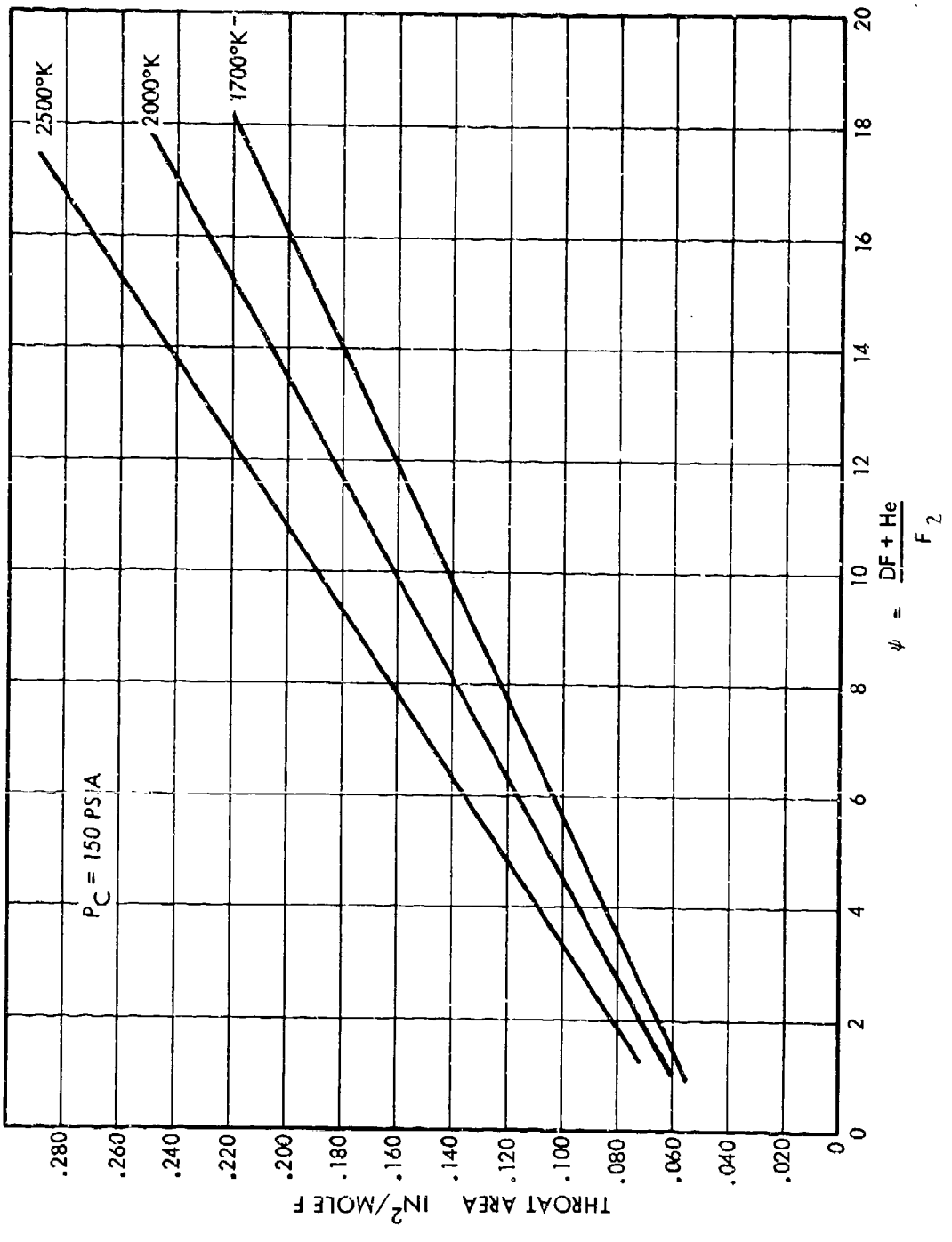

Figure 26. Cavity Oxidizer Injector, Throat Area vs ψ

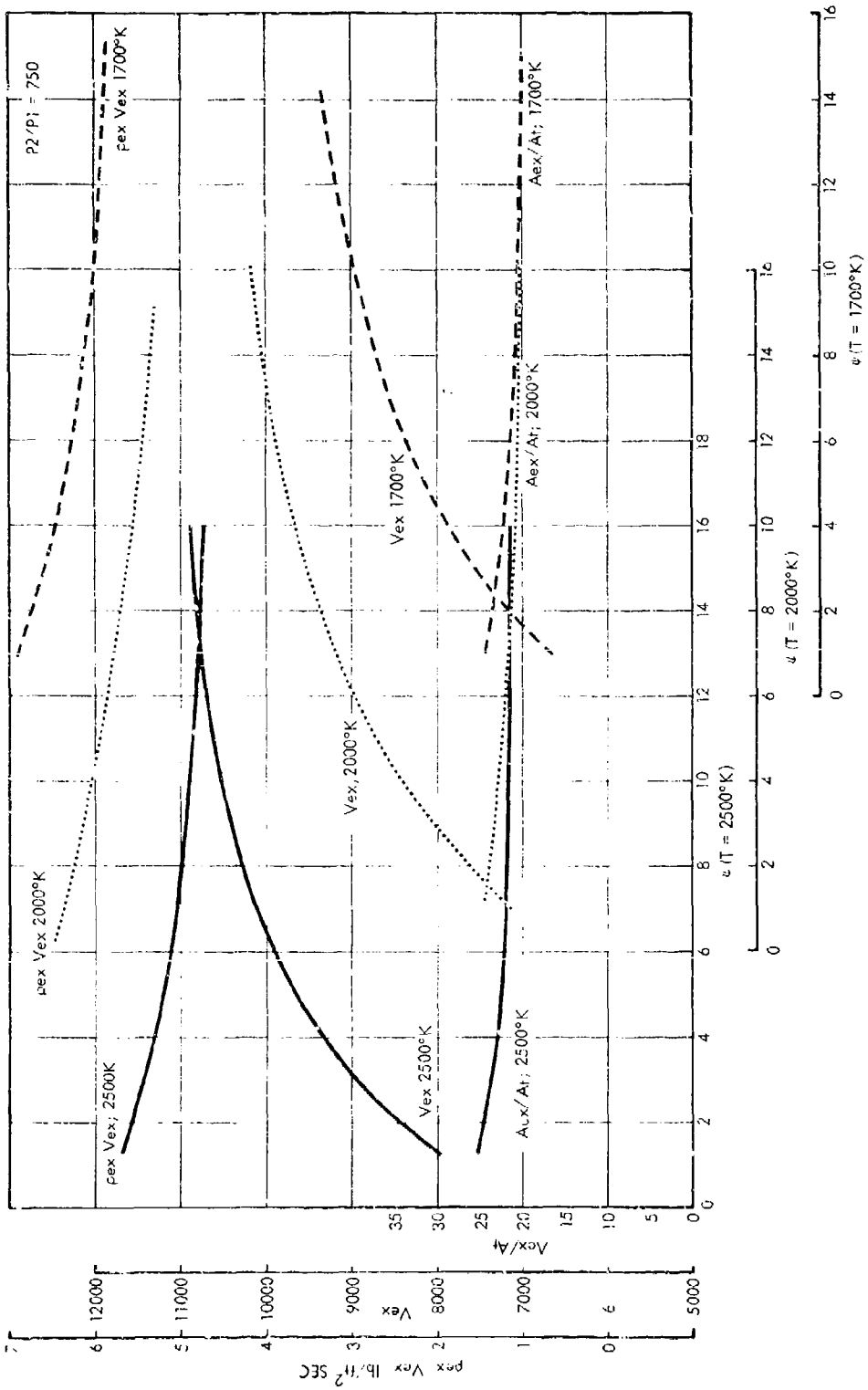

Figure 27. Oxidizer Cavity Injector Parametric Studies

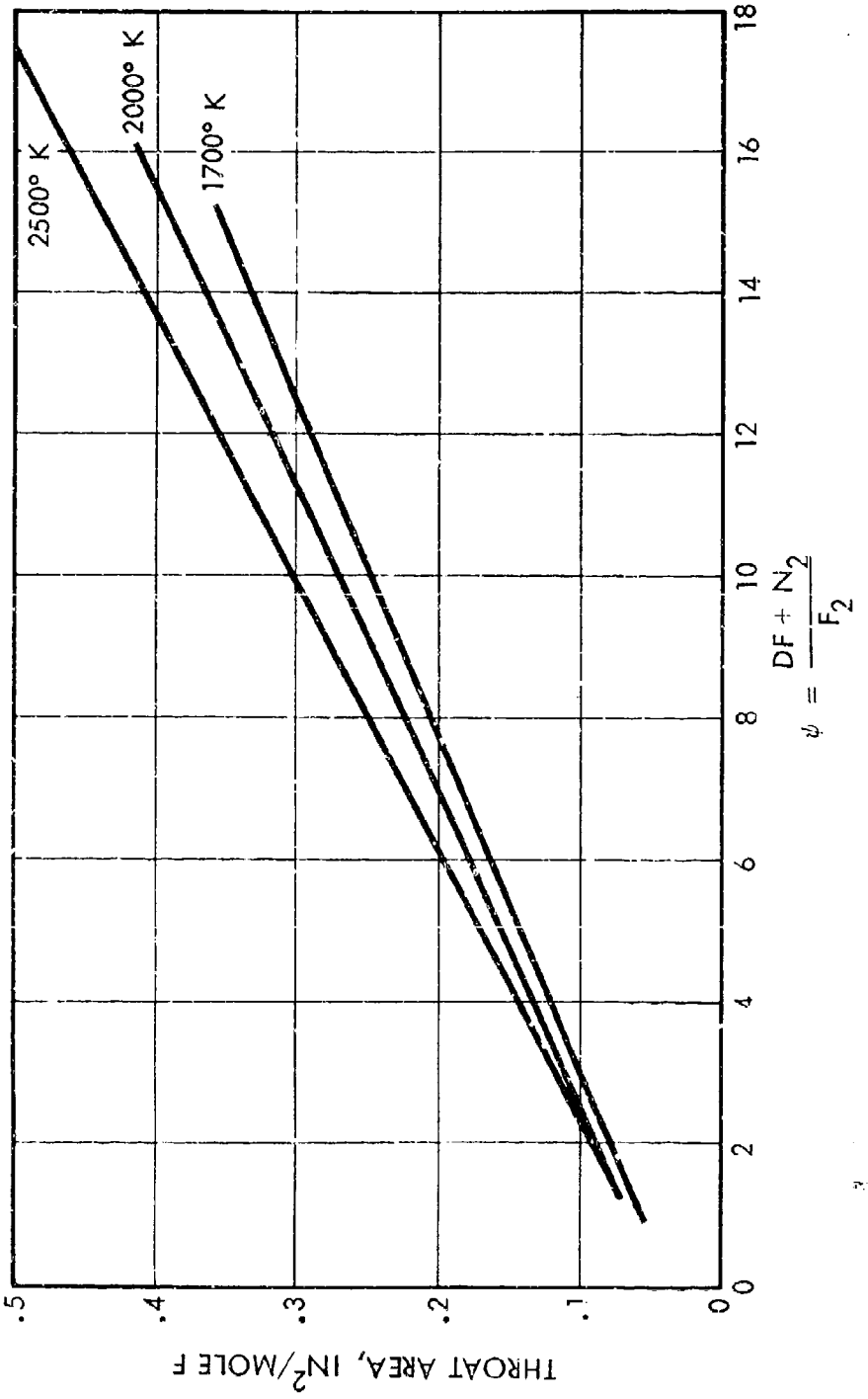

Figure 28. Cavity Oxidizer Injector (N_2 Diluent) Throat Area vs ψ

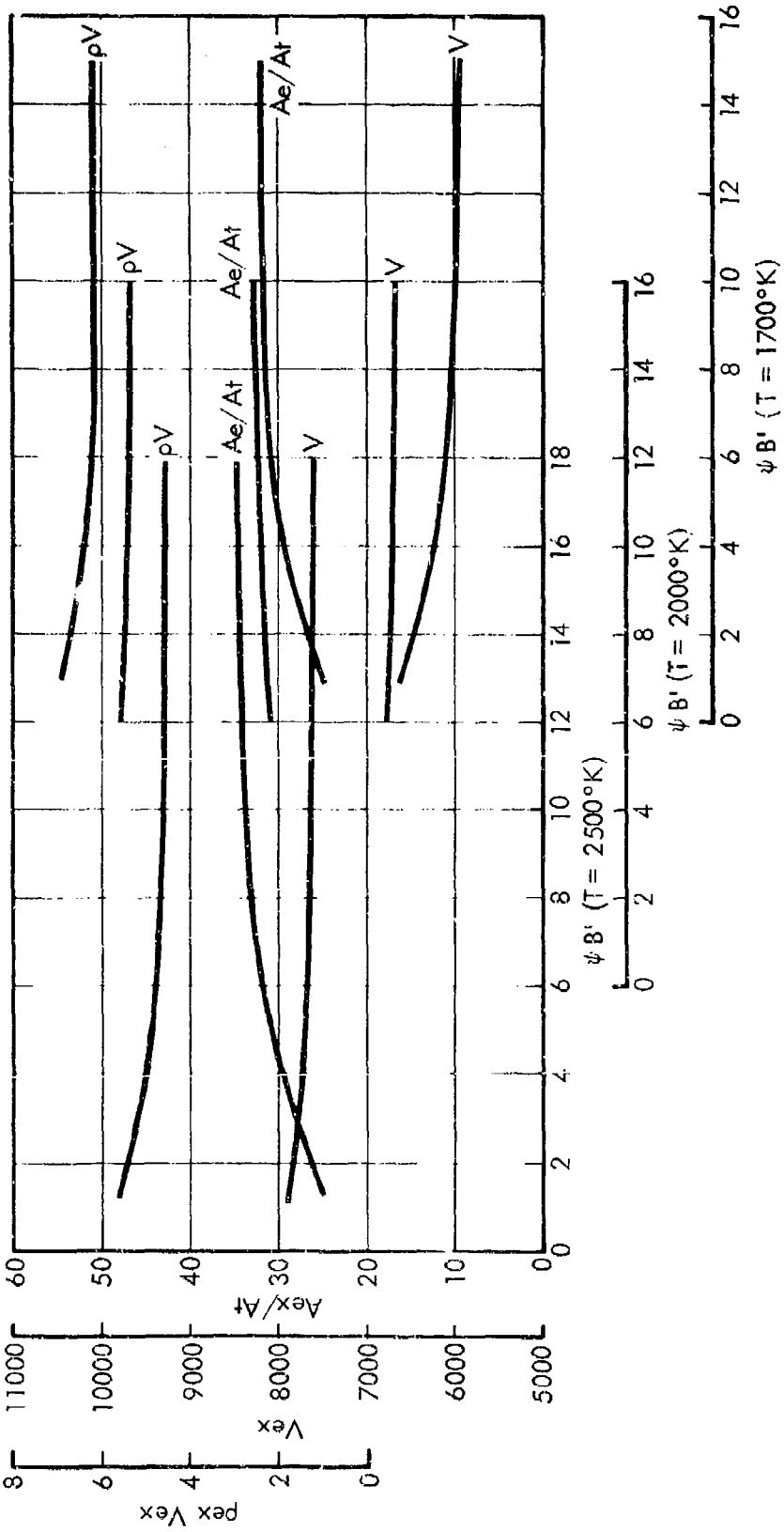

Figure 29. Cavity Oxidizer Parametric Studies, N_2 Diluent

velocity could be varied from 3100 to 10,000 ft/sec. The following section presents the analysis of the various operating conditions and summarizes the nominal conditions including molar flow rates of each constituent, the combustor temperature, the core flow exit conditions and the boundary layer properties. All cases have been corrected for estimated heat loss.

b. Fluid Mechanics Analysis

(1) Boundary Layer and One-Dimensional Mixing Calculation

Nozzle boundary layer and one-dimensional mixing analyses were performed for each of the run conditions selected from the parametric study described previously. The calculations utilized the two-dimensional nozzle boundary layer program described in Appendix III of reference 14. The properties of the mixed flow in the lasing cavity were then calculated with and without heat release. The mixing calculation is based upon an isentropic expansion of the nozzle flows from the nozzle exit static pressure (P_{ex}) to the specified cavity pressure (P_1). The expanded flows are then assumed to mix with conservation of continuity, momentum and total enthalpy. When chemical reaction is included in the mixing, it is assumed that all possible HF or DF formation occurs. The results of the computations are given in Tables VIII and IX.

The calculations of Table VIII are based upon combustor pressures of 75 psia and a laser cavity pressure of 5 torr. Calculations for each of 10 selected run conditions are included. Nozzle exit conditions, mixed flow properties prior to heat addition and flow properties following HF formation are presented.

Table IX presents six selected flow condition calculations for combustor pressures of 150 psia.

(2) Prediction of Turbulent Spreading Angles

Operating conditions which lead to rapid mixing of the fluorine-containing and hydrogen-containing streams are necessary in order to achieve maximum lasing power. Factors which influence the mixing rate are the velocity and density differences between the two streams, the respective stream Mach numbers, the heat release through chemical reaction, the wakes of the intervening boundary layers, and the geometry of the base wall separating the boundary layers at the nozzle exits. A detailed analysis of the mixing region is desirable and with some limitations is feasible, but development of a large computer code for this purpose lies outside of the scope of the present study. For this reason simplified correlations of experimental data were employed for the purpose of giving direction to the selection of the hardware geometry and flow conditions which yield the best mixing.

A condition necessary to optimize mixing is that the mixing region itself be turbulent. The mixing layer is more unstable than the boundary layer because of the presence of an inflection point in the velocity profile. Furthermore, the boundary layer is nearly transitional in the present case, and with the added vortex generators, the mixing layer should be turbulent. Assuming that this condition is fulfilled, the mixing layer is expected to grow linearly with an initial thickness as large, or less than, the gap height between nozzles. A larger thickness is more likely if vortex generators are used in the gap to destroy the two-dimensionality of the flow and thereby enhance the mixing.* The downstream extent over which the boundary layers tend to retard the mixing is also reduced for the same reason. The present analysis thus considers the mixing to be quantitatively close to predictions for uniform parallel streams of different density, velocity and Mach number. Experimental

*If the gap is simply closed by a flat base plate, the flow situation is very similar to a wake flow behind a supersonic wedge at angle of attack. The wall boundary layer flow will expand above a recirculation zone into the gap after separating from the base plate near the corner. Reattachment will occur one to two base heights downstream and a turbulent core approximately half a can height in thickness will form the origin of the mixing layer.

evidence indicates that the mixing rate is most strongly dependent on the velocity ratio between the streams.

It should be noted that the referenced spreading angle is described by a line defining the progression of 5 percent concentration of one constituent into the other. Although considerable empirical data regarding this progression exists as summarized below, detailed quantitative data regarding concentration profiles and microscale mixing within the boundaries of the turbulent mixing region is not currently available. The uncertainty regarding the length required to completely mix the reactants in the lasing cavity remains a major uncertainty in the CL III design.

Data from several sources where both streams are of equal density are presented in Figure 30 for the total included spreading angle α of the mixing layer as a function of the velocity ratio $u_2/u_1 \leq 1$; the normalizing angle α_o is the spreading angle at $u_2/u_1 = 0$ where $\alpha_o = 0.36$. A theoretical curve derived by Abramovich (Ref. 15) is also presented and is seen to represent a lower bound to the data. The curve is represented by the relation $\alpha/\alpha_o = (1 - u_2/u_1)/(1 + u_2/u_1)$ which was used in the present analysis.

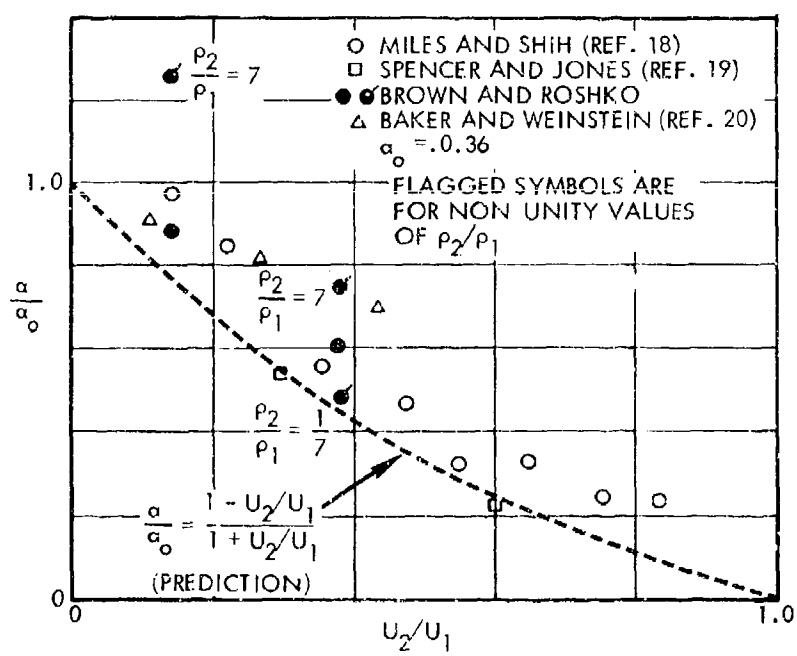

Figure 30. Effect of Velocity Ratio on Spreading Rate

The effect of density ratio on the spreading angle was studied by Brown and Roshko (Ref. 16) and data points for $\rho_2/\rho_1 = 7$ and $\rho_2/\rho_1 = 1/7$ are also presented in Figure 30. The data show that increasing the density on the low speed side of the flow increases the spreading angle. The present application lies closer to the larger value of u_2/u_1 studied and, hence, the constant density spreading angle was scaled by a multiplication factor $(1 + 0.1 \ \ n \ \rho_2/\rho_1)$ obtained from the Brown and Roshko data (Ref. 16) at $u_2/u_1 = 1/\sqrt{7}$. However, since the largest density ratios are typically less than 5, the effect on the spreading angle is at most 15 percent by this relation. Brown and Roshko also showed that the effects of Mach number difference and density difference between the two streams are separate and distinct; unfortunately, good understanding of both effects is yet to be achieved. Some effects of Mach number and chemical heat release on the mixing rate were studied experimentally by Sanderson and Steel (Ref. 17) with the conclusions that: (1) Mach number has little influence on the mixing rate, and (2) heat release can appreciably increase the rate when the velocity difference is small. No corrections for Mach number and heat release are considered here.

Predicted spreading angles for several hypothetical condition are shown in Table X and a typical example is shown graphically in Figure 31.

c. Thermal and Stress Analyses

(1) Thermal Analysis

Heat loss estimates for the CL III were arrived at primarily by scaling from the CL II device (Ref. 1). Calculations of maximum wall temperatures were made using a thermal model and grid network.

Prior to beginning the heat loss analysis, the CL II heat loss results were summarized. Data from the CL II 1 x 7 nozzle was used. Figure 32 presents the CL II 1 x 7 combustor and nozzle heat loss data over a range of total mass flow rates.

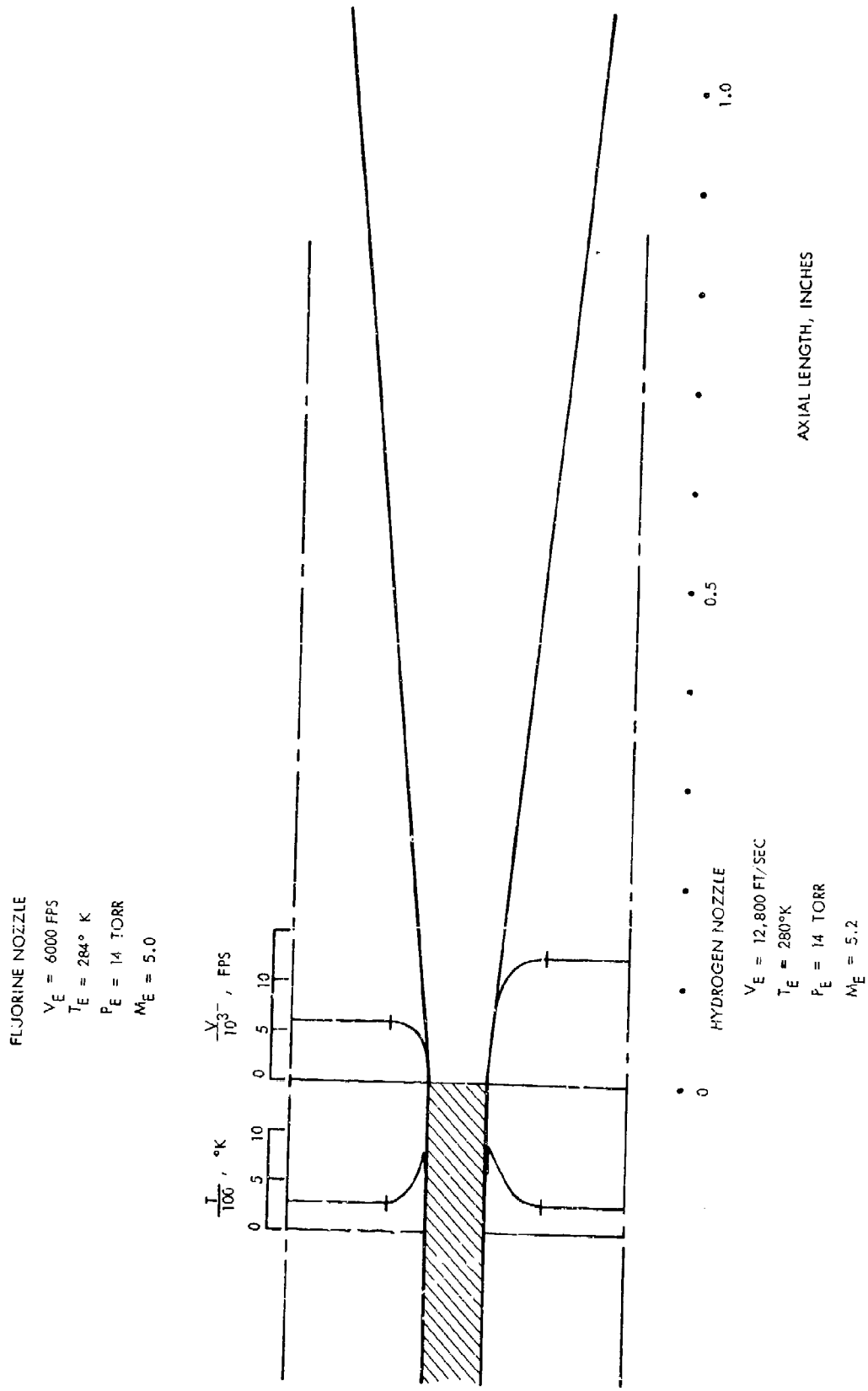

Figure 31. Typical Hypothetical Spreading Angles

Table X. Chemical Laser Design Study

Case	V_e	T_e	Average Molecular Weight	P_e	ρ_e	M_e	$\rho_e V_e$	Total Included Spread Angle α
	ft/sec	^oK		psia	lb/in^3		lb/in^2-sec	
I F	6,540	229	19.6	.186	$.476 \times 10^{-6}$	5.3	.037	.11
I H_2	11,750	208	6.2	.231	$.206 \times 10^{-6}$	5.5	.029	
II F	9,700	151	8.1	.192	$.308 \times 10^{-6}$	6.0	.036	.07
II H_2	13,900	477	5.8	.203	$.074 \times 10^{-6}$	4.5	.012	
III F	10,340	184	8.4	.141	$.192 \times 10^{-6}$	5.9	.024	.09
III H_2	6,360	66	2	Jet	$.092 \times 10^{-6}$	4.2	.007	
IV F	6,000	284	24.7	.287	$.75 \times 10^{-6}$	5.0	.054	.16
IV H_2	12,800	280	6.1	.268	$.174 \times 10^{-6}$	5.2	.027	
CL II F	9,970	320	10	.068	$.062 \times 10^{-6}$	4.3	.007	.08
CL II H_2	6,360	66	2	Jet	$.092 \times 10^{-6}$	4.2	.007	

e ≡ inviscid core

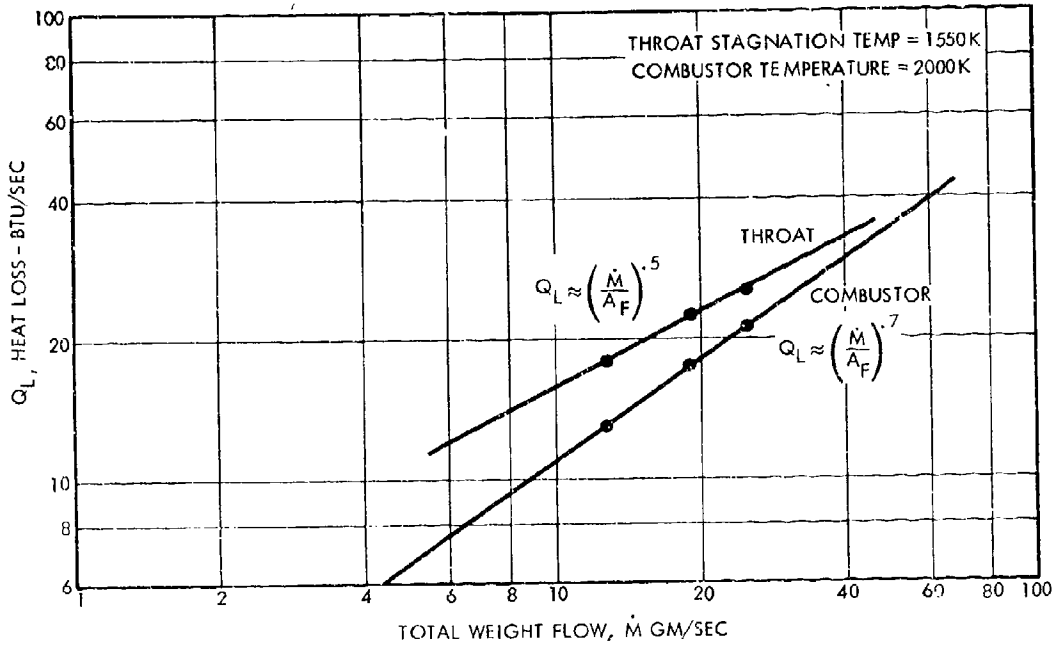

Figure 32. CL II Heat Loss/Total Weight Flow Correlation

The combustor losses were scaled to CL III flows directly using the exponent derived from the slope of the curve of Figure 32 ($Q_L \approx \dot{m}^{.7}$). For determining the plenum losses, the combustor scaling criteria again was applied taking into account the flow area, wetted perimeter, hydraulic diameter, and surface area factors as given in equation (17). Throat losses were scaled from the CL II 1 x 7 results using equation (18) and the slope of the curve from Figure 32 ($Q_L \approx \dot{m}^{.5}$). The following relations derived from the Bartz pipe flow heat loss

equation with the $\frac{\dot{m}}{A_F}$ exponent derived empirically from Figure 32 were used for scaling to the CL-III run conditions:

Combustor and Plenum Heat Loss

$$Q_{L_{CL-III}} = Q_{L_{CL-II}} \left(\frac{\dot{m}_{CL-III}}{\dot{m}_{CL-II}}\right)^{.7} \left(\frac{A_{f_{CL-II}}}{A_{f_{CL-III}}}\right)^{.7} \left(\frac{D_{H_{CL-II}}}{D_{H_{CL-III}}}\right)^{.2}$$

$$\left(\frac{A_{s_{CL-III}}}{A_{s_{CL-II}}}\right) \frac{(T_c - T_w)\ CL-III}{(T_c - T_w)\ CL-II} \tag{17}$$

where

A_f = Flow cross section area

D_H = 4 Af/wetted perimeter

A_s = Surface area in contact

T_c = Gas temperature

T_w = Wall temperature

(a) Nozzle Heat Loss

$$Q_{L_{CL-III}} = Q_{L_{CL-II}} \left(\frac{\dot{m}_{CL-III}}{\dot{m}_{CL-II}}\right)^{.5} \left(\frac{A_{f_{CL-II}}}{A_{f_{CL-III}}}\right)^{.5} \left(\frac{D_{H_{CL-III}}}{D_{H_{CL-II}}}\right)^{.2}$$

$$\left(\frac{A_{s_{CL-III}}}{A_{s_{CL-II}}}\right) \frac{(T_c - T_w)\ CL-III}{(T_c - T_w)\ CL-II} \tag{18}$$

Table XI summarizes the estimated heat loss values for a typical run condition (Number 1) given in Table VII.

Table XI. Estimated Heat Losses for CL III, Case I (Btu/sec)

	Combustor Heat Loss	Plenum Heat Loss	Throat Heat Loss	Total
H_2 Injector	15	24	18	57
F Injector	26	43	21	90

Calculations were then performed to determine the margin on the plenum cooling water passage design for burnout considerations. Using Case 1 from Table IX at full 150 psia combustor pressure, the estimated heat losses to the plenum cooling water is:

H_2 side, Q_L plenum = 40 Btu/sec

F side, Q_L plenum = 69 Btu/sec

Total 109 Btu/sec

the heat flux into 0.100 and 0.050 cooling passes reduces to

Q_L/A where $A = \pi D N_1 L + \pi D N_2 L$ N_1 = number of 0.100 diameter passages

N_2 = number of 0.050 diameter passages

$$\pi D_1 N_1 L = \pi 0.100 \times 41 \times 0.6'' = 7.74 \text{ in}^2$$

$$\pi D_2 N_2 L = \pi \times 0.050 \times 41 \times 0.6 = 3.86 \text{ in}^2$$

Total 11.60 in^2

$$\text{Heat flux} = 109 \text{ Btu/sec}/11.60 \text{ in}^2 = 9.4 \text{ Btu/sec/in}^2$$

$$= 4.9 \times 10^6 \text{ Btu/hr/ft}^2$$

The empirical equation of Gunther [Trans. ASME 73, 115 (1951)] was used to determine the critical burnout heat flux

$$Q/A_{max} = 7000 \sqrt{V} \ \Delta T \text{ sat}$$

where

V = 100 ft/sec

ΔT sat = T sat - T water = $330^{\circ}F - 90^{\circ}F = 240^{\circ}F$
($330^{\circ}F$ corresponds to outlet pressure of 100 psia)

$Q/A_{max} = 7000 \sqrt{100} \ 240 = 16.8 \times 10^{6}$ Btu/hr/ft^2

Comparing the 4.9×10^{6} value against the critical 16.8×10^{6}, a safety factor of 3.4 exists. This margin is reduced as combustor temperatures are increased, and should be reevaluated if significantly higher operating temperatures are contemplated.

Apart from estimates of expected heat loss needed for combustor scaling and system studies, the CL III thermal effort also involved a procedure of analyzing critical "hot spots" in the design under worst case assumptions. While it was recognized that the resulting calculated temperatures and consequent thermal stresses were perhaps more severe than would be encountered in the actual device, the focus was on ensuring thermal and structural integrity of the unit. It was expected that the calculated temperatures would be reviewed as test data on the unit accumulated. Accordingly, local thermal models of the cavity injector sidewall, throat and backwall were constructed and used to compute temperatures in the copper walls. As would be expected from Figure 33, the maximum temperature on the cavity injector sidewalls was found to occur half way between water coolant passages at the surface exposed to hot gas (node 2 of the sidewall thermal model). Assuming a combustor wall gas side film coefficient of 0.9×10^{-3} Btu/in^2-sec-$^{\circ}$R and hot gas recovery temperatures of 3200°, 2820° and 1500°K, the temperature of node 2 was found to be 928°, 841° and 512°F, respectively. Node 2 at 928°F became the maximum temperature expected at any point on the cavity injector walls. Figure 34 shows the cavity injector throat

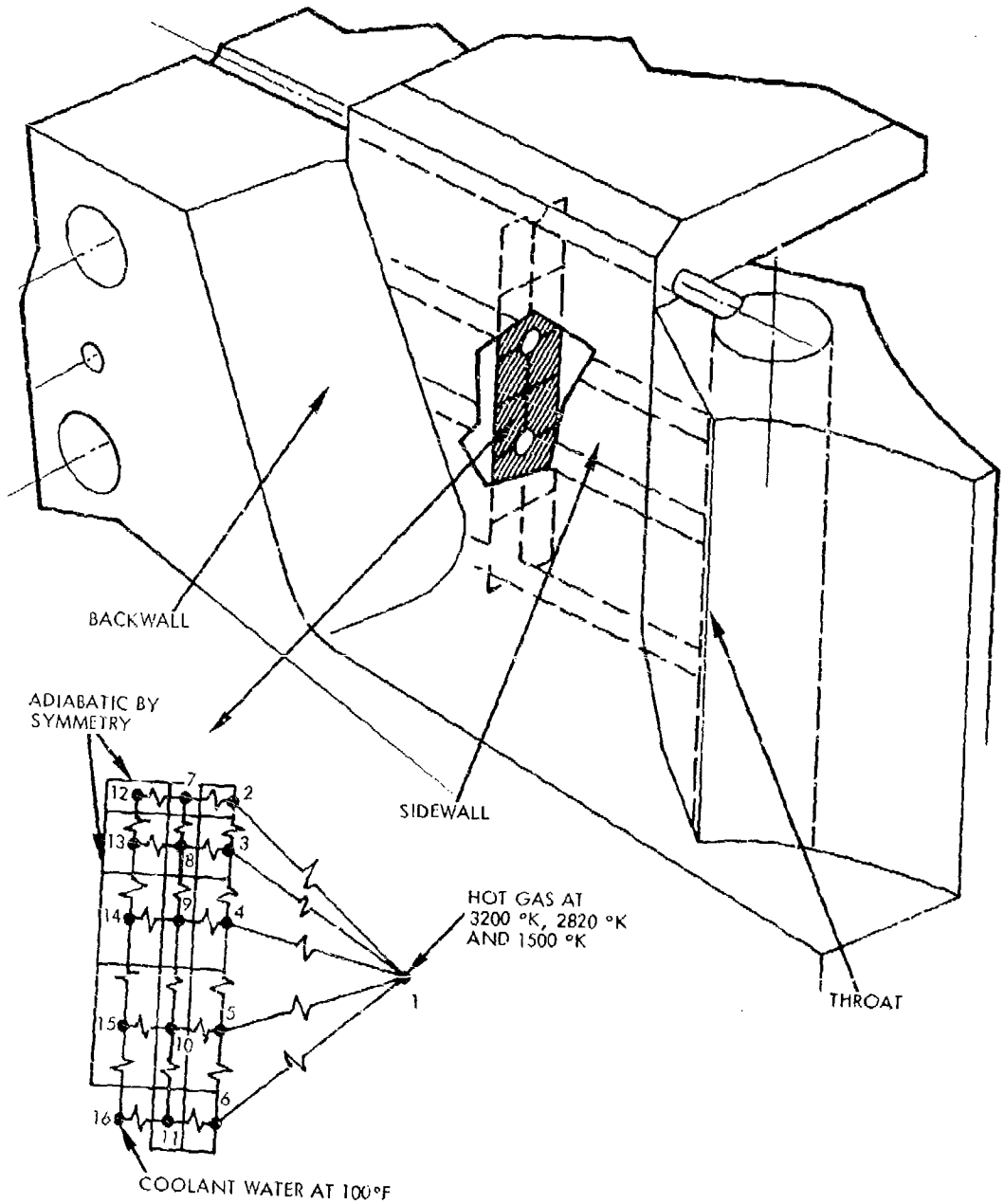

Figure 33. Cavity Injector Sidewall Thermal Model

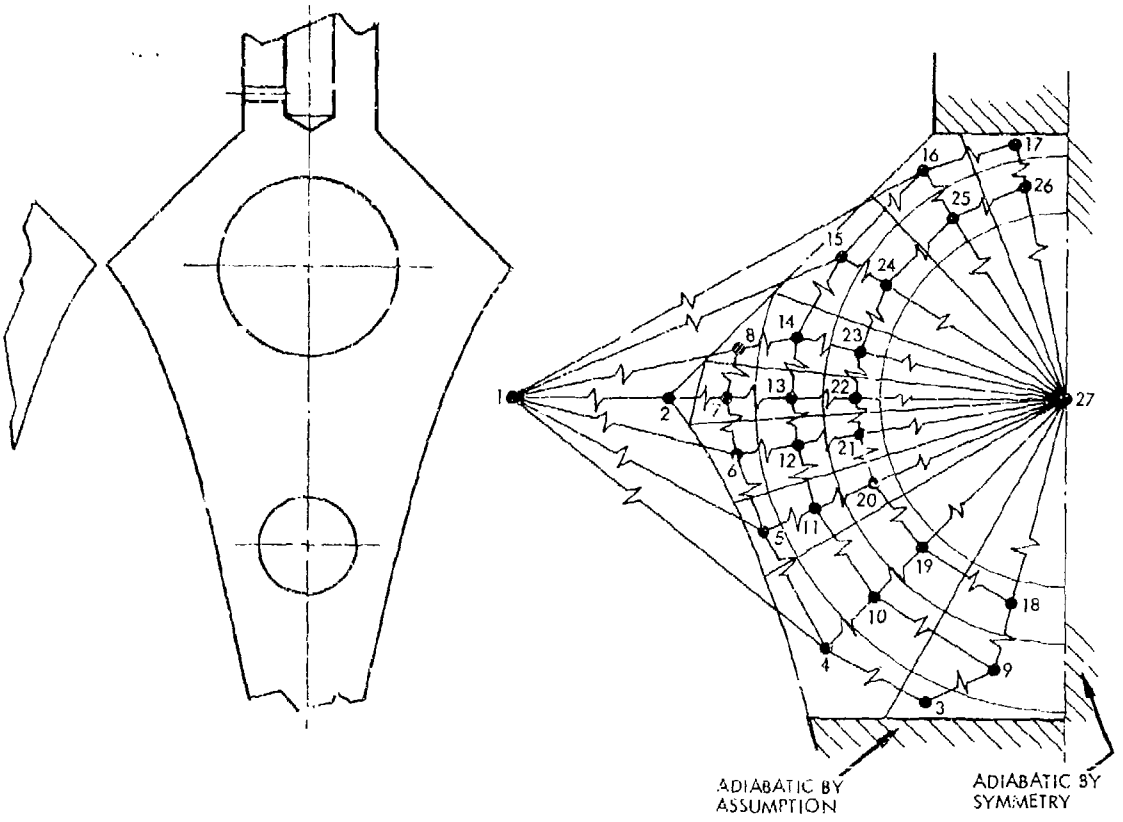

Figure 34 Cavity Injector Throat Thermal Model

thermal model. A hot gas recovery temperature of 2000°K and a throat heat transfer coefficient of 3.5×10^{-3} Btu/in^2-sec-°R calculated from the Bartz equation was used in running this model. Nucleate boiling data on 100 psia, 100°F water flowing at 100 feet per second was taken from NASA TND 1214. With these assumptions, a maximum gas side surface temperature of 435°F (node 2) and a maximum water passage surface temperature of 315°F (node 22) were found from the model.

A third thermal mod s constructed representing the center of the cavity injector backwall (Figure 35) but this point was found to be less critical (lower temperature) under comparable assumptions than the sidewall. A maximum surface temperature of 558°F was calculated in this area assuming a 3200°K recovery temperature and a 0.9×10^{-3} Btu/in^2-sec-°R film coefficient. This is some 370°F cooler than the sidewall surface under the same conditions.

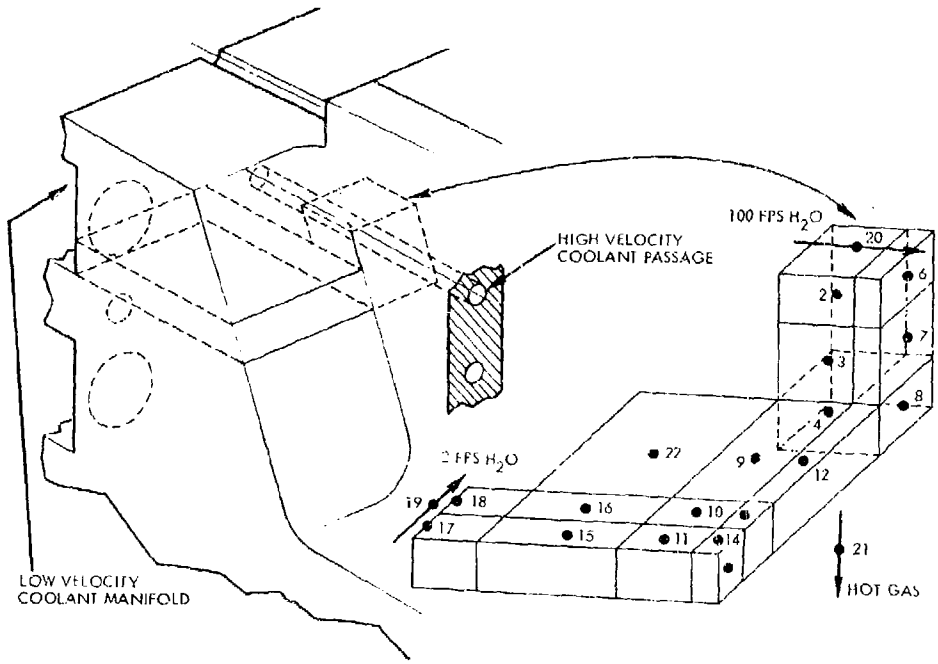

Figure 35. Cavity Injector Backwall Thermal Model

(b) CL III Stress Analysis

The structural analysis of CL III focused primarily on the high temperature areas of the cavity injector, although rough sizing calculations were made to estimate conservative wall thicknesses for external pressure loadings on the optical cavity, salt window and plexiglass viewing windows.

The cavity injector design was analyzed first from the standpoint of primary pressure stress producing fracture or other catastrophic failure and second with respect to the probable number of test firings sustainable until the onset of thermal fatigue cracking. A limit coolant water pressure of 150 psia was used in the analysis. Limit hot gas pressure was also set at 150 psia in either or both sets of adjacent fuel and oxidizer rich compartments. A proof factor of 1.5 and a burst factor of 2.0 on limit pressure was assumed.

Figure 36 shows the as-brazed material properties of OFHC copper selected for the analysis.

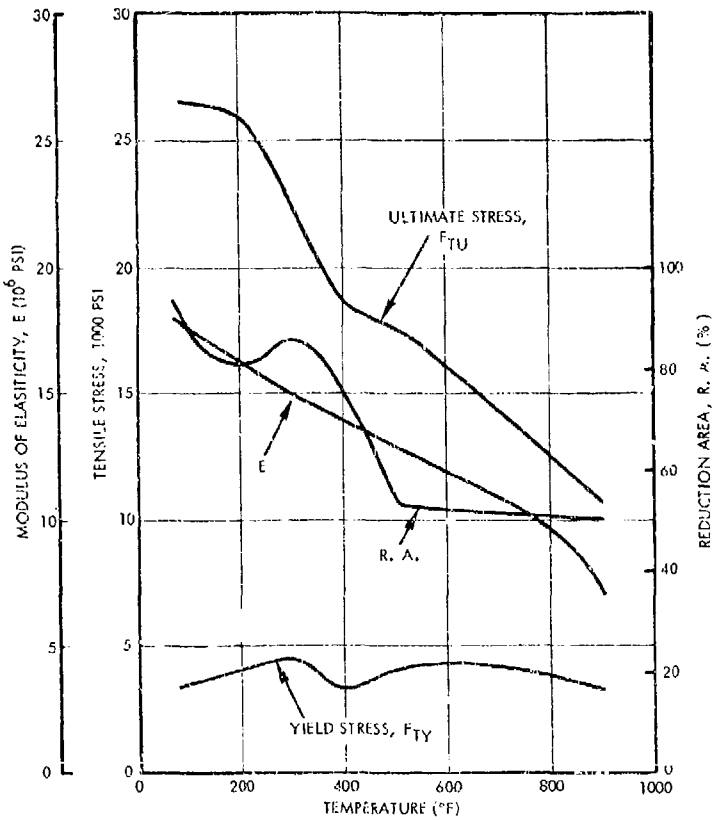

Figure 36. Mechanical Properties of OFHC After Braze Cycle

Sixty percent of the tensile strength (19,000 psi) of pure gold at room temperature was used for the ultimate shear strength of all braze joints. The actual shear strength of such joints will depend on gap, degree of alloying with base metal, cleanliness, etc. The above value of 11,400 psi is thought to be conservative for well made joints of 100 percent area coverage.

With these assumptions, the several drilled hole coolant passages and braze plugs show very high margins with the modest internal pressures applied (again assuming good braze points). The minimum margin for internal pressure in the manifolds occurs at the sides of the 347 CRES water mainfold closeouts at the back of the injector, where the proof margin of safety approaches 36 percent in bending. The critical internal pressure condition for the hot gas occurs in the sidewalls between

fuel and oxidizer rich compartments when only one set of compartments is flowing (150 psia across wall). Under this condition the ultimate margin of safety equals 169 perce but the applied stress approaches yield at the edge of the sidewall. s the stress is bending rather than direct tension, and the ultimate strength is much greater than yield, the only result will be a slight bulging of the compartment walls. The worst case throat area change under this operating condition is 3 percent neglecting the wall thickening at the throat. Including this additional stiffness, the area change is probably about 1 percent.

In order to determine the allowable number of tests on the hardware under thermal cycling, the uniaxial tensile properties of Figure 36 were used to construct an estimate of the low cycle fatigue properties of OFHC copper (Figure 37). The Universal Slopes correlation of S. S. Manson, et al, which was used as low cycle fatigue data were unavailable for the as-brazed condition. The worst case thermal analysis had indicated a maximum temperature of 928°F on the compartment side-walls midway between coolant passages. Assuming that the thermal

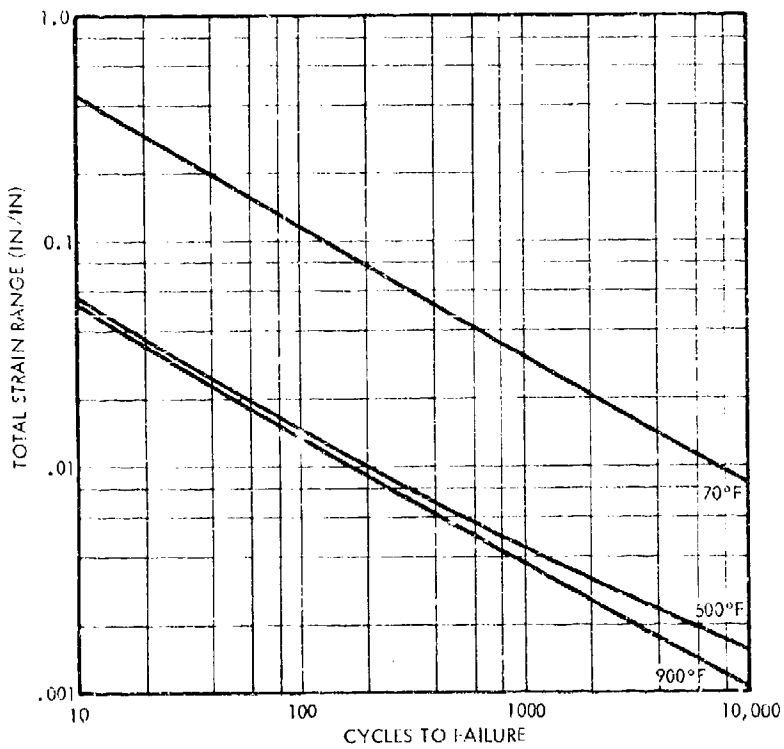

Figure 37. Fatigue Cycle Life of OFHC Copper, Post-Braze Cycle

expansion resulting from this hot spot is fully biaxially restrained by the surrounding colder material, an equivalent mechanical compressive strain of 0.0172 in/in would result. Figure 37 indicates a cycle life of about 67 tests for cycling between this maximum temperature and ambient conditions.

The conditions assumed in the worst case thermal analysis were more severe than those actually encountered by the hardware. The 3200°K gas side temperature was not included in the test matrix, and the 512°F wall temperature corresponding to the 1500°K gas temperature was typical of most of the CL III operating conditions. Under these conditions the fatigue cycle life probably exceeds the useful life of the device as an experimental test article.

SECTION IV

EXPERIMENTAL EVALUATION

The third task of the subject contract consisted of an Experimental Evaluation of the new CL III Laser Hardware.

An initial 2 weeks of testing was performed under this program. Subsequent testing will be accomplished under the follow-on contract and will be reported later. For the first several runs in the initial test series, a nominal combustor pressure of 75 psia was selected. This was done to accomplish screening and mixing evaluations at a more conservative laser cavity pressure of 5 torr and at a reduced reactant consumption rate. Later in this initial test series combustor pressures of up to 93 psia were used. The test series consisted of combustor checkouts and determination of heat loss values from each combustor, infrared scans of the cavity flow field under various flow conditions, orange glow photography, and an initial measurement of laser power.

1. TEST SUMMARY AND DIAGNOSTICS

The objectives of the CL III test series were as follows:

(1) Checkout of the CL III cavity injector and combustor systems including H_2 preheater

(2) Evaluation of four operating conditions with relative stream velocity ratios of F and H_2 ranging from 0.59 to 2.61

(3) Determination of turbulent mixing spread angles as a function of relative stream velocities

(4) Correlation of orange glow photography and IR scan results

(5) Determination of laser power for selected flow conditions

Twenty-five tests of the CL III device were performed. The flow conditions for each of the tests are summarized in Table XII. Included in the table are the combustor flows, combustion pressure, combustor temperature, molar ratios including ψ and Ω, and nozzle exit properties including exit velocity, temperature, pressure and boundary layer properties.

The initial tests, HB5-308 through -318, were performed at approximately 60 psia combustor pressure and provided a checkout of the laser hardware and IR scanner apparatus. Difficulties such as IR scanner data acquisition and facility pumping system operation were encountered and resolved.

Tests HB5-319 through -323 provided data on four widely varying conditions of relative H_2 and F stream velocity. Detailed IR scans similar to those taken for the CL II device were obtained. Two of these conditions were later repeated for acquisition of full field orange glow photos (tests HB5-341 and -342). Table XIII summarizes the test runs involving the principal diagnostic methods and resulting velocity ratios.

Table XIII. Summary of Principal Diagnostics Taken in Initial Test Series and Significant Flow Conditions

Test Numbers		Velocity Conditions		
Full Orange Glow Photos	IR Scans	F Velocity (ft/sec)	H_2 Velocity (ft/sec)	Velocity Ratio V_F/V_{H_2}
		5945	8531	0.69
		7819	8609	0.90
HB5-341	HB5-319 HB5-320	5699	9633	0.59
HB5-342	HB5-321	8271	5207	1.6
	HB5-322	8133	3114	2.61
	HB5-323	8271	9633	0.86

Figure 22 illustrated the test setup with the IR scanner in place on the CL III laser cavity. A discussion of the IR scanner results and comparison with the orange glow photos is presented in the subsequent section. Also included is a discussion of the observed mixing angles compared to those predicted in Section III, 2, a(2).

Tests HB5-324 through -331 were performed for initial power measurement. The stable cavity mirrors described in Section III were used for this determination. A water-cooled calorimeter located behind the flat hole outcoupling mirror was used for power measurement.

Output power was less than 500 watts for all tests. Several major problem areas were indicated and are discussed in Section IV.3. These problem areas will be further addressed under the technology follow-on program.

The IR scanner equipment was designed under the TRW HF Laser Technology Study to provide data for cavity flowfield visualization based upon the total infrared emission of HF* in the 2.7 micron band.

Details of the IR scanner apparatus, the experimental measurement technique and the various options for data presentation are described fully in reference 21. However, a few minor modifications were made for the CL III measurements, primarily to improve the system frequency response, and to provide a means of accurate spatial reference between successive linear scans in the computer programs which are used for data reduction and presentation. Improved spatial reference between scans was achieved by means of an electrically heated wire stretched across the scanner frame near the focal plane of the optics and in a position such that the signal pulse generated in the detector circuit can be used to trigger the start of each scan in either the oscilloscope or computer plotted data presentations. A small tungsten lamp was also located above the centerline of the nozzle bank and served to orient the visual data presentations; the intensity pulse caused by this lamp was readily identified in the data, and in each case located the center of the flow field at the upstream end adjacent to the nozzle injector assembly.

As in the previous experiments, the IR scanner data for the CL III tests are presented in the form of real time oscilloscope traces and computer generated plots.

Figures 38 through 57[†] present typical IR scans for tests 319 through 323. For clarity and ease of data interpretation, additional data plots displaying only every tenth linear scan of the complete raster are included.

[†] The square wave noise evident in these figures was caused by the tape recorder not the IR scanner.

In each case, the HF intensity distribution in the flow field is shown as a series of linear scans forming a raster display, with the band intensity being represented on a linear scale by the displacement along the ordinate axis; in the computer generated plots each successive scan is itself displaced along both the ordinate and abscissa to produce a pseudo perspective visualization of the flow field.

A blackbody calibration of the IR scanner was made using the technique described in reference 1. Because of the change in the detector circuitry made for improved frequency response, the absolute response (volts) of the IR scanner as used in CL III tests was reduced by approximately 1/10 as compared to the earlier CL II tests. However, this was offset by the spatial resolution which was increased to approximately 3 mm for these tests compared with the resolution of 1 mm used in obtaining CL II data. Overall the IR scanner sensitivity was essentially unchanged and was 0.110 volt/watt cm^{-2} $ster^{-1}$ for the CL III data presented in this report; the sensitivity was 0.102 volt/watt cm^{-2} $ster^{-1}$ for the CL II tests. It should be noted that the increased spatial resolution element of 3 mm used in obtaining CL III data is still less than the nozzle spacing of about 8.5 mm for this injector configuration, and good spatial data were obtained for the CL III flow field.

In principal, features of the intensity distribution along a given scan line can be identified readily with the nozzle injector geometry. This is shown in Figure 58 where intensity minima are found to correspond to the

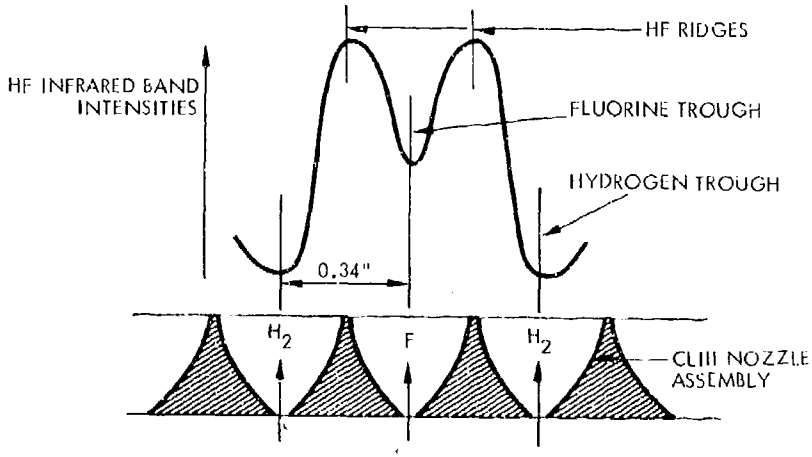

Figure 58. Schematic IR Intensity Profile in CL III Flow Field

centerlines of both the hydrogen and fluorine jets, while intensity maxima are seen at their adjacent boundaries. These features generally persist throughout the cavity flow field and generate well defined streamlines parallel to the flow direction which we have referred to as the hydrogen and fluorine troughs, and the HF ridges, respectively.

Table XIII summarized the calculated velocities of the fluorine and hydrogen injected into the CL III cavity for each of the IR scanner tests. As shown in the table, the ratio of these velocities was varied over a range of 0.59 to 2.61, and for four representative tests we have plotted sets of intensity profiles along typical flow streamlines, Figures 59 through 62.

These intensity profiles are the smoothed and averaged curves obtained for each test case by first plotting the data from 6 to 10 individual streamlines in each flow field using the computer plots of Figures 38 through 57.

The IR scanner data were also reduced through an intensity modulation mode to produce a video picture comparable to the orange glow photos. Figures 63 and 64 are the visible light photography (test 341) and IR pictures (test 319) for an identical set of flow conditions (refer to Table XII). Figures 65 and 66 present similar data for tests 342 and 321, respectively. The similarity of the pictures indicate the utility of the visible light photography as a diagnostic of the flow field.

Figures 67 and 68 are the side view visible light photos of tests 341 and 342.

2. ANALYSIS OF DIAGNOSTIC DATA

The primary objective of the initial test series with the CL III laser system was the correlation of the mixing predictions with the observed phenomena in the actual flow field. In this section, we attempt to examine the flow field structure by observation of the visible light photos and IR scanner presentations shown in Section IV.1.

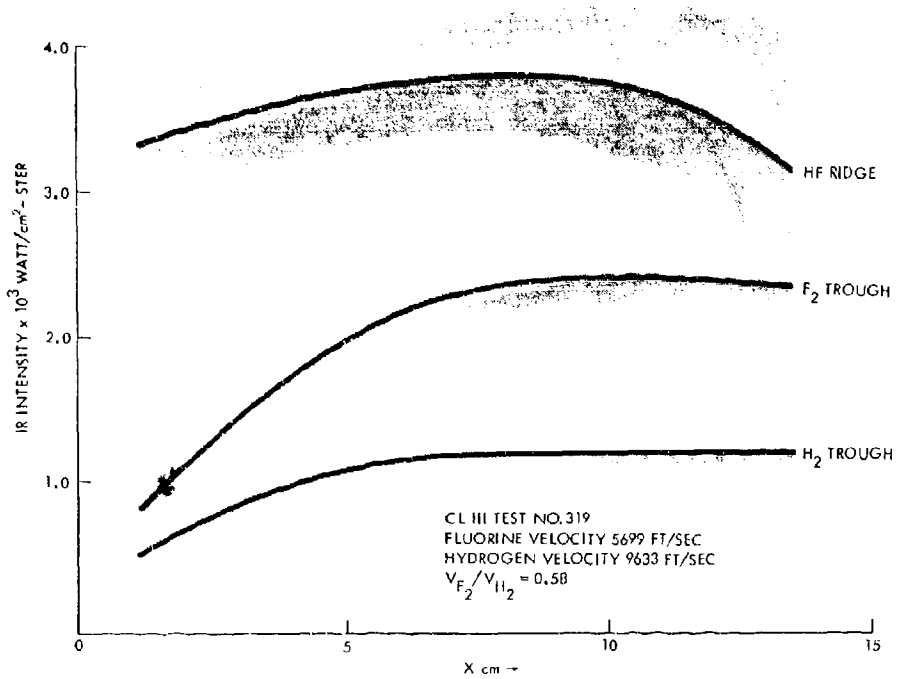

Figure 59. IR Intensity Profiles, Test 319

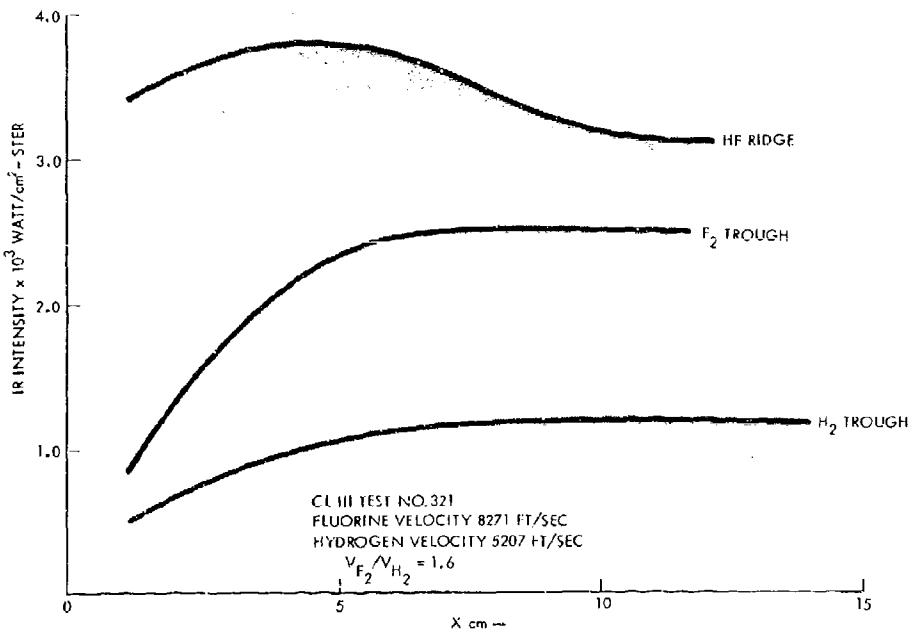

Figure 60. IR Intensity Profiles, Test 321

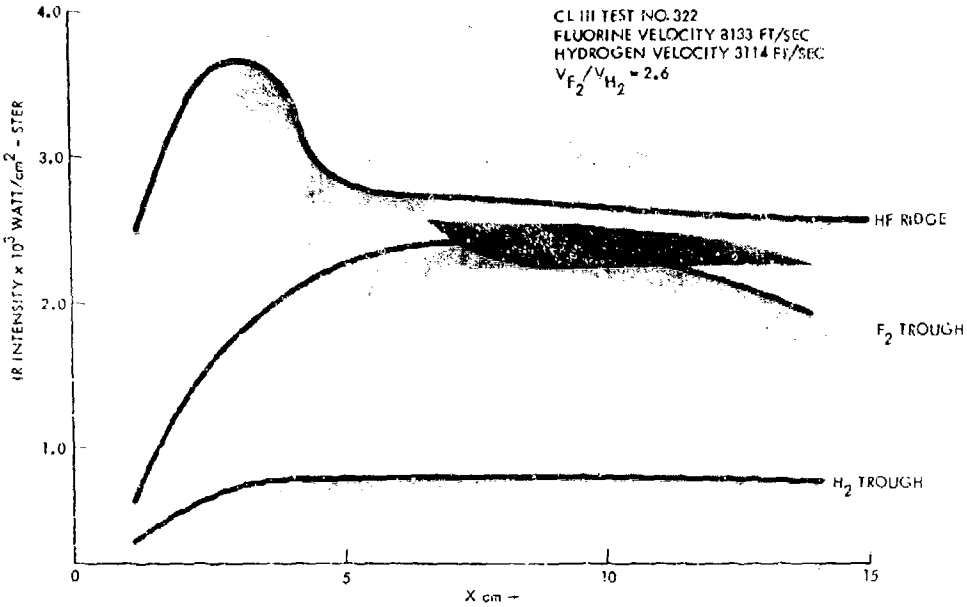

Figure 61. IR Intensity Profiles, Test 322

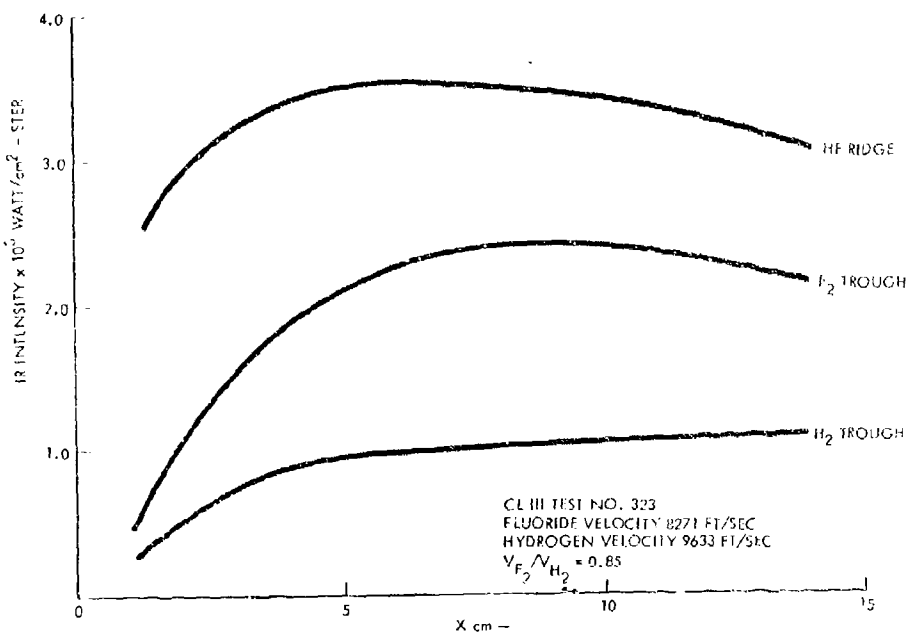

Figure 62. IR Intensity Profiles, Test 323

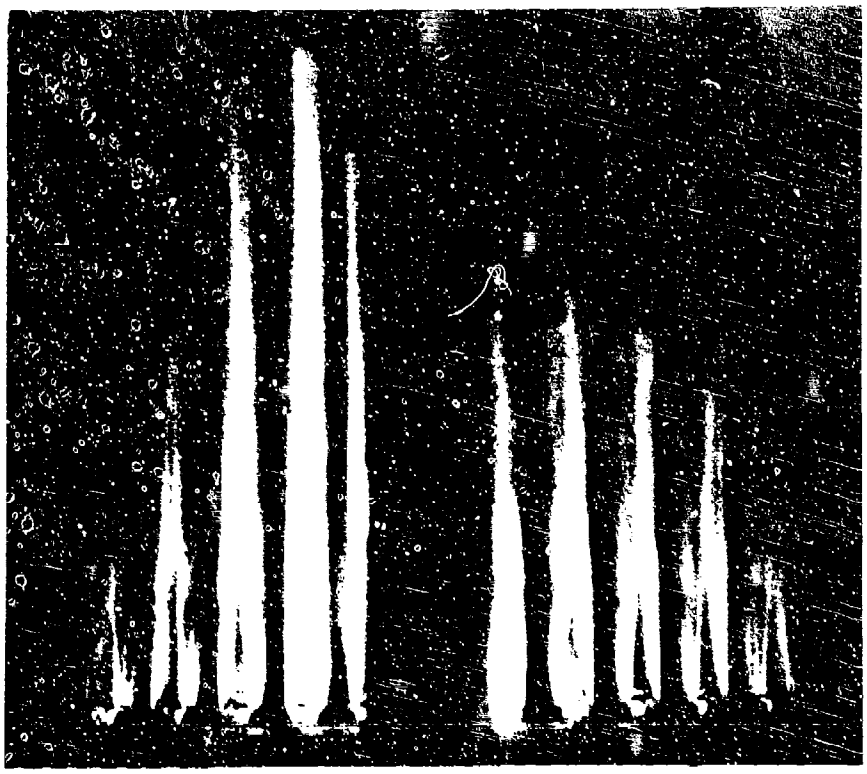

Figure 63. Visible Light Photo of Test 341

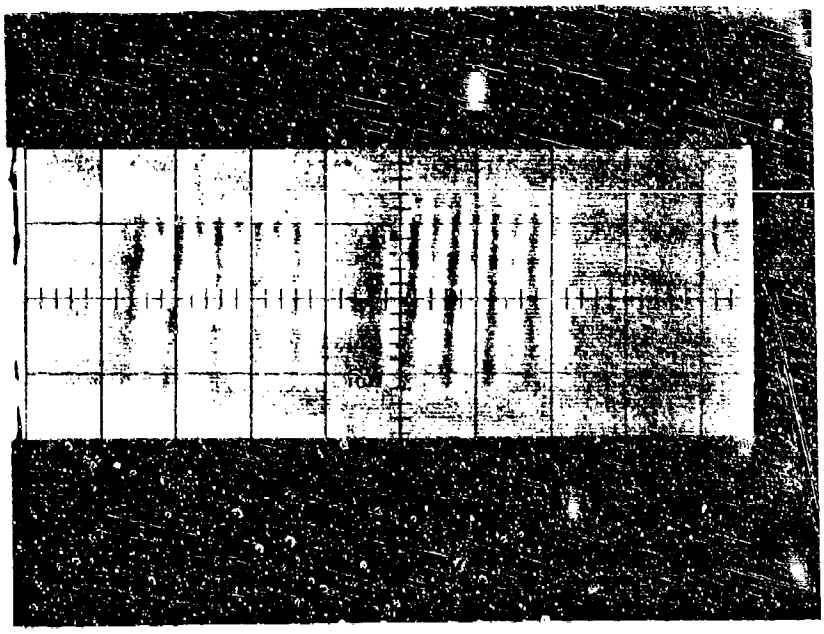

Figure 64. IR Scan of Test 319 in Video Mode

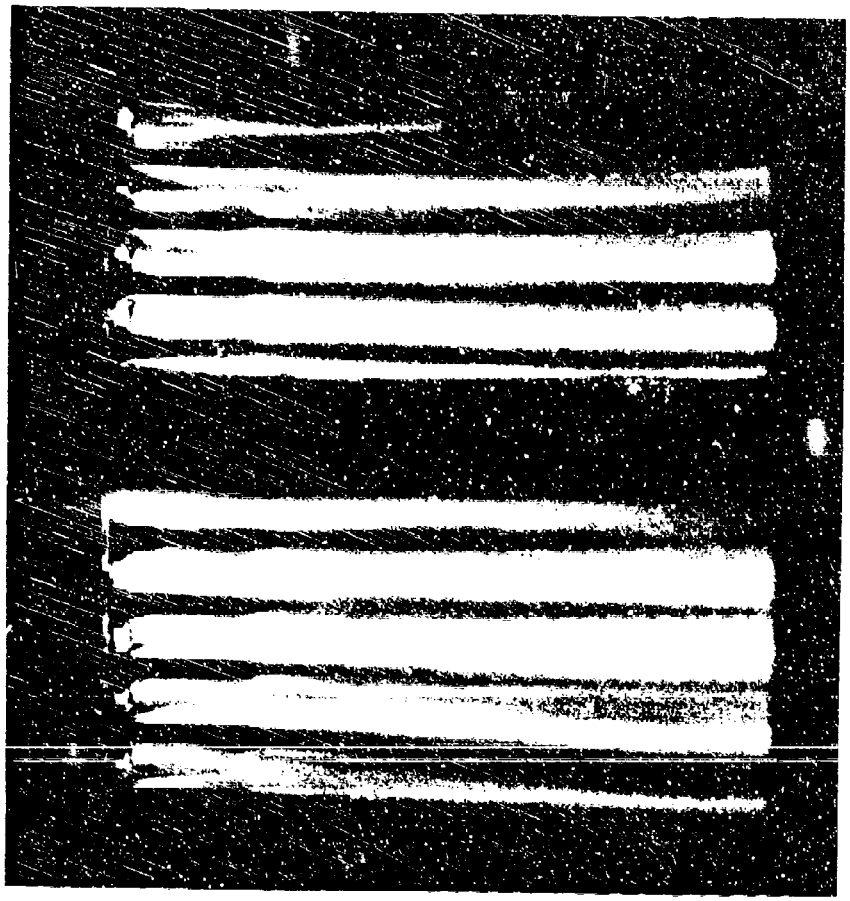

Figure 65. Visible Light Photo of Test 342

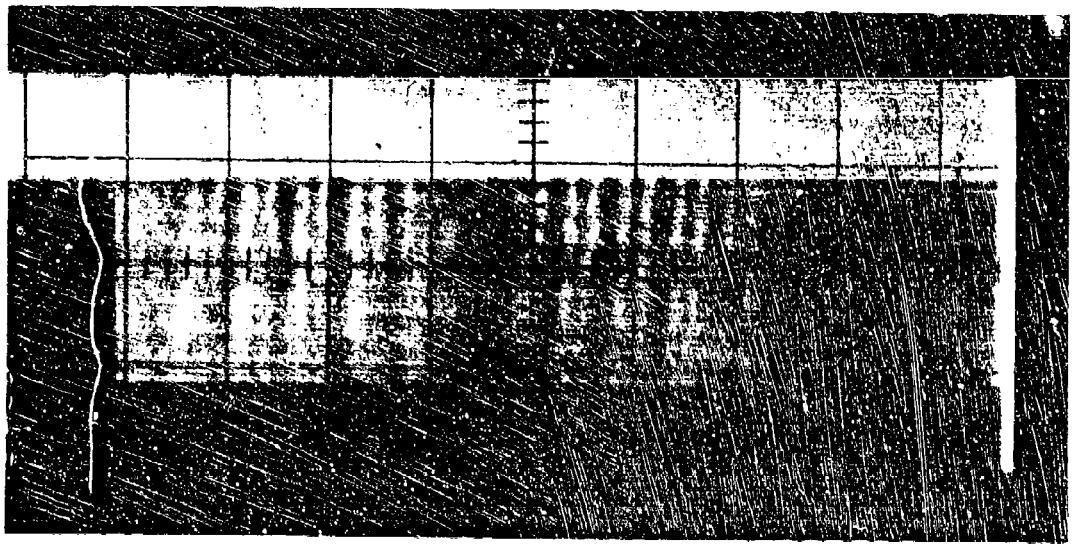

Figure 66. IR Scan of Test 321 in Video Mode

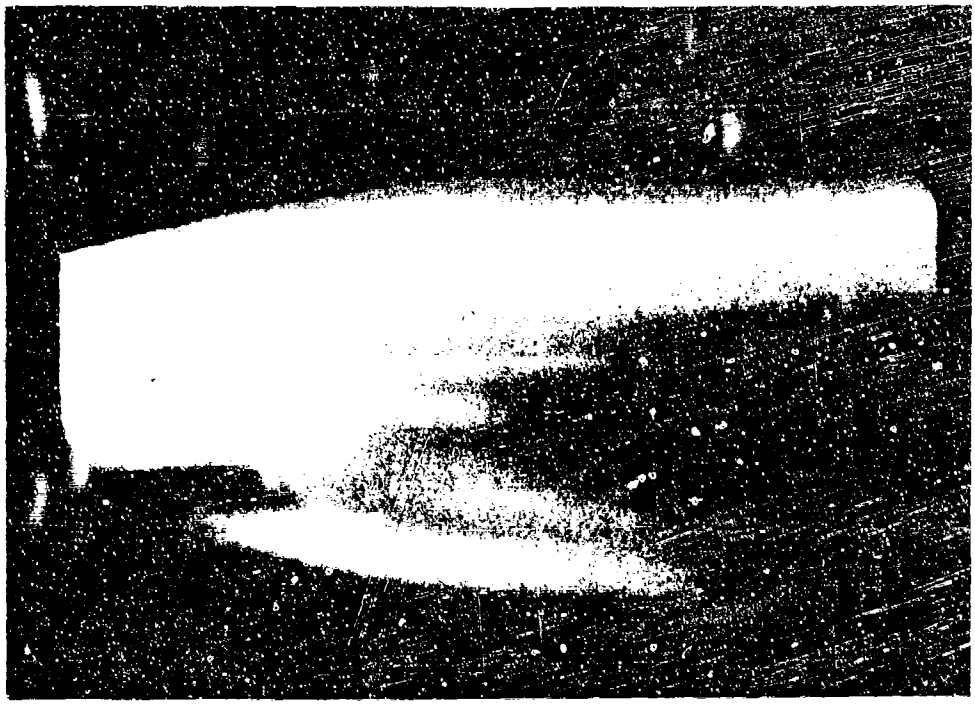

Figure 67. Visible Light Photo of Test 341, Side View

Figure 68. Visible Light Photo of Test 342, Side View

Several general statements can be made concerning the observed character of the flow field as follows:

(1) There is very little IR or visible radiation emission directly downstream of the hydrogen nozzles

(2) The intensity within the fluorine jets begins to rise almost immediately and to level out at the centerline approximately 2-1/2 inches downstream

(3) The velocity difference between the fluorine and hydrogen streams has little if any influence on the observed spread angle

The first observation is in general agreement with the characteristics of the CL II device. In particular the "flame" appears to grow into the fluorine flow, sometimes with the boundary between the orange region and the fluorine making sharp bends. It is believed that the sharp bends in both cases are caused by oblique shock waves. Second, dark streaks originating at the hydrogen nozzles persist for many centimeters downstream in both lasers.

The dark streaks are more difficult to explain. There are several hypotheses. The first is that the hydrogen temperature is so low that the pumping reaction $H_2 + F \rightarrow HF^* + H$ proceeds very slowly in the hydrogen side of the mixing zone, and furthermore that the ratio of the several V-T deactivation rates relative to the pumping rate is higher at the lower temperature on the hydrogen side. Both these effects reduce the excited state population on the hydrogen side of the zone. The deleterious effects of cold temperature are even more pronounced for the "hot" ($H + F_2 \rightarrow HF^* + F$) reactions which would explain the absence of the orange glow in the troughs.

In the CL II device, the hydrogen is not preheated and is thus necessarily cold after expansion from the free jet slit through which it is injected.

The hydrogen stream in the CL III test series exited at approximately 115°K. This results from the large expansion ratio (effective $A_{ex}/A_t = 24/1$) and the fact that the hydrogen combustor temperatures were established at approximately 1100°K. Higher operating temperatures up to 2000°K can be produced but were not included in the initial test series to avoid any possibility of HF/DF isotope exchange.

A further explanation of the reduced emissions from the H_2 jet results from the discovery of an erroneous calibration of a sonic flow control orifice in the F_2 feed line for the H_2 preheater. As a consequence of this calibration error, considerable ground state HF was produced in the H_2 combustor and introduced along with the diluent and preheated H_2.

The discharge of ground state HF from the hydrogen nozzles would have similar effects on the production of excited states as the low temperatures discussed above, i.e., on the hydrogen side of the mixing zone, where the concentration of HF is higher, the HF V-T deactivation rate would be higher and thus the HF* concentration lower. The deleterious effect of the ground state HF is, or course, reinforced by the low temperature of the hydrogen stream.

Next, it should be pointed out that the molar concentration of hydrogen was higher than that of the fluorine in all the test runs and that this condition caused the flame to burn towards the fluorine side. To see this, consider the simplest situation in which the two streams have equal velocity (Case 5 of Table VIII). In this case, the hydrogen concentration is approximately four times that of the flourine. Assume an approximation that the two reactants diffuse turbulently and therefore with equal diffusion coefficients, to a narrow reaction zone. As is indicated in Figure 69, the reaction zone is shifted towards the fluorine side by the requirement that the reactant fluxes and therefore the concentration gradients be equal. In turbulent flow, of course, the reaction zone is smeared out but the effect should still exist. In the absence of a reliable method for dealing with

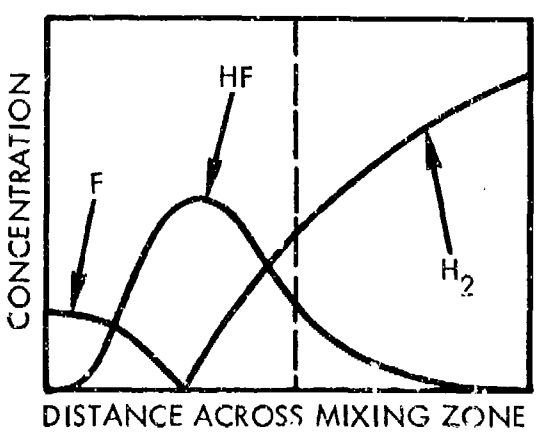

Figure 69
Concentration Profile Across Mixing Zone

reactions in turbulent flow, the above picture cannot be made quantitative but it seems unlikely that it fully explains the asymmetry in the reaction zone.

If we accept these explanations for the lack of emission from the hydrogen jet, then the angle of spread of the orange glow into the fluorine stream (observation 2) provides an indication of the gross mixing rate. There is considerable emission from the center of the fluorine stream at approximately 1 inch downstream and almost uniform emission 2-1/2 inches downstream. The estimates based on the subsonic mixing experiments, see Figure 31 (Section III. 3b (2) for example, predict that the edge of the mixing region reaches the nozzle conterline at approximately 1-1/2 inches from the nozzle exit.

Referring to Figures 59 through 62, the axial variation in intensities along the hydrogen and fluorine centerlines, the "valleys," are shown together with the intensity along the "ridge" between them. The data were taken from the flow field downstream of the third fluorine nozzle from the left hand side. The effects of parallax have not been removed from these data but it is useful, as it stands, in indicating several points. First, at distances greater than approximating 1 to 2 cm from the cavity injector exit there is little axial variation in the peak intensity, a result implying that the pumping reaction is not completed within the 14 cms scanned. Second, the radiation in the fluorine valley rises to a significant fraction of the peak intensity in 5 to 8 cm, a result consistant with considerable chemical reaction on the fluorine side of the mixing region. Finally, the much lower radiation from the hydrogen rich part of the field is evident.

The conclusion must be that the rate of gross turbulent mixing is approximately equal to that predicted in Section III. 3. b(2). The apparent failure for the pumping reaction to have been completed within the 14 cm length must presently be ascribed either to a failure to thoroughly mix on the microscale or to excessively slow kinetics as a result of the low nozzle exit temperatures. As was described previously, observation of a spread angle of approximately 0. 1 radian for the boundaries of gross turbulent mixing is not sufficient to describe adequate mixing for efficient lasing. The mechanism of microscale mixing within the turbulent zone is not well known and could be sufficiently slow to cause the observed extended reaction zone. The answer to these questions will be addressed by subsequent tests of the CL III with chemiluminescent spectroscopy diagnostic techniques.

There are two possible explanations for observation (3), the lack of influence on the spread angle caused by stream velocity differences. One is that the vortex generators so enhance the mixing that the velocity effect is overriden. The other possibility is suggested by the experiments in reference 17, i.e., combustion also can significantly increase the mixing rate between two supersonic streams and remove the velocity dependence. There is, at present, no basis for a choice between the two hypotheses and further testing is required to resolve the matter.

3. POWER MEASUREMENTS

The power tests (HB5-324 through -336) were conducted under similar conditions to those which were present in the previous diagnostic test series (HB5-308 through -323), so that the power output could be correlated with the diagnostic data. To preclude any HF/DF isotope exchange in the hydrogen preheater, all tests were performed at H_2 combustor temperatures less than 1100°K. Also, from a specific power standpoint, a minimum preheating of the H_2 just sufficient to obtain the required velocity difference was deemed advantageous. Unfortunately, the power in all cases was disappointingly low, less than 500 watts. Three fundamental causes have been identified and are discussed below.

a. Mixing Characteristics

As stated in the preceding section, the visible and IR radiation intensity within the fluorine jets began to rise almost immediately. The intensity then leveled out at the fluorine jet centerline approximately 2-1/2 inches downstream of the nozzle exit plane and remained nearly constant for at least another 3 inches downstream. The conclusion drawn from these data was that the gross rate of turbulent mixing within the fluorine jet was approximately equal to that predicted from previous subsonic experiments. However, micro-scale mixing within the turbulent zone is not well known and could be sufficiency slow to cause the observed extended reaction zone thus adversely affecting the lasing action.

b. Erroneous Calibration Data of Sonic Flow Control Orifice

In order that ground state HF not be formed in the H_2 preheater, it is necessary that the F_2/D_2 molar mixture ratio be equal to or less than one everywhere in the combustor (see Figure 70).

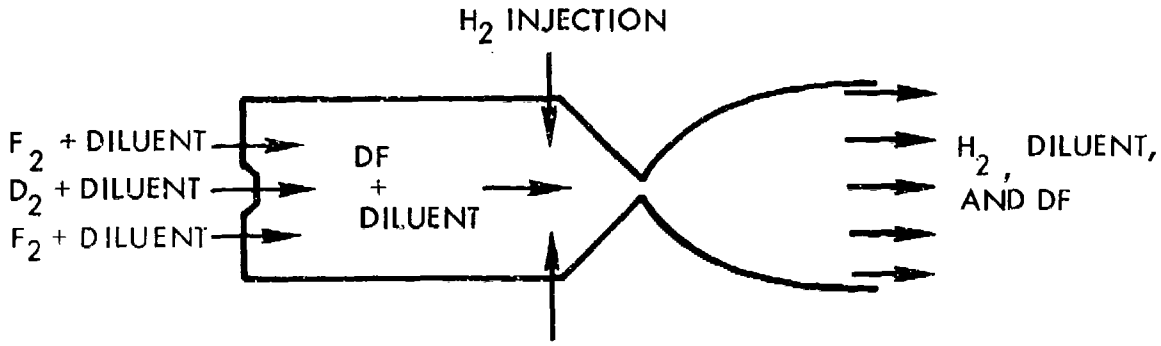

Figure 70. Typical H_2 Heater Nozzle Cross Section Schematic

Following completion of the test program, all sonic orifices were recalibrated. An error of five percent was found in the calibration of the F_2 sonic orifice leading to excessive F_2 flow into the H_2 heater combustor. This excess F_2 reacted with the H_2 injected downstream leading to the injection of relatively large quantities of ground state HF with the H_2 stream to the lasing cavity. This situation was further aggrevated by combustor injector flow maldistribution. Based upon empirical observation of the quantity of ground state HF introduced into the prior CL II device when operated in the HF/HF mode, and the calculated quantity introduced as a result of the CL III calibration problems, it is believed that sufficient ground state was injected to account for the low powers observed. Additional testing is required to confirm this hypothesis.

c. Low Nozzle Exit Temperatures

The relatively low hydrogen heater combustor temperatures of less than 1100°K led to very low H_2 temperatures at the nozzle exit, on the order of 115°K. This resulted in a laser cavity static temperature after mixing, but prior to the lasing reaction of only 150°K. Extrapolation of measured kinetics data (Ref. 21) taken at 350°K to the 150°K condition revealed that production to deactivation rates of HF* were unfavorable for lasing. As described in Section IV.2 this is believed to be one reason for

apparent lack of reaction in the center of the H_2 stream. Temperatures in the H_2 and F combustors must ultimately be increased to remedy this situation. Subsequent testing under the Technology Follow-On Program will involve increased combustor and consequently nozzle exit temperatures.

SECTION V

CONCLUSIONS

The conclusions of the investigations presented in this report may be grouped into two broad categories associated with the cavity diagnostics studies and chemical laser cavity injector development as follows.

- Cavity Diagnostic Evaluations

  The basic feasibility of Rayleigh/Raman scattering techniques to measure concentrations of molecular hydrogen and molecular fluorine in HF/DF laser cavities was established through analyses and laboratory experiments. By using a xenon UV laser and modifying existing scanner equipment, detection sensitivities on the order of 4×10^{-2} torr could be achieved for the above indicated species. However, helium appears not to be detectable with the current apparatus.

  Holographic interferometry appears to be a viable cavity diagnostic technique when employed on larger chemical laser devices where the optical path length is on the order of 1 meter. However, the method has marginal utility, i.e., it produces extremely small fractions of a fringe, when used in conjunction with current, smaller chemical laser systems unless modifications are made to existing interferometry devices and techniques to extend the state of the art. This is caused principally by the relatively short optical path length and very low density gases in the lasing region of the smaller laser devices.

- CL III Cavity Injector Development

  The testing of the CL III device during this program must, of course, be considered preliminary. The CL III design represents a new class of chemical laser cavity injectors that may be generically designated as high Reynolds number devices. As only limited testing was accomplished during the subject program, the substantiation of the high Reynolds number approach must await further evaluation testing. However, with the test results at hand the following preliminary observations can be made.

  (1) The CL III chemical laser is the first device capable of supplying a fully developed, preheated H_2 flow at high Reynold's number along with a similar parallel F flow to investigate the effects of hydrogen/fluorine velocity differences on turbulent mixing and lasing over a wide range of supersonic conditions.

(2) Analyses of the CL III cavity diagnostic data revealed that very little IR or visible radiation emission occurred directly downstream of the hydrogen nozzles in any of the runs observed. On the other hand, the intensity within the fluorine jets began to rise almost immediately and leveled out at the centerline approximately 2-1/2 inches downstream of the nozzle exit plane. The conclusion drawn from these data is that the rate of gross mixing within the fluorine jet was approximately equal to that predicted from subsonic experiments.

(3) The inability to derive closed cavity power greater than 500 watts can be attributed to three fundamental causes: first, sufficiently slow microscale mixing within the gross turbulent mixing regions to cause extended axial reaction zones thus adversely affecting the lasing action; second, the relatively low laser cavity static mixture temperature of approximately 150°K leading to adverse production-to-deactivation rates of HF* as predicted from extrapolated kinetics data; and third, excessive ground state HF injected into the laser cavity as a result of a miscalibrated fluorine orifice in the reactant feed system.

Further testing of the CL III device employing chemiluminescent spectroscopy is required to understand and correct the deficiencies observed in this initial test series.

REFERENCES

1. F. Mastrup, J. Broadwell, J. Miller and T. Jacobs, "Hydrogen Fluoride Laser Technology Study," AFWL TR-72-28, 3 February 1972.

2. S. Chandrasekhar, Radiative Transfer, Dover Publications, New York, New York, 1960.

3. F.A. Jenkins and H.E. White, Fundamentals of Optics, 3rd Edition, McGraw Hill New York, 1957.

4. S. Tolansky, An Introduction to Interferometry, Longmans, Green, London, 1955.

5. H.W. Liepmann and A. Roshko, Elements of Gas Dynamics, John Wiley and Sons, 1057.

6. S. Tolansky, Multiple Beam Interferometry of Surfaces and Films, Clarendon Press Oxford, 1949.

7. R.C. West and S.M. Selby, Editors, CRC, Handbook of Chemistry and Physics, 48th Edition, The Chemical Rubber Company, Cleveland, Ohio, 1968.

8. R.F. Wuerker, L.O. Heflinger and R.A. Briones, "Holographic Interferometry with Ultraviolet Light," Applied Physics Letters, 12., #9, May 19, 1968.

9. L.O. Heflinger and R.E. Brooks, "Holographic Instrumentation Studies, Contract NAS 2-4992, 12122-6007-R0-00, NASA Ames, Sept. 1970.

10. R.F. Wuerker, B.J. Matthews and R.A. Briones, "Producing Holograms of Reacting Sprays," JRL Contract 952023 (NASA 7-100), July 1968.

11. "EG Initial CO_2 Laser Holography," Lawrence Livermore Contract P.O. 7866109, May 1972.

12. Richard B. Fancher, "Low Area Ratio Thrust Augmenting Ejectors," Aerospace Research Laboratories.

13. Robert C. Johnson, "Real-Gas Effects in Critical Flow Through Nozzles and Tabulated Thermodynamic Properties, NASA TN D-2565.

14. "Chemical Laser System Study (U)," AFWL TR-71-174, 24 January 1972 (S).

15. G.N. Abramovich, The Theory of Turbulent Jets, The M.I.T. Press, Cambridge, Mass., 1963

16. Garry Brown and Anatol Roshko, "The Effect of Density Difference on the Turbulent Mixing Layer," Calif. Institute of Technology, Pasadena, private communication.

17. R. J. Sanderson and P. C. Steel, "Results of a Shock Tube Experiment in Compressible Turbulent Mixing." Proj. SQUID No. MAR-1-PU, March 1971.

18. J. B. Miles and J. Shih, "Similarity Parameter for Two-Stream Turbulent Jet-Mixing Region," AIAA J. 6 (1968).

19. B. W. Spencer and B. G. Jones, "Statistical Investigation of Pressure and Velocity Fields in the Turbulent Two-Stream Mixing Layer," AIAA Paper No. 71-613.

20. R. L. Baker and H. Weinstein, "Experimental Investigation of the Mixing of Two Parallel Streams of Dissimilar Fluids," NASA CR-957.

21. J. R. Airey and S. F. Fried, "Vibrational Relaxation of Hydrogen Fluoride," Chem. Phy. Letters, Vol. 8, 23, Jan. 1971. p 23

Table VIII. Boundary Layer and One-Dimensic
culation Results (150 psia combust

Potential Test Condition	Injector	Combustor Conditions							Nozzle Exit Flow Properties											
		$\dot{m}_{D_2}$ (gm/sec)	$\dot{m}_{F_2}$ (gm/sec)	$\dot{m}_{He}$ (gm/sec)	$\dot{m}_{N_2}$ (gm/sec)	$\dot{m}_{H_2}$ (gm/sec)	P_c (psia)	Temperature (°K)	$\bar{N}$ (gm/mole)	$\bar{V}$ Btu/Sec	(GM)	$\dot{\bar{V}}$ (GM)	$\frac{\bar{V}B}{R}$	$\frac{P_c}{\langle P_c \rangle}$	M_{ex}	(GM)	v_{ex} (ft/sec)	P_{ex} (psia)	T_{ex} (°K)
1	H_2	1.41	26.6	17.6	0	4.0	75	1000	4.89	1.537	.1565	.0624	.2262	2.206	5.84	4.[illegible]	[illegible]	.0098	98
	F	1.60	34.2	0	0	0	66	1700	19.89	1.481	.1127	.0775	.2556	2.208	5.52	4.64	6440	.0963	204
2	H_2	1.66	15.8	17.2	0	3.0	75	1300	5.68	1.542	.1575	.0632	.2546	2.238	5.37	5.01	10260	.09[illegible]	136
	F	1.60	34.2	0	0	0	66	1700	19.89	1.481	.1127	.0770	.2656	2.208	5.52	4.54	6440	.0963	204
3	H_2	1.60	15.2	10.4	0	1.2	75	1870	7.10	1.542	.1855	.0732	.3264	2.242	5.[illegible]	4.[illegible]	11[illegible]	[illegible]	181
	F	1.60	34.2	0	0	0	66	1700	19.89	1.481	.1127	.0770	.2856	2.208	5.52	4.54	[illegible]	[illegible]	204
4	H_2	1.60	15.2	10.4	0	1.2	75	1870	7.10	1.542	.1555	.0632	.3264	2.242	5.[illegible]	4.[illegible]	11[illegible]	.0973	181
	F	1.20	22.8	0	17.6	0	67	1300	22.75	1.444	.1535	.0541	.2[illegible]	1.[illegible]	5.[illegible]	4.[illegible]	[illegible]	[illegible]	23[illegible]
5	H_2	1.41	13.3	17.6	0	4.0	75	1300	4.[illegible]8	1.580	.1[illegible]26	.1010	.1[illegible]	2.[illegible]	[illegible]	5.15	34[illegible]	[illegible]	[illegible]
	F	1.82	26.8	6.8	0	0	75	2300	11.[illegible]	1.546	.1827	[illegible]	.3235	2.2[illegible]	5.42	5.26	[illegible]	.0945	16[illegible]
6	H_2	0	0	0	98.1	3.6	75	300	1[illegible].17	1.4[illegible]	.0715	.0442	.0767	1.4[illegible]	5.12	4.7[illegible]	25[illegible]	.1243	[illegible]
	F	1.92	37.2	4.2	0	0	75	1700	14.4[illegible]	1.526	.1[illegible]	.0838	.2[illegible]	2.08[illegible]	5.52	5.34	742	[illegible]	172
7	H_2	0.85	7.98	0	46.2	2.0	71	1100	18.[illegible]	1.[illegible]	.104	.04[illegible]	.184	1.[illegible]	4.[illegible]4		521[illegible]	.[illegible]	1[illegible]5
	F	1.67	16.0	6.0	0	0	73	1700	12.[illegible]	1.5	.144	[illegible]	.2[illegible]	[illegible]	[illegible]		[illegible]	.12	2[illegible]
8	H_2	1.52	14.4	17.2	0	3.0	78	1300	5.5[illegible]	1.52	.142	.075	.225	1.[illegible]	5.[illegible]		[illegible]	.1[illegible]	115
	F	1.40	15.2	0	22.4	0	75	1[illegible]	2[illegible]	1.[illegible]	.114	[illegible]	.252	1.5[illegible]	4.[illegible]		5[illegible]	.1[illegible]	[illegible]
9	H_2	0	0	0	98.1	3.6	75	300	1[illegible].[illegible]	1.[illegible]	.047	.042	.1[illegible]	1.51	4.[illegible]		[illegible]	.155	[illegible]
	F	1.66	34	6.6	0	0	75	1700	12.[illegible]	1.4[illegible]	.147	.0[illegible]5	.27[illegible]	1.[illegible]	5.37		8[illegible]0	.124	222
10	H_2	1.52	14.4	17.2	0	3.0	75	1300	5.5[illegible]	1.52	.142	.07[illegible]	.2[illegible]5	1.[illegible]	5.[illegible]		[illegible]	.110	115
	F	1.66	34.8	6.0	0	0	75	1700	12.[illegible]	1.5[illegible]	.144	.0[illegible]	.2[illegible]1	1.67	5.[illegible]		82[illegible]	.12[illegible]	233

er and One-Dimensional Mixing Cal-
ts (150 psia combustor pressure)

r Properties								Mix Properties Without Heat Addition								Mix Properties With Heat Addition							
M_x	V_{ex} (ft/sec)	P_{ex} (psia)	T_{ex} (°K)	Velocity Ratio $\frac{V_{ex}(H_2)}{V_{ex}(H_2)}$	(T_{ex}) (°K)	(V_{ex}) (ft/Sec)	A (cm²)	$\bar{N}_m$ (gm/mole)	$\bar{\gamma}_m$	M_m	V_m (ft/Sec)	T_m (°K)	T_{om} (°K)	P_{om} (psia)	A_m CM²	$\bar{N}_m$ (gm/mole)	$\bar{\gamma}_m$	M_m	V_m (ft/Sec)	T_m (°K)	T_{om} (°K)	P_{om} (psia)	A_m (cm²)
.97	9720	.0988	98	0.66	126.1	9450	38.1	7.95	1.531	4.84	7790	150.6	1086	2[illegible].91	69.4	7.954	1.531	2.102	7790	797	1732	0.0910	367
.84	6440	.0963	204		247.0	6195	29.3																
.01	10260	.0973	126	0.63	161.2	9915	44.0	8.71	1.534	4.52	8100	203.5	1316	20.6	86.4	8.711	1.534	2.174	8100	881	1994	1.911	374
.84	6440	.0963	204		247.0	6195	29.3																
.98	11010	.0973	181	0.58	230.6	10550	35.7	10.07	1.527	4.09	8060	320.1	1733	12.85	93.4	10.07	1.527	2.401	8060	913	2299	1.410	268
.84	6440	.0963	204		247.0	6195	29.3																
.98	11010	.0973	181	0.57	230.6	10550	35.7	12.01	1.512	4.01	7890	344.5	1761	12.00	103.8	12.01	1.512	2.457	7890	916	2333	1.532	276
.70	6300	.1069	248		283.3	6075	34.8																
.15	9460	.0897	84	0.95	115.6	9185	33.9	7.03	1.572	5.37	8880	136.8	1165	43.82	61.0	7.035	1.572	2.980	8880	444	1573	3.13	198
.05	8980	.0943	189		241.0	8600	35.5																
.79	2670	.1240	48	2.58	49.9	2855	37.6	17.46	1.444	3.70	4140	161.1	675	10.26	131.8	17.46	1.444	1.736	4140	769	1283	0.513	629
.04	7420	.0971	172		215.1	7155	36.4																
	5210	.156	185	1.59																			
	8270	.123	203																				
	9630	.116	115	0.50																			
	5[illegible]00	.197	359																				
	5110	.155	70	2.61																			
	6330	.124	222																				
	9630	.116	115	0.36																			
	8270	.123	203																				

NOT CALCULATED

Table IX. Boundary Layer and One-Dim
Calculation Results (75 psia c

Test Condition No.	Injector	Combustor Conditions							Nozzle Exit Pr						
		$\dot{m}_{D_2}$ (gm/sec)	$\dot{m}_{F_2}$ (gm/sec)	$\dot{m}_{He}$ (gm/sec)	$\dot{m}_{N_2}$ (gm/sec)	$\dot{m}_{H_2}$ (gm/sec)	P_c (psia)	Temperature °K	δ (cm)	δ^* (cm)	$\frac{MB}{\dot{m}}$	$\frac{P_c}{P_c^*}$	M_{ex}	<M>	V_{ex} (ft/sec)
1	H_2	2.82	53.2	35.2	0	8.0	150	1000	0.1147	0.0685	0.1571	1.785	5.92	5.28	9735
	F	3.20	68.4	0	0	0	132	1700	0.1176	0.0559	0.2016	1.682	5.57	5.05	6450
2	H_2	3.32	31.6	34.4	0	6.0	150	1300	0.1227	0.0687	0.1841	1.803	5.95	5.30	10280
	F	3.20	68.4	0	0	0	132	1700	0.1176	0.0559	0.2016	1.682	5.57	5.05	6450
3	H_2	3.20	30.4	20.8	0	2.4	150	1870	0.1354	0.0687	0.2274	1.834	5.95	5.29	11025
	F	3.20	68.4	0	0	0	132	1700	0.1176	0.0559	0.2016	1.682	5.57	5.05	6450
4	H_2	3.20	30.4	20.8	0	2.4	150	1870	0.1354	0.0687	0.2274	1.834	5.95	5.29	11025
	F	2.40	45.6	0	35.2	0	134	1800	0.1140	0.0499	0.2054	1.625	5.34	4.89	6310
5	H_2	2.82	26.6	35.2	0	8.0	150	1000	0.120	0.0749	0.1571	1.848	6.22	5.49	9485
	F	3.64	53.6	13.6	0	0	150	2000	0.1332	0.0669	0.2274	1.302	6.00	5.34	8990
6	H_2	0	0	0	196.2	7.2	150	300	0.0572	0.0314	0.0780	1.323	5.12	4.88	2870
	F	3.84	74.4	8.4	0	0	150	1700	0.1197	0.0611	0.1947	1.722	5.87	5.29	7435
	H_2														
	F														
	H_2														
	F														
	H_2														
	F														
	H_2														
	F														

Layer and One-Dimensional Mixing
n Results (75 psia combustion pressure)

Nozzle Exit Properties										Mix Properties Without Heat Addition							
[illegible]	M_{ex}	$\langle M \rangle$	V_{ex} (ft/sec)	P_{ex} (psia)	T_{ex} (°K)	$\frac{V_{ex}(F)}{V_{ex}(H_2)}$	$\langle T_{ax} \rangle$ °K	$\langle V_{ex} \rangle$ (ft/sec)	A (cm^2)	$\bar{N}_n$ (gm/mol)	$\bar{Y}_n$	M_m	V_m (ft/sec)	T_m (°K)	T_{om} (°K)	P_{om} (psia)	A_m (cm^2)
1. [illegible]	5.92	5.28	9735	0.184	96.1	0.66	113.7	9350	34.7			5.16	7775	131.8	1063	79.93	60.9
1. [illegible]2	5.57	5.05	6450	0.184	201.0		235.7	6275	27.6								
1. [illegible]03	5.35	5.30	10280	0.181	122.5	0.63	150.8	10015	40.7			4.71	8185	191.2	1327	50.48	80.4
1. [illegible]2	5.57	5.05	6450	0.184	201.3		235.7	6275	27.6								
1. [illegible]4	5.95	5.29	11025	0.181	176.2	0.58	216.0	10685	33.0			4.22	8225	307.2	1752	30.1	88.4
1. [illegible]2	5.57	5.05	6450	0.184	201.0		235.7	6275	27.6								
1. [illegible]4	5.95	5.29	11025	0.181	176.2	0.58	216.0	10685	33.0			4.13	7985	331.2	1781	27.9	98.7
1. [illegible]2	5.34	4.89	6310	0.207	245.8		272.2	6150	33.1								
1. [illegible]43	6.22	5.49	9485	0.165	81.9	0.95	107.3	9275	31.2			5.67	9000	125.7	1284	115.1	55.3
1. [illegible]02	6.00	5.34	8990	0.177	184.8		227.5	8720	33.1								
1. [illegible]	5.12	4.88	2870	0.247	47.9	2.59	48.4	2865	36.5			3.83	4160	159.5	678	21.5	75.5
1. [illegible]	5.87	5.29	7435	0.184	168.7		201.4	7220	34.1								

2

Table XII. Summary of CL III Test

Test No.	Test Date	Test Duration (sec)	Combustor	COMBUSTOR CONDITIONS $\dot{n}_{D_F}$ (mo/sec)	$\dot{n}_{F_2}$ (mo/sec)	$\dot{n}_F$ (mo/sec)	$\dot{n}_{He}$ (mo/sec)	$\dot{n}_{N_2}$ (mo/sec)	$\dot{n}_{H_2}$ (mo/sec)	Total Molar Flow Rate (mo/sec)	P_c (psia)	T_c (°K)	α Dissociation Fraction	ψ Diluent Ratio	Rc Mixture Ratio	Heat Loss: Combustor Loss (Btu/sec)	Heat Loss: Cavity Injector Loss (Btu/sec)	SUPPLY CO $\dot{m}_{D_2}$ (gm/sec)	$\dot{m}_{F_2}$ (gm/sec)	$\dot{m}_{He}$ (gm/sec)
EBS:																				
308	2-24-72	70	H_2	0.444	-	-	3.52	-	1.500	5.456	57.3	790	-	-	1.045	17.1	36.7	0.895	8.82	14.08
			F_2	(Test run with H_2 combustor only)						-										
309		66	H_2	(Test run with F_2 combustor only)				-		-										
			F_2	0.596	0.030	0.640	-	-	-	1.266	50.4	1695	0.913	1.703	2.199	18.8	40.7	1.187	24.62	-
310	2-24-72	18	H_2	0.437	-	-	3.39	-	1.50	5.330	55.8	790	-	10.572	1.044	14.9	39.7	0.881	8.32	13.58
			F_2	0.598	0.010	0.704	-	-	-	0.680	53.4	1900	0.971	1.651	2.212	13.0	37.4	1.204	25.12	-
314	3-1-72	42	H_2	0.424			3.551		2.011	6.081	66.0	745		12.18	1.055	18.5	55.7	1.056	10.51	14.22
			F_2	0.606	0.042	0.585				1.233	51.4	1630	0.873	1.812	2.104	19.5	52.4	1.221	24.24	-
315		53	H_2	0.530			3.358		1.977	5.865	63.4	770		10.983	1.018	17.8	56.4	1.068	10.25	13.44
			F_2	0.599	0.066	0.576				1.241	51.8	1570	0.814	1.692	2.182	19.2	53.1	1.206	24.83	-
316		47	H_2	0.551			3.348		1.972	5.871	63.0	770		-	0.978	16.7	61.7	1.109	10.23	13.40
			F_2	-	-					-	-	-	-	-	-	-	-	-	-	-
317		32	H_2	0.551			3.373		.969	5.893	63.1	820		21.21	0.974	17.2	54.8	1.110	10.20	13.50
			F_2	0.664	0.019	0.332	1.288			2.243	66.4	1545	0.899	10.551	1.551	32.2	51.6	1.348	19.73	5.15
318	3-1-72	44	H_2	-			-		-	-	-	-		-	-	-	-	-	-	-
			F_2	0.668	0.025	0.317	1.277			2.287	66.4	1500	0.863	10.599	1.550	31.1	54.8	1.345	19.67	5.11
319	3-6-72	35	H_2	0.722			4.218		1.509	6.449	85.2	1105		19.526	1.096	21.5	46.7	1.454	15.03	16.88
			F_2	0.702	0.021	0.364		0.823		2.010	89.4	1670	0.916	6.028	1.721	26.7	43.9	1.414	22.96	-
320		72	H_2	0.772			4.256		1.527	6.551	85.4	1120		20.315	1.025	22.5	55.4	1.556	15.03	17.04
			F_2	0.704	0.035	0.425		0.827		1.991	91.3	1585	0.859	6.186	1.704	27.1	52.1	1.413	22.79	-
321		80	H_2	0.435			-	1.678	0.985	3.098	74.2	930		8.486	0.998	10.6	46.4	0.876	8.24	-
			F_2	0.835	0.005	0.488	1.515			2.843	88.9	1845	0.979	9.438	1.598	36.1	43.7	1.681	25.34	6.06
322		42	H_2	-			-	3.95	1.780	5.730	75.3	-		18.036		-	-	-	-	
			F_2	0.752	0.020	0.398	1.328			2.498	78.9	1590	0.907	9.498	1.584	33.6	57.5	1.514	22.62	5.31
323	3-6-72	39	H_2	0.759			4.29		1.49	6.539	85.5	1040		20.318	1.055	22.7	63.7	1.529	15.21	17.16
			F_2	0.895	0.020	0.457	1.520			2.832	88.1	1625	0.919	9.477	1.595	36.8	59.9	1.681	25.30	6.08
324	3-8-72	44	H_2	0.783			4.25		1.484	6.517	85.7	1125		21.103	1.017	22.7	57.0	1.576	15.13	17.01
			F_2	0.717	0.026	0.425		0.813		1.981	93.1	1625	0.890	6.415	1.666	27.1	53.7	1.444	22.70	-
325		55	H_2	0.192			1.02		0.360	1.572	18.2	785		15.439	1.009	8.5	24.0	0.386	3.67	4.08
			F_2	0.198	0.046	0.065		0.201		0.510	23.4	1200	0.412	5.083	1.796	10.9	22.6	0.498	6.74	-
326		55	H_2	-			6.00		1.22	7.220	39.7	-		42.705	-	-	-	-	-	23.96
			F_2	0.344	0.061	0.159		0.408		0.972	44.1	1320	0.566	5.352	1.817	16.7	31.9	0.603	11.88	-
327		120	H_2	0.208			1.104		0.357	1.669	18.9	845		14.623	0.932	9.0	24.2	0.418	3.68	4.42
			F_2	0.200	0.048	0.095		0.211		0.514	24.4	1175	0.361	5.444	1.758	12.1	22.8	0.402	6.67	-
328		120	H_2	0.197			0.996		0.354	1.547	18.1	825		15.595	0.987	8.5	24.8	0.397	3.70	3.98
			F_2	0.196	0.049	0.055		0.200		0.500	23.7	1175	0.360	5.176	1.782	11.5	22.9	0.395	6.64	-
329		103	H_2	0.785			4.385		1.488	6.658	86.5	1125		20.314	1.919	22.7	55.7	1.58	15.19	17.55
			F_2	0.694	0.046	0.417		0.924		1.981	93.2	1550	0.820	5.965	1.732	27.5	52.5	1.398	22.85	-
330		43	H_2	-			-	3.24	1.60	4.840	62.6	-		13.996		-	-	-	-	-
			F_2	0.746	0.032	0.399	1.346			2.523	80.2	1535	0.861	9.037	1.622	33.8	52.5	1.502	22.96	5.39
331	3-8-72	54	H_2	0.436				1.608	0.978	3.022	72.1	915		8.394	0.997	10.9	49.4	0.879	8.27	-
			F_2	0.837	0.006	0.475	1.517			2.835	89.9	1815	0.975	9.667	1.582	36.9	46.5	1.686	25.16	6.07
332	3-14-72	68	H_2	0.255			0.993		0.354	1.602	20.9	1065		16.103	1.008	10.0	28.9	0.514	4.89	3.74
			F_2	0.251	0.019	0.117		0.207		0.594	28.8	1375	0.753	5.910	1.619	11.5	27.2	0.505	7.71	-
333		120	H_2	0.256			0.940		0.354	1.550	21.0	1065		15.432	1.010	10.5	28.4	0.515	4.91	3.76
			F_2	0.252	0.019	0.117		0.208		0.596	28.9	1375	0.753	5.935	1.614	12.1	26.8	0.508	7.73	-
334		53	H_2	0.531			2.000		0.733	3.264	45.5	1370		34.435	0.945	16.6	37.3	1.069	9.53	8.02
			F_2	0.256	0.042	0.063		0.216		0.577	29.4	1210	0.428	6.422	1.575	11.6	35.2	0.515	7.65	-
335		41	H_2	0.544			2.00		0.734	3.278	45.6	1335		19.875	0.927	16.7	42.4	1.095	9.57	8.00
			F_2	0.490	0.002	0.252		0.411		1.155	56.7	1830	0.981	7.039	1.523	18.5	39.9	0.987	14.18	-
336	3-14-72	48	H_2	0.846			4.19		0.730	5.766	81.7	1370		44.175	0.937	22.4	55.5	1.70	15.07	16.76
			F_2	0.650	0.000	0.228		0.411		1.289	65.3	2390	0.999	9.307	1.351	20.1	52.2	1.31	16.68	-
339	3-15-72		H_2	0.243			1.027		0.359	1.629	21.6	1005		16.076	1.042	9.1	27.9	0.494	4.85	4.11
			F_2	0.249	0.016	0.126	-	0.208		0.599	28.0	1405	0.800	5.785	1.632	10.7	26.3	0.502	7.73	-
340			H_2	0.149				0.410	0.236	0.795	20.5	750		6.988	1.107	4.7	23.8	0.300	3.13	
			F_2	0.249	0.012	0.136	0.366			0.763	23.8	1410	0.830	7.688	1.640	12.5	22.4	0.502	7.77	1.47
341			H_2	0.768			5.31		1.49	6.568	85.3	1125		21.336	1.029	22.3	52.8	1.547	15.02	17.27
			F_2	0.710	0.021	0.434		0.826		1.991	93.4	1660	0.912	6.454	1.671	26.3	49.8	1.430	22.54	
342			H_2	0.425				1.660	0.986	3.071	74.4	950		7.342	1.033	10.0	43.1	0.856	8.33	
	3-15-72		F_2	0.830	0.003	0.482	1.499			2.814	89.1	1925	0.986	8.201	1.588	34.0	40.6	1.672	25.05	6.00

CL III Test Results

SUPPLY CONDITIONS						NOZZLE CONDITIONS					CAVITY CONDITIONS						REMARKS
$\dot{m}_{O_2}$ (gm/sec)	$\dot{m}_{H_2}$ (gm/sec)	$\dot{m}_{He}$ (gm/sec)	$\dot{m}_{N_2}$ (gm/sec)	$\dot{m}_{H_2}$ (gm/sec)	Total Weight Flow Rate (gm/sec)	Pex Exit Pressure (psia)	Tex Exit Temperature (°K)	Vex Exit Velocity (ft/sec)	Velocity Ratio $V_{ex}(H)/V_{ex}(H_2)$	Heat Loss (Btu/sec)	P_L (torr)	M Diluent Ratio	Shroud Pressures Upper (torr)	Shroud Pressures Lower (torr)	GN2 Mirror Purge (gm/sec)	R_L (moles)	
195	5.82	14.08	-	3.022	26.82	-	-	-	-	2.2	-	-	-	-	-	-	Reduced field orange glow photos from bottom; IR. scan checkout from top. Heat loss tests at 75% of rated flow rates with one steam ejector.
												1.703				-	
187	24.62	-	-	-	25.81					2.2							
181	5.52	13.58	-	3.022	25.79					0.9		12.222				4.140	
204	25.12	-	-	-	26.33					0.9							
156	10.51	14.22	-	4.05	29.94	0.092	81.5	8531	0.697	1.4	6.25	13.99			8.0	6.012	Reduced field orange grow photos from bottom; I.R. scan checkout from top; 75% of rated flow rates with one steam ejector. 20% outcoupled flat mirror and Y_c scan.
221	24.74	-	-		25.46	0.087	211	5945		1.4							
188	10.25	15.41	-	3.98	28.75					1.4	6.25	12.67			8.0	5.585	
200	24.53	-	-		26.04					1.4							
109	10.27	13.40	-	3.97	28.71					0.1	3.72				8.0	-	
-	-	-	-		-												
110	10.20	13.50	-	3.97	28.78	0.089	83	8609	0.908	1.4	5.67	31.762			8.0	10.643	
248	19.73	5.15			26.23	0.086	147	7819		1.4							
-	-	-	-	-	-					-	2.33	10.599			8.0	-	
245	19.67	5.11	-		26.13					0.7							
154	15.0	16.35	-	3.04	36.41	0.116	115	9633	0.592	2.4	6.46	25.55			8.0	5.964	100% rated flow rates with 2 steam ejector. Reduced field orange glow photos from bottom and I.R. scan from top. Y_c scan with 20% outcoupled flat mirror.
314	22.96	-	23.06		47.43	0.197	339	5699		2.4							
154	15.03	17.04	-	3.07	36.69	0.116	115	9633	0.592	2.5	77.91	26.501			16.0	6.154	
318	22.79	-	23.17		47.38	0.197	339	5699		2.5							
176	8.24	-	47.00	1.98	58.10	0.156	185	5207	1.588	2.2	6.83	17.924			16.0	3.956	
181	25.34	6.06	-		33.09	0.123	203	8271		2.2							
-	-		113.89	3.59	114.48	0.155	70	3114	2.612	-	10.34	27.534			16.0	8.128	
314	22.62	5.31	-		29.45	0.124	222	8133		3.0							
329	15.21	17.16	-	3.00	36.90	0.116	115	9633	0.592	2.9	7.50	27.715			16.0	5.996	
181	25.30	6.08	-		33.06	0.123	203	8271		2.9							
176	15.17	17.01	-	2.99	36.70	0.116	115	9633	0.592	2.6	7.70	27.517	502	4.03	16.0	6.222	Plume shrouds set at 20°. 5% outcoupled flat mirror with purge ducts added to both mirrors. Reduced colorimeter water flow rate by 50% and increased water at sensitivity for tests HBS-327 and subsequent.
344	22.70	-	22.78		46.93	0.197	339	5699		2.6							
186	3.67	4.05	-	0.73	8.86	0.035	85	7802	1.111	1.1	3.10	20.522	3.83	2.95	16.0	4.586	
398	6.74	-	5.64		12.78	0.123	203	8671		1.1							
-	-	23.96	-	2.45	25.91	0.053	30	6496	0.819	-	7.70	48.057	6.93	5.58	16.0	8.683	
593	11.88	-	11.43		24.01	0.103	298	5318		1.6							
312	7.68	4.42	-	0.72	9.23	0.035	85	7802	0.648	1.1	3.21	20.067	4.24	3.62	16.0	4.728	
602	6.67	-	5.60		12.98	0.060	273	5059		1.1							
397	3.70	3.98	-	0.71	8.79	0.035	85	7802	0.648	1.1	2.07	20.771	2.07	1.55	4.0	4.527	
395	6.64	-	5.60		12.63	0.060	273	5059		1.1							
58	15.19	17.[illegible]	-	3.00	37.32	0.166	115	9633	0.592	2.6	6.00	26.279	3.57	2.43	4.0	5.847	
398	22.85	-	23.09		47.34	0.197	339	5699		2.6							
-	-	-	99.54	3.20	99.74	0.134	71	3130	2.598	-	8.79	24.033	5.95	-	4.0	7.442	
302	22.96	5.39	-		28.47	0.124	222	8133		4.3							
379	8.27	-	43.04	1.97	56.17	0.156	185	5207	1.579	2.4	4.76	18.061	3.05	-	4.0	4.016	
206	25.16	6.97	-		32.92	0.123	203	8221		2.4							
314	4.89	3.74	-	0.71	9.85					1.3	1.81	22.013	0.93	-	4.0	4.568	Closed cavity power tests with plume shrouds set at 20°. Orange glow photos from top through port in upper plume shroud 4 inches downstream of nozzle exit.
505	7.71	-	5.81		14.02					1.3							
315	4.91	3.76	-	0.71	9.90					1.4	1.81	21.367	0.83	-	4.0	4.568	
508	7.73	-	5.83		14.07					1.4							
969	9.53	8.02	-	1.48	20.10					1.6	2.58	40.857	0.98	-		9.973	
515	7.65	-	6.06		14.23					1.6							
995	9.57	8.00	-	1.48	20.15					2.0	3.10	26.914	0.98	-	4.0	5.734	
987	14.18	-	11.51		26.68					2.0							
70	15.07	16.7[illegible]	-	3.47	35.00					2.4	4.39	53.482	1.81	-	4.0	6.404	
31	16.[illegible]	-	11.50		26.50					2.4							
494	4.85	4.11		0.724	10.18					1.1	1.76	21.861	0.21	-	4.0	4.544	Full field orange glow photographs top and side.
502	7.73	-	5.83		14.06					1.1							
300	3.13		11.47	0.476	15.38					0.9	1.39	14.676	0.15[illegible]	-	4.0	3.250	
302	7.77	1.4[illegible]			9.74					0.9							
347	15.02	17.25		3.01	36.84	0.116	115	9633	0.592	2.3	6.53	27.790	1.81	-	4.0	6.261	
336	22.54		24.15		47.12	0.197	339	5699		2.3							
344	8.35		46.50	1.99	57.08	0.156	185	5207	1.588	1.9	4.39	15.543	1.50	-	4.0	3.472	
372	25.05	6.00			32.73	0.123	203	8271		1.9							

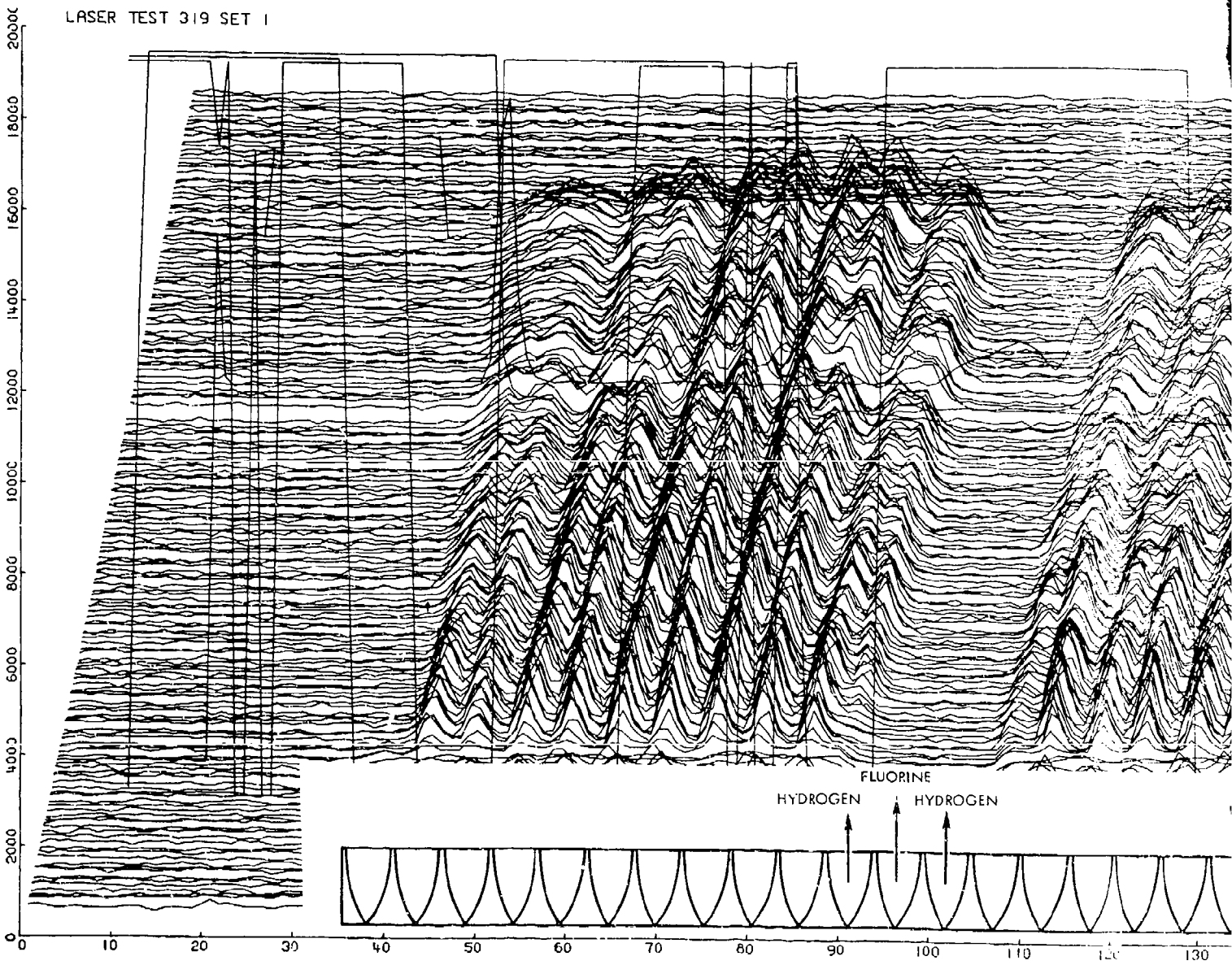

Figure 38. IR Intensity Distribution—

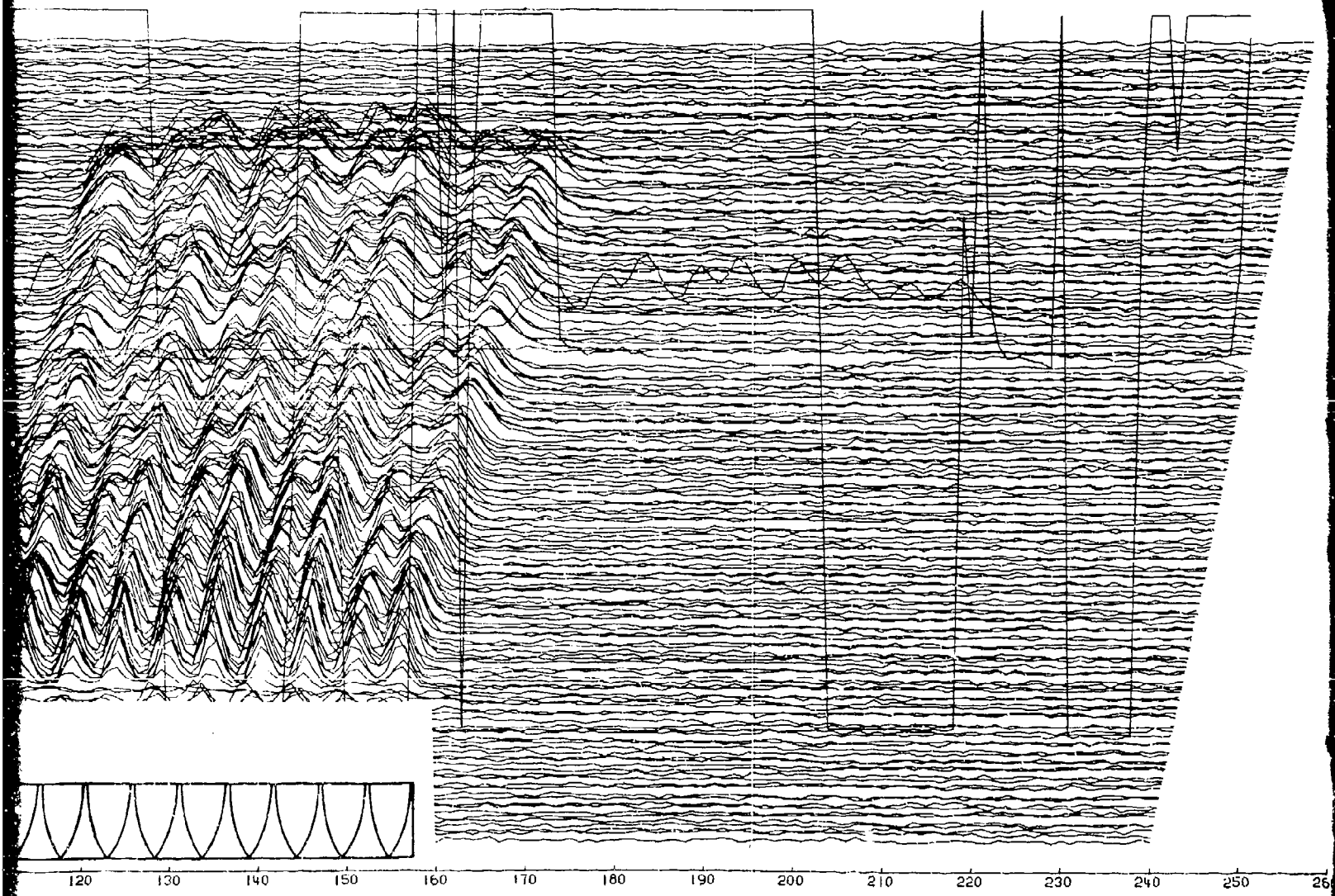

nsity Distribution — Test 319, Set I

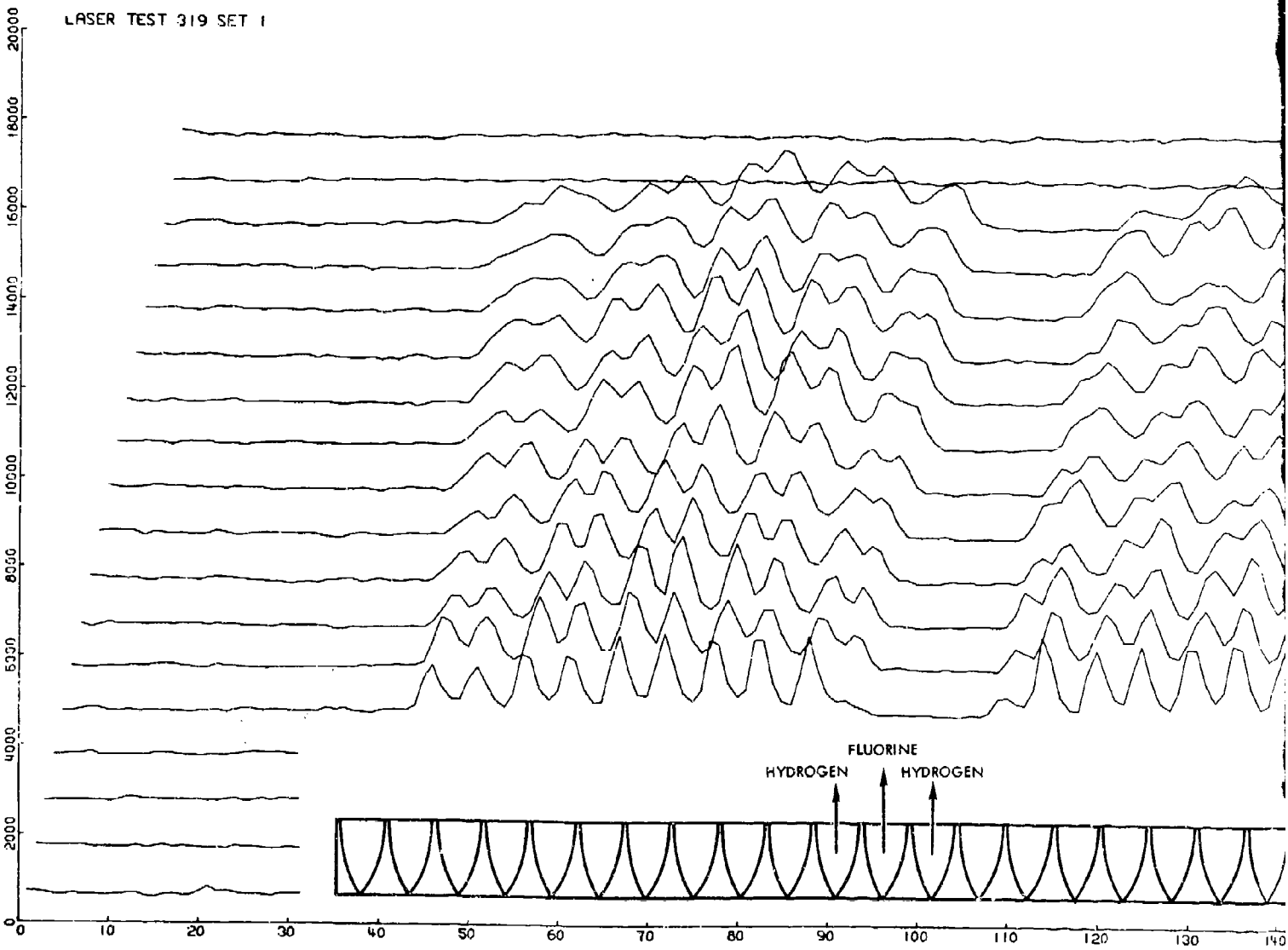

Figure 39. IR Intensity Distribution—Test 319. Set 1

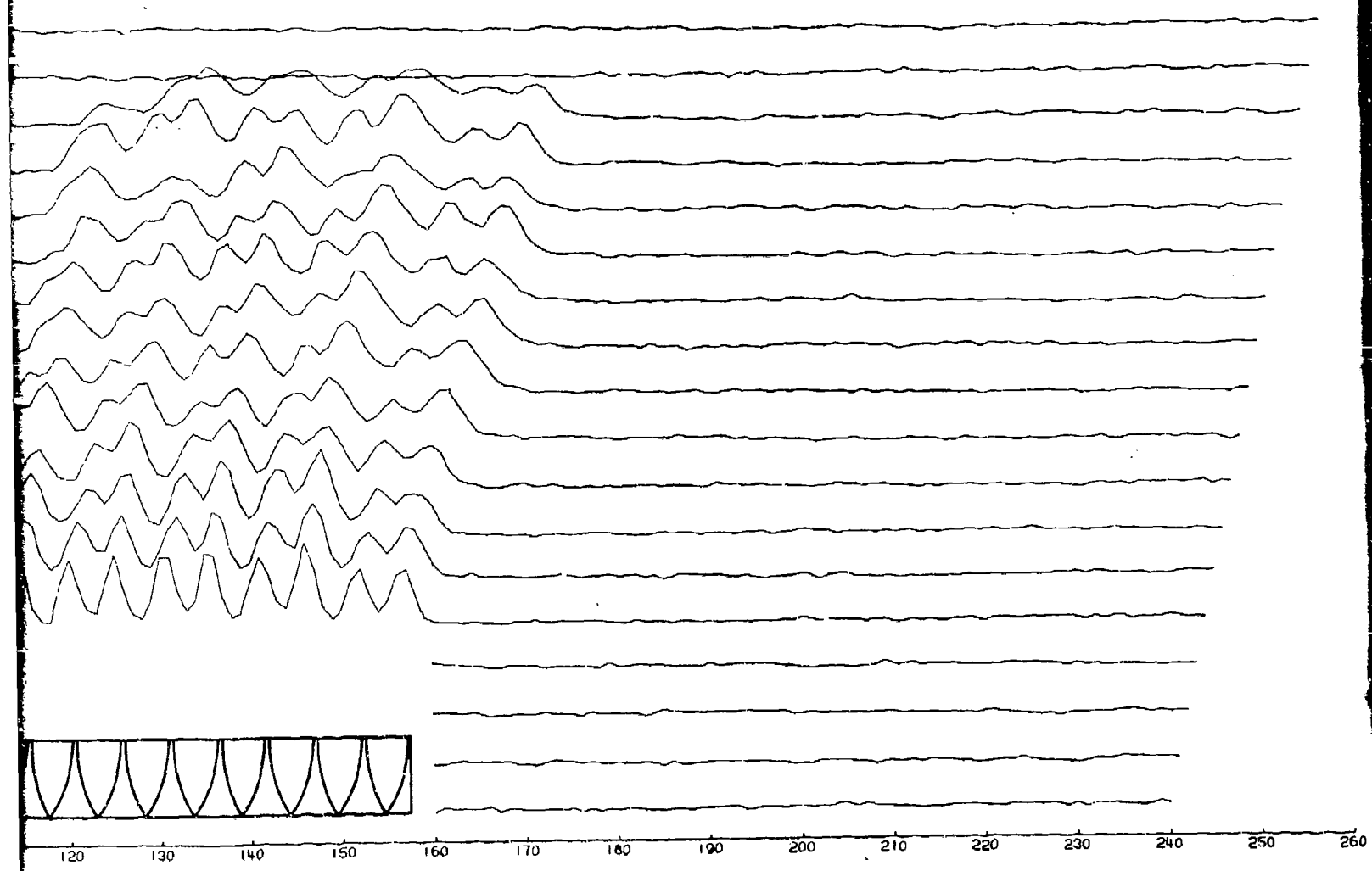

tion — Test 319. Set 1 (every 10th scan line)

2

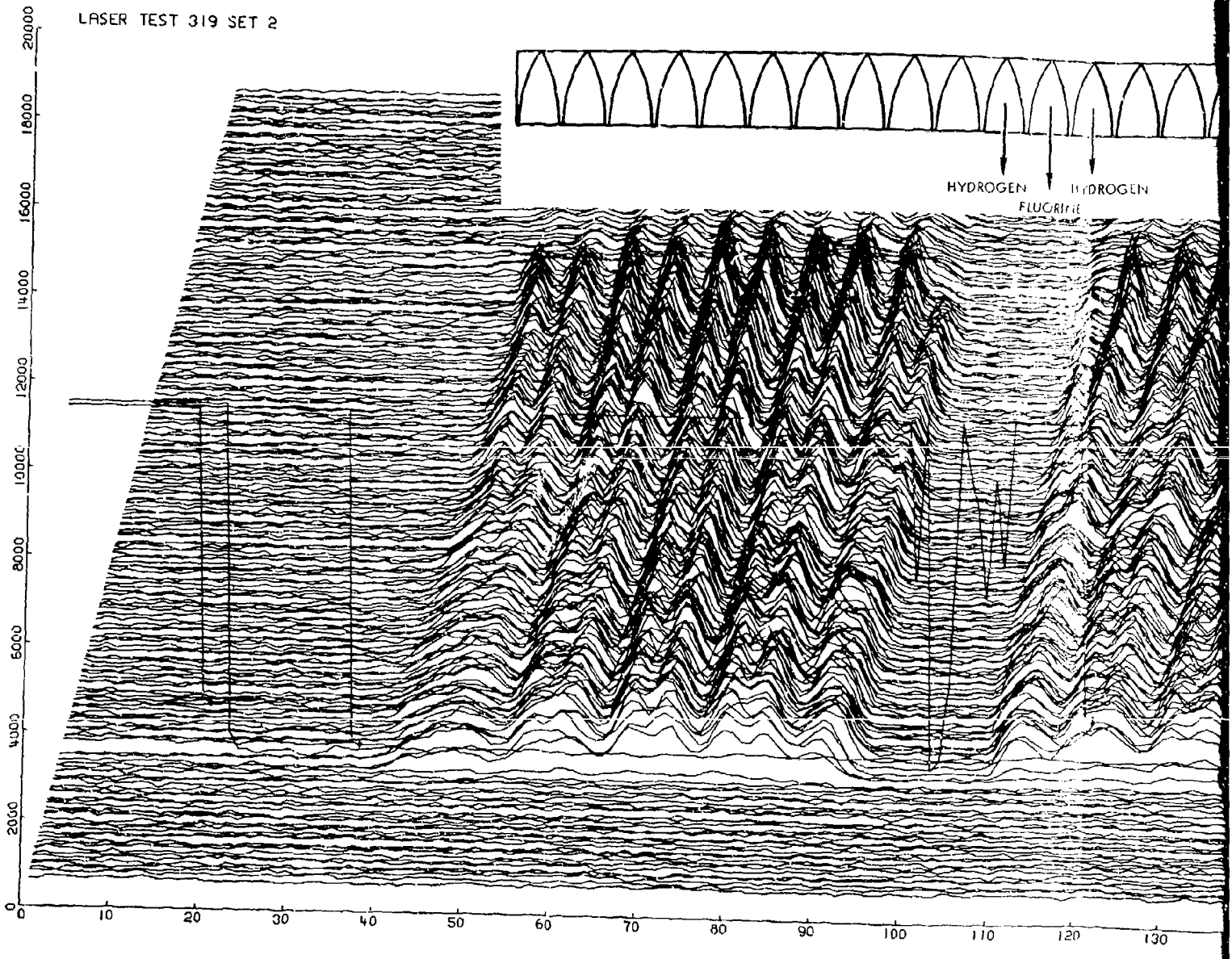

Figure 40. IR Intensity Distribu

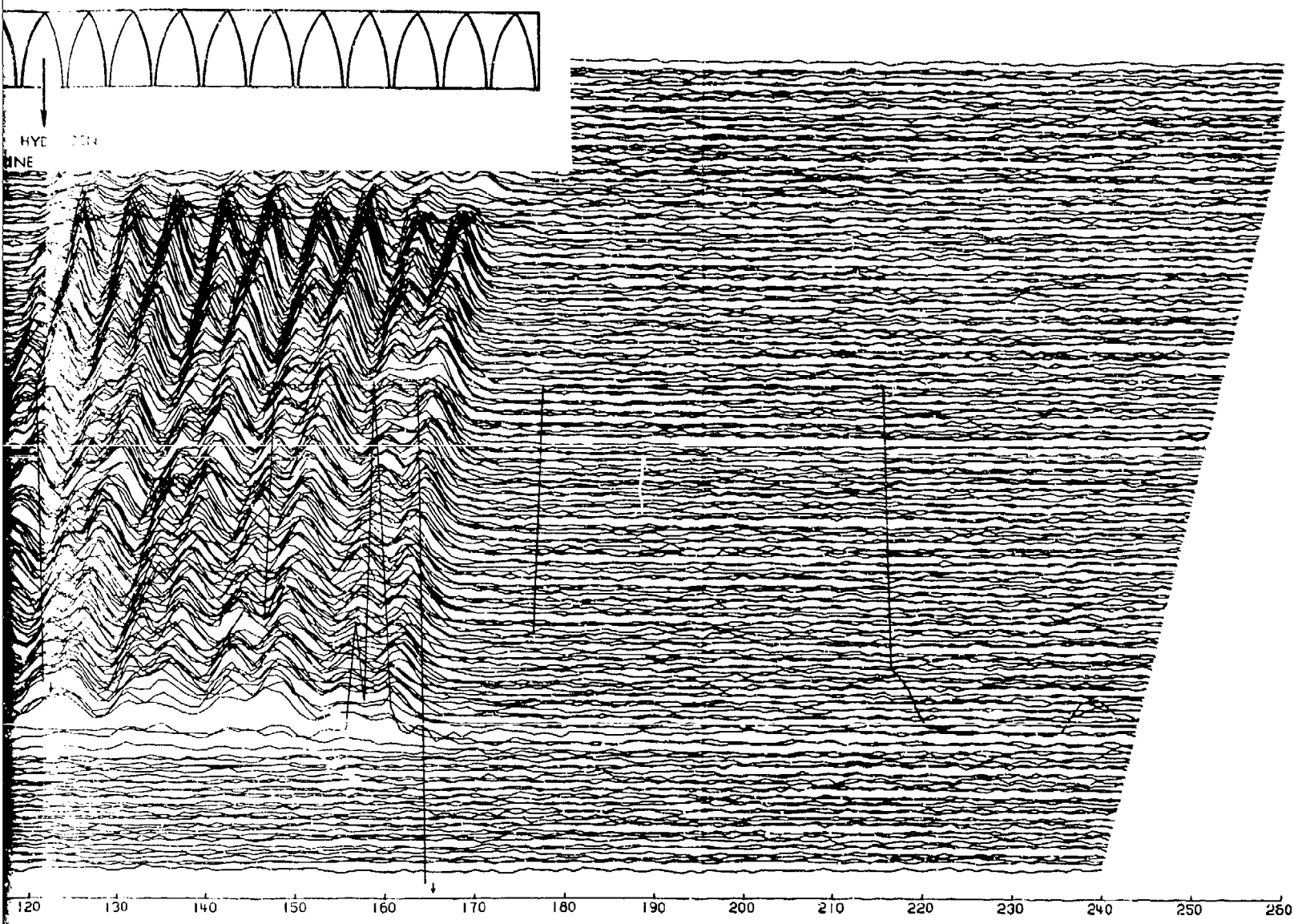

Intensity Distribution—Test 319, Set 2

2

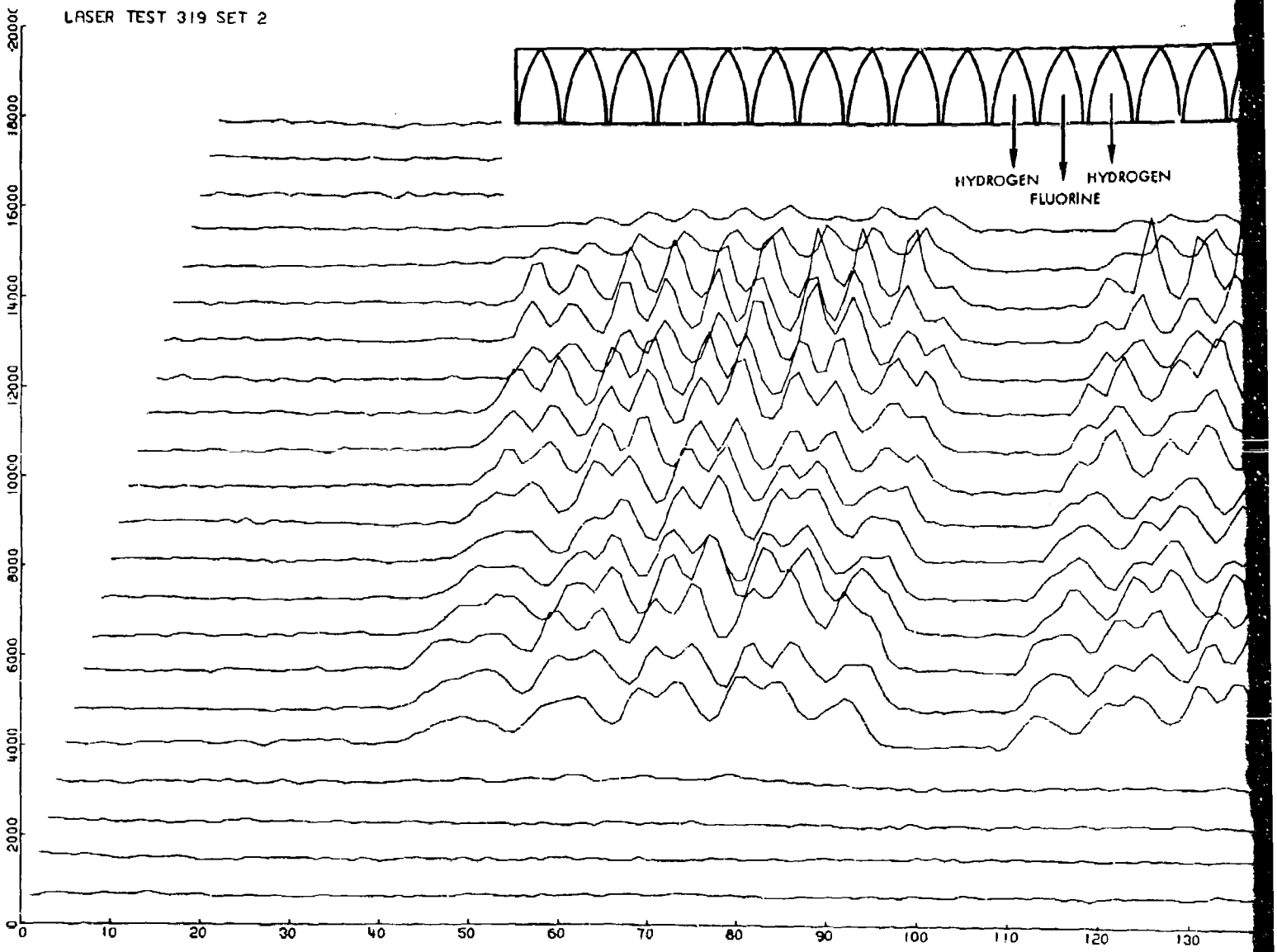

Figure 41. IR Intensity Distribution— T

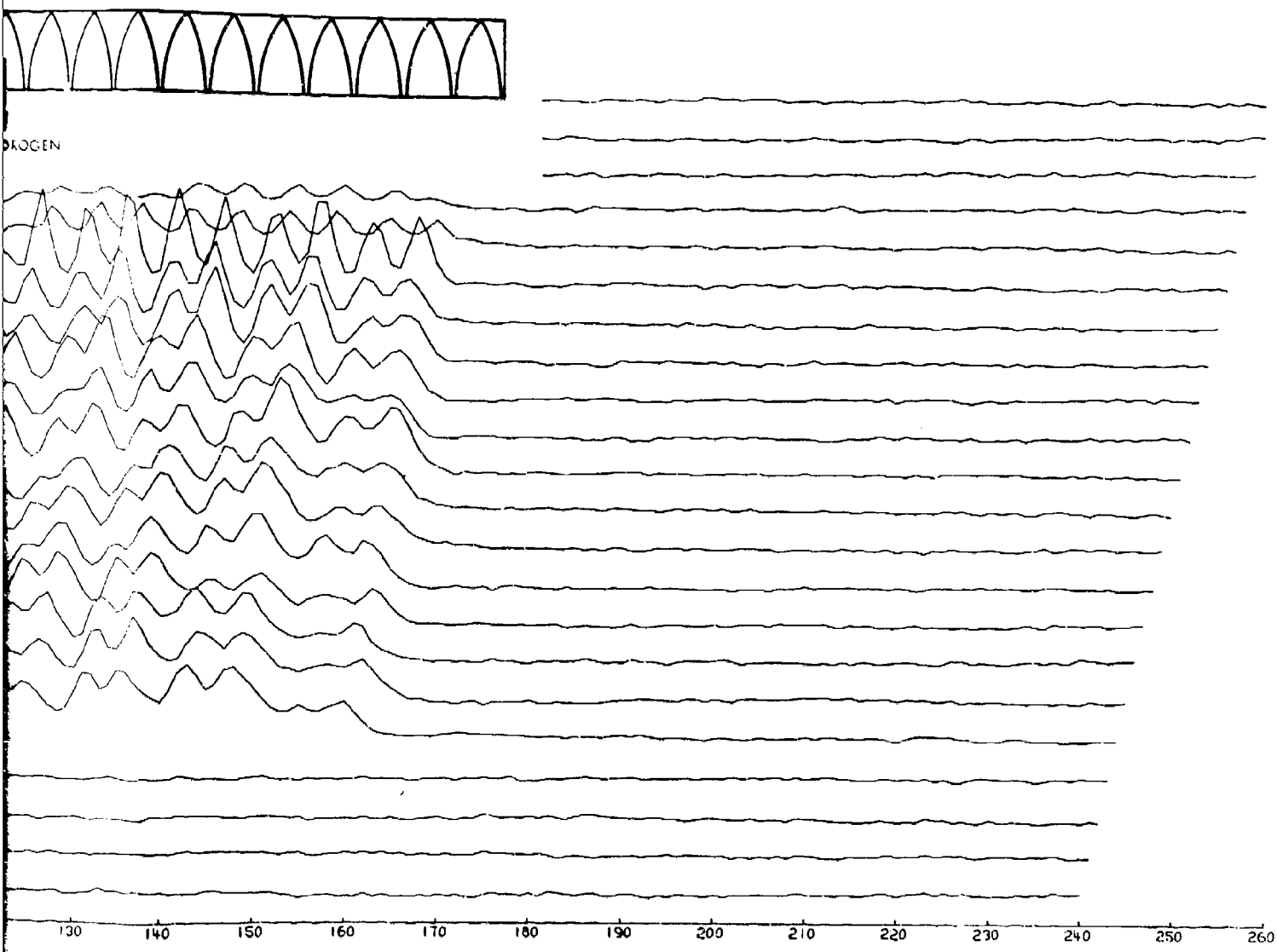

tribution– Test 319, Set 2 (every 10th scan line)

2

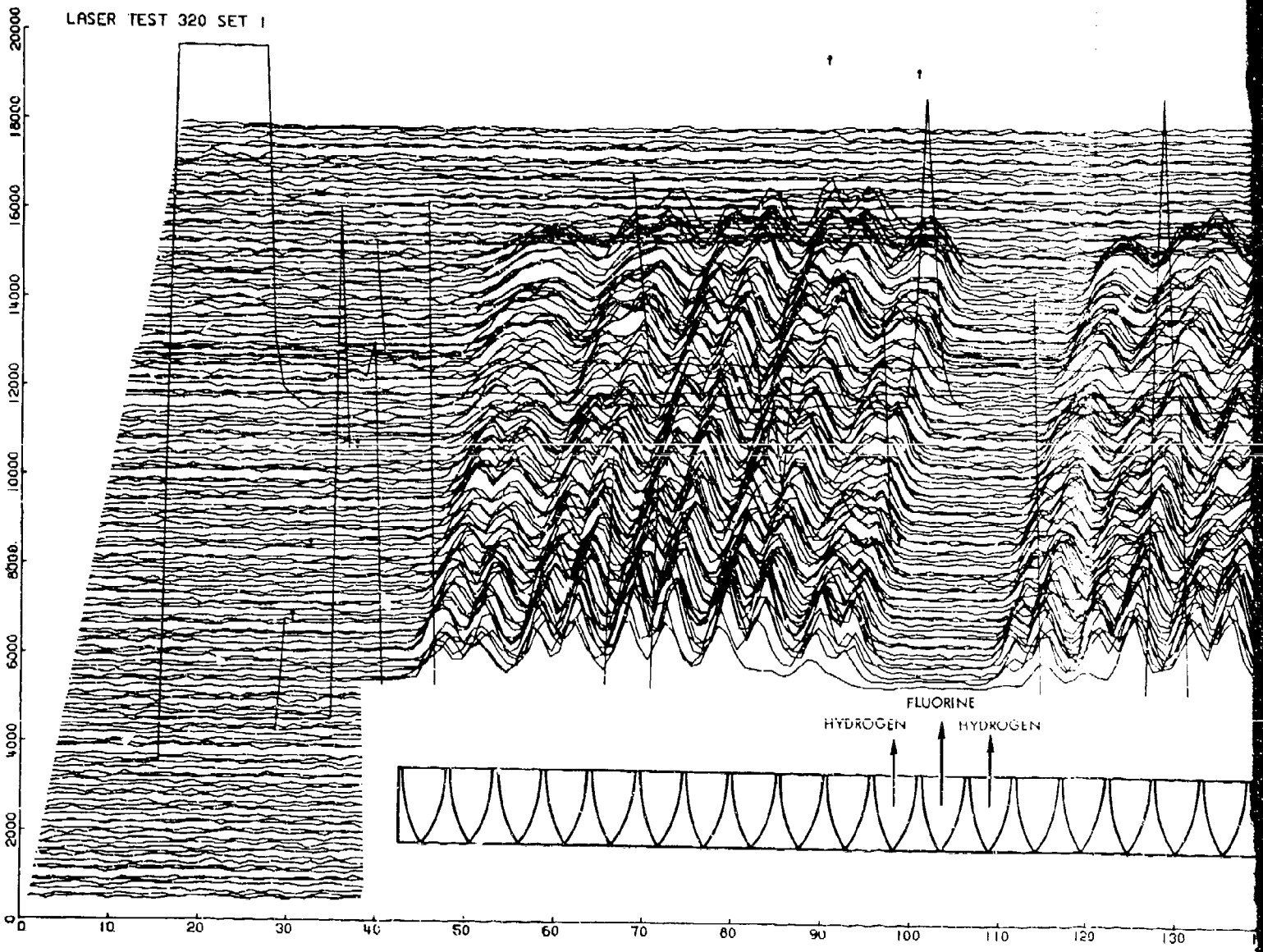

Figure 42. IR Intensity Di

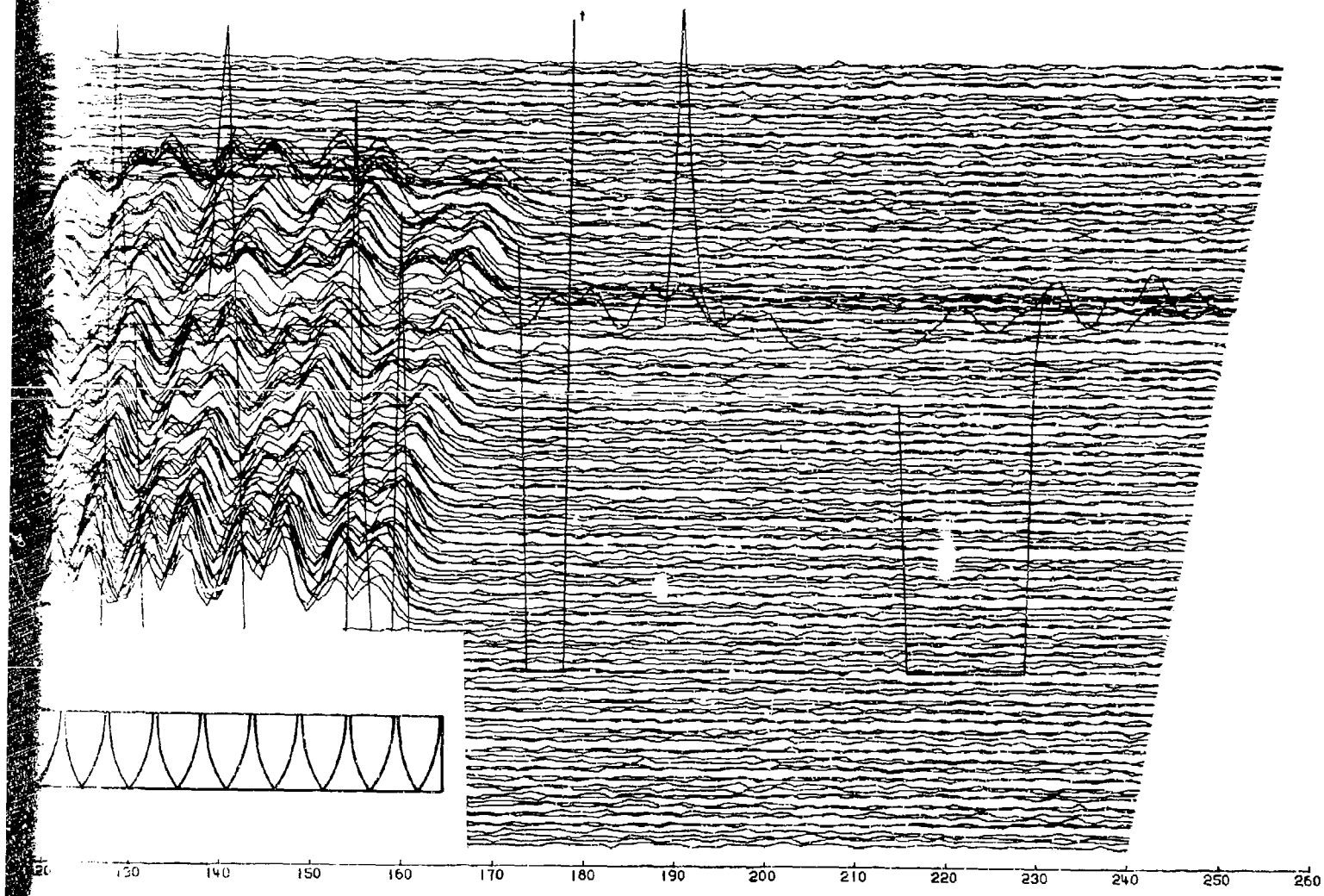

2. H Intensity Distribution — Test 320, Set 1

2

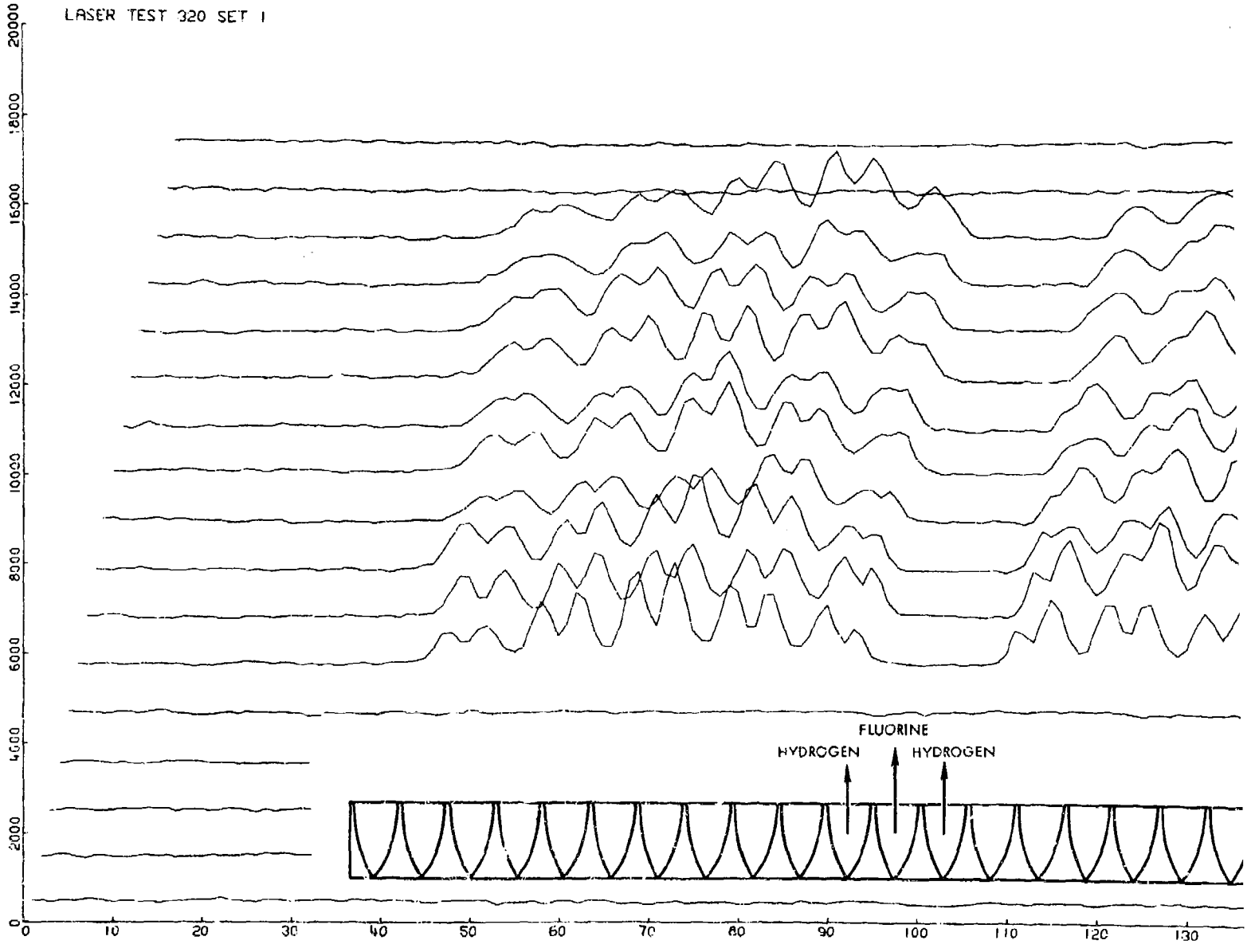

Figure 43. IR Intensity Distribution Test 32

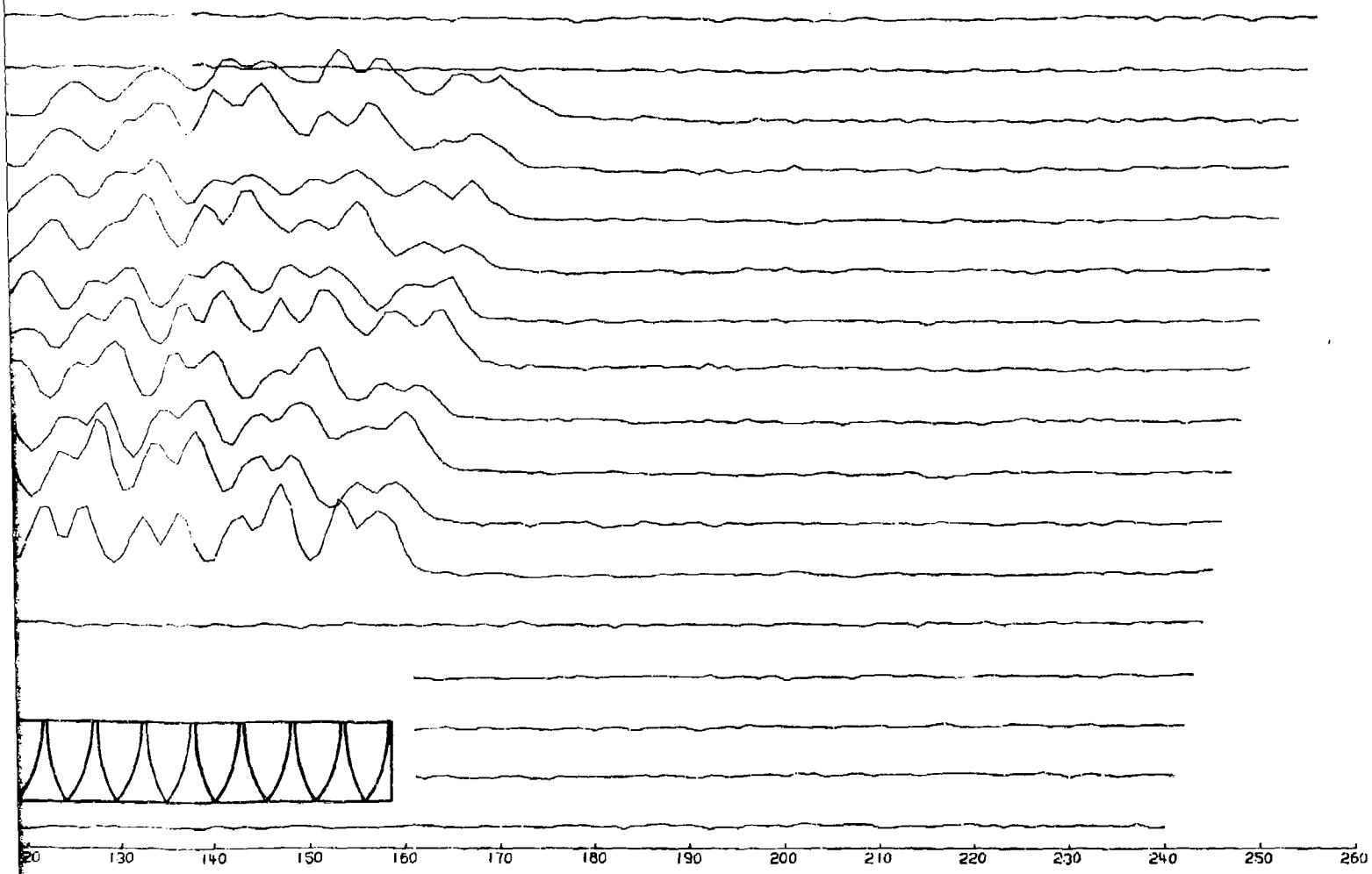

lbution Test 320, Set 1 (every 10th scan line)

2

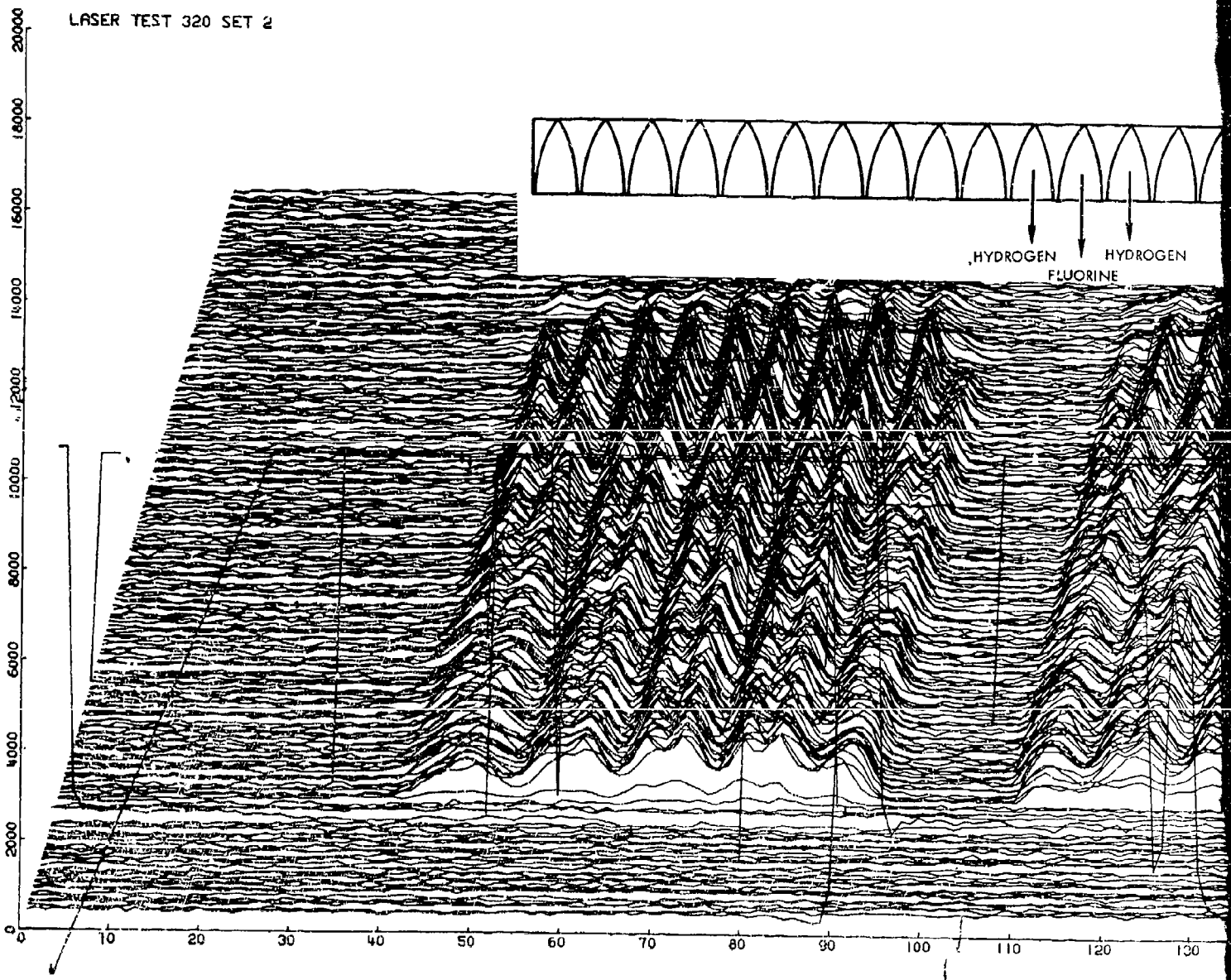

Figure 44. IR Intensity Distr

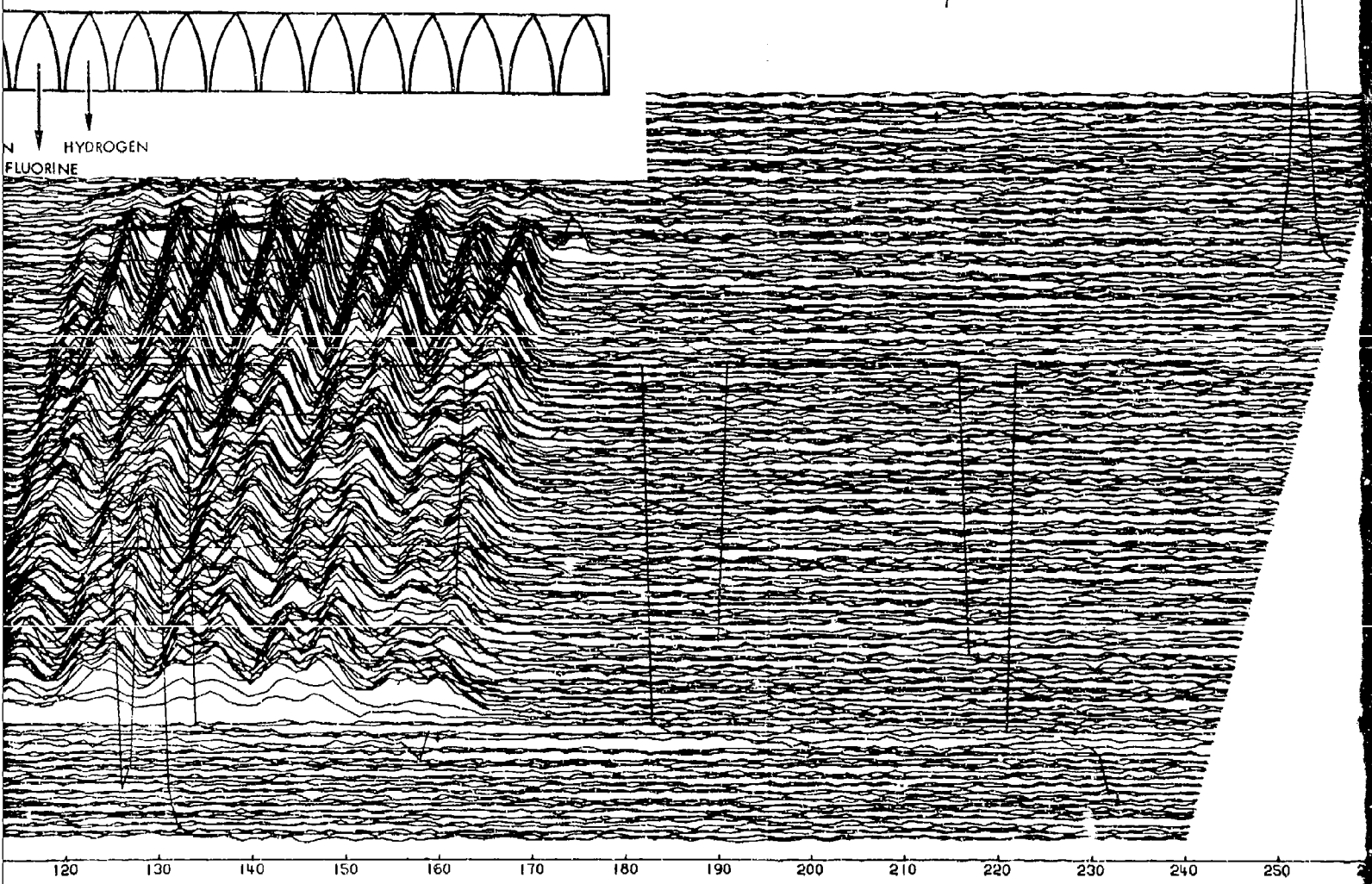

IR Intensity Distribution--Test 320, Set 2

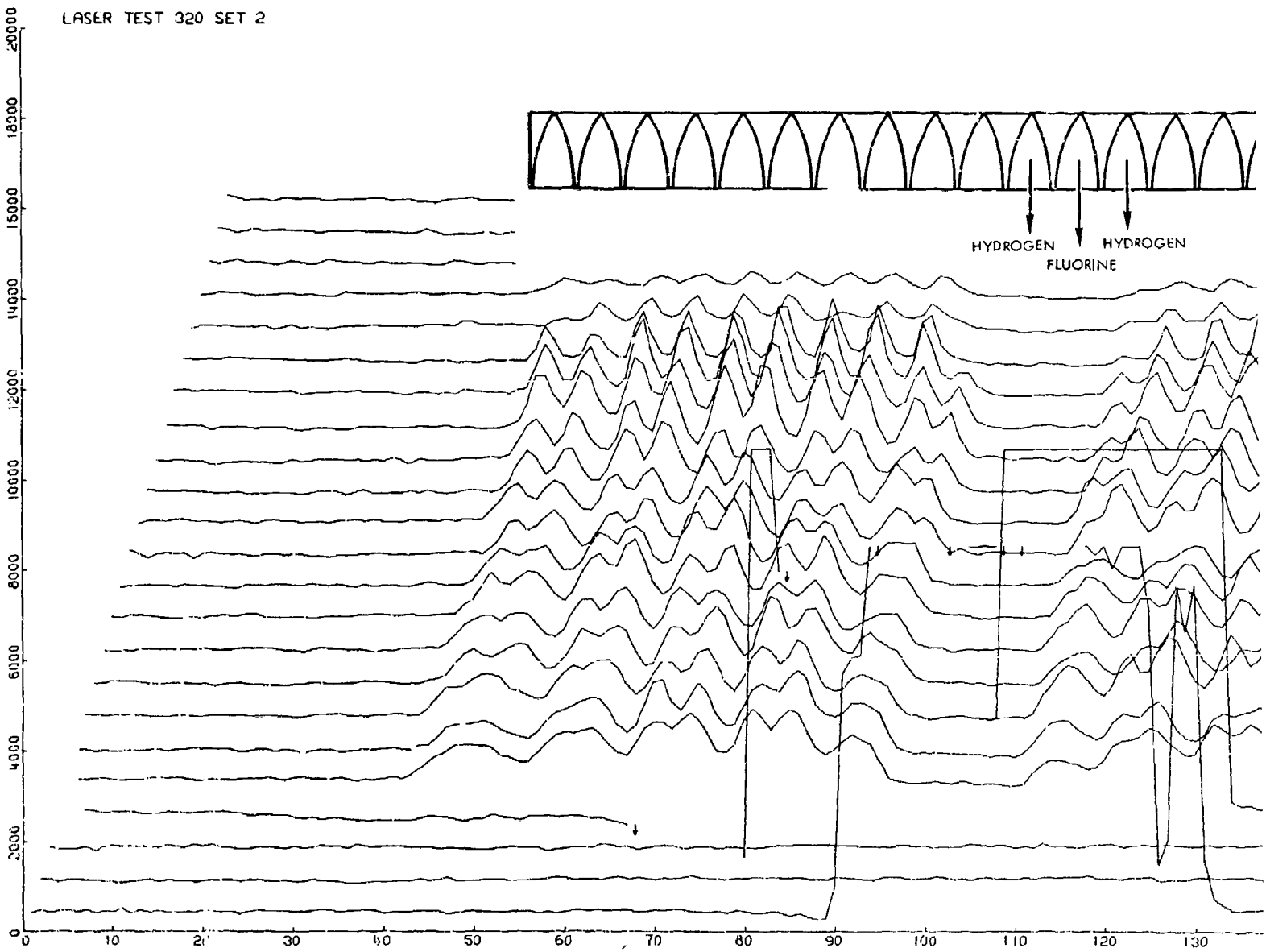

Figure 45. IR Intensity Distribution--Test

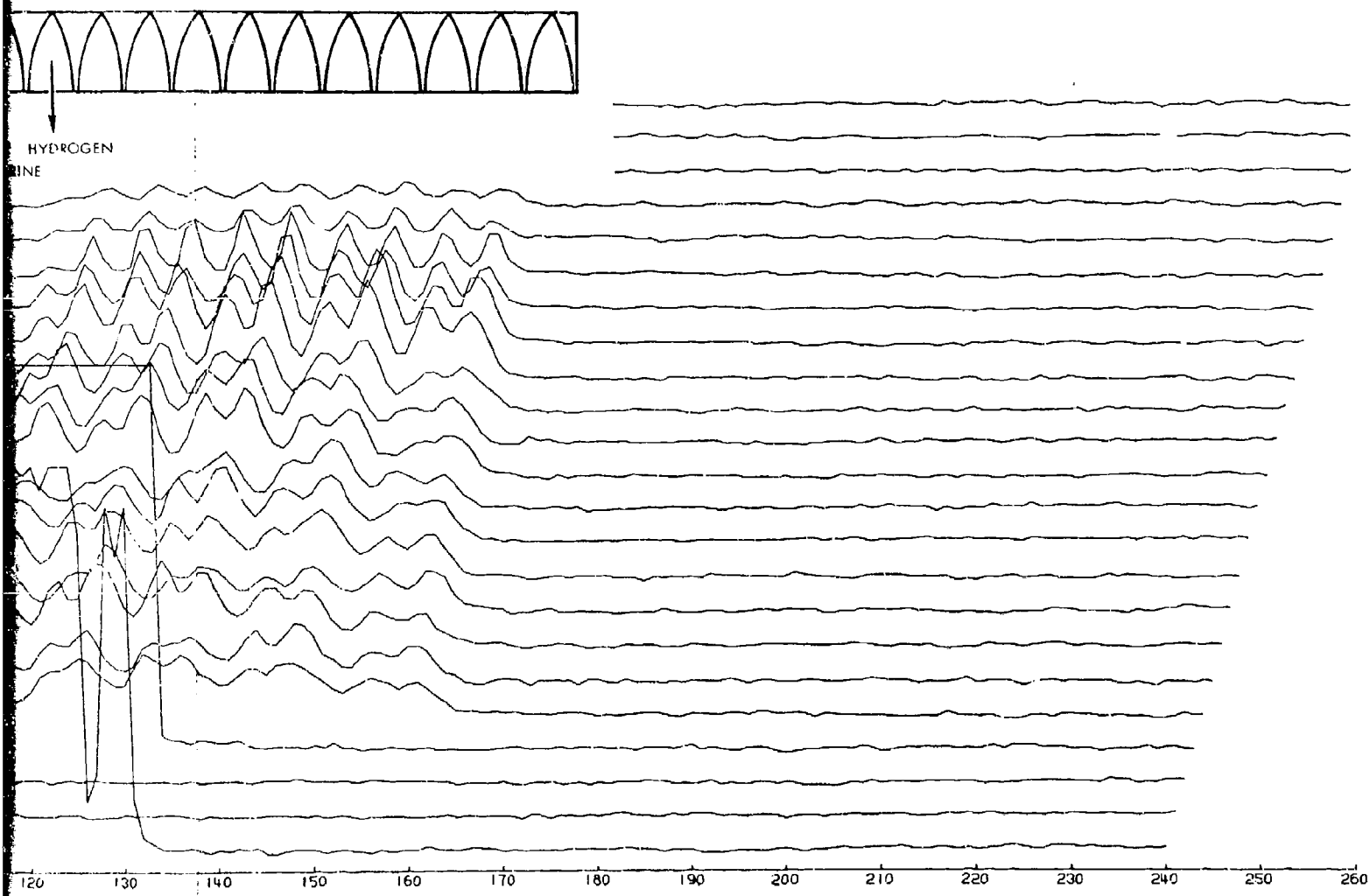

Distribution--Test 320, Set 2 (every 10th scan line)

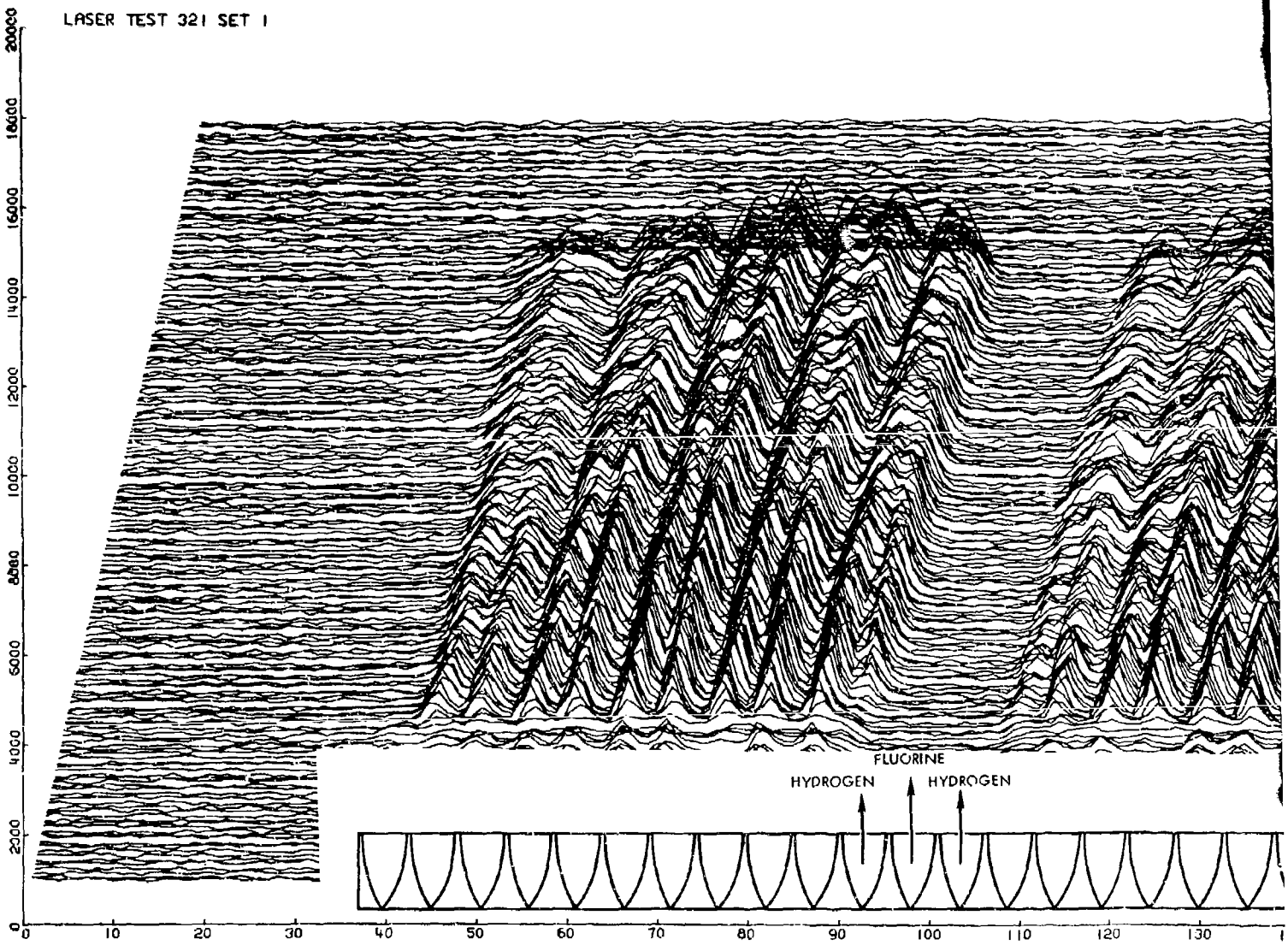

Figure 46. IR Intensity Distributio

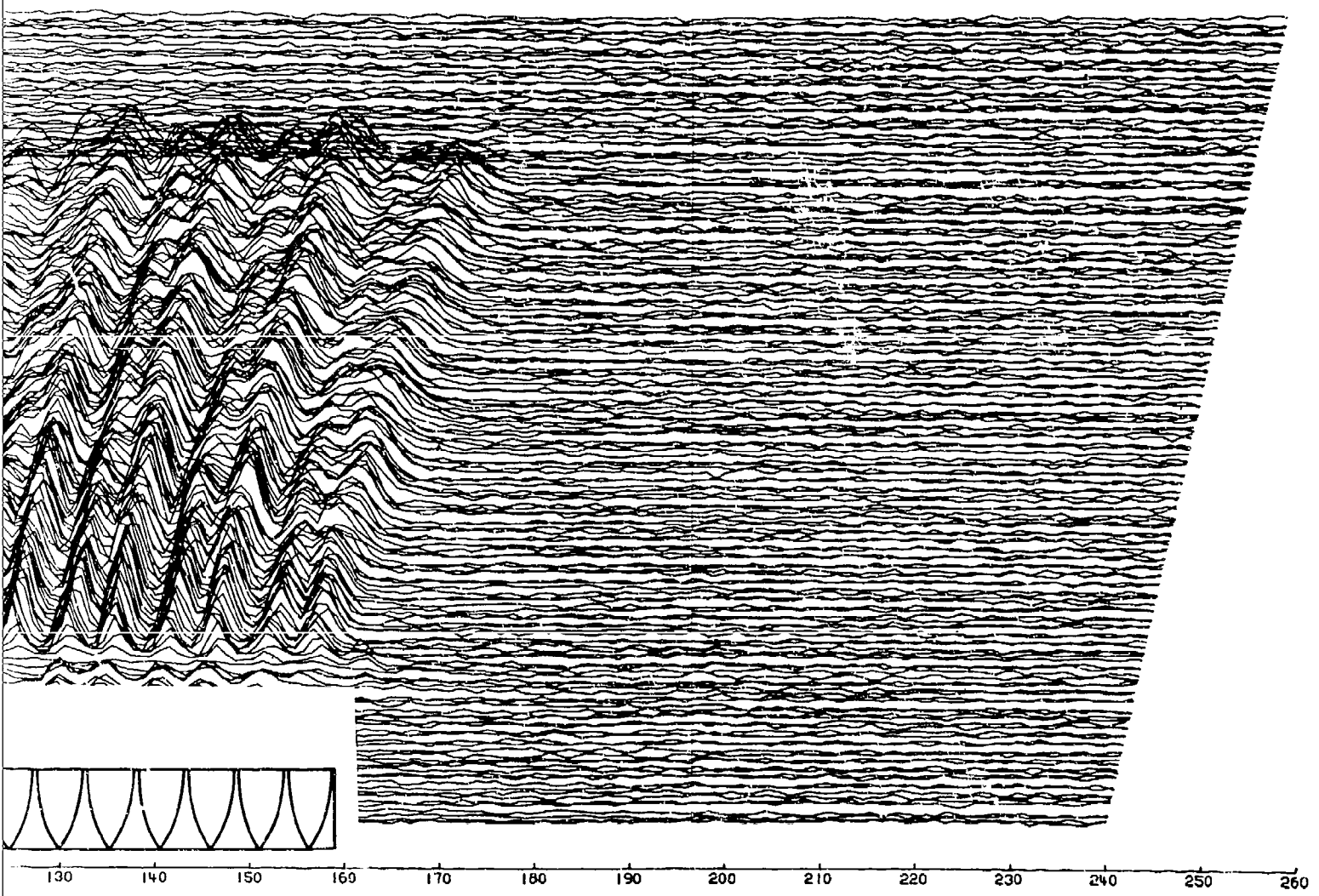

y Distribution--Test 321, Set 1

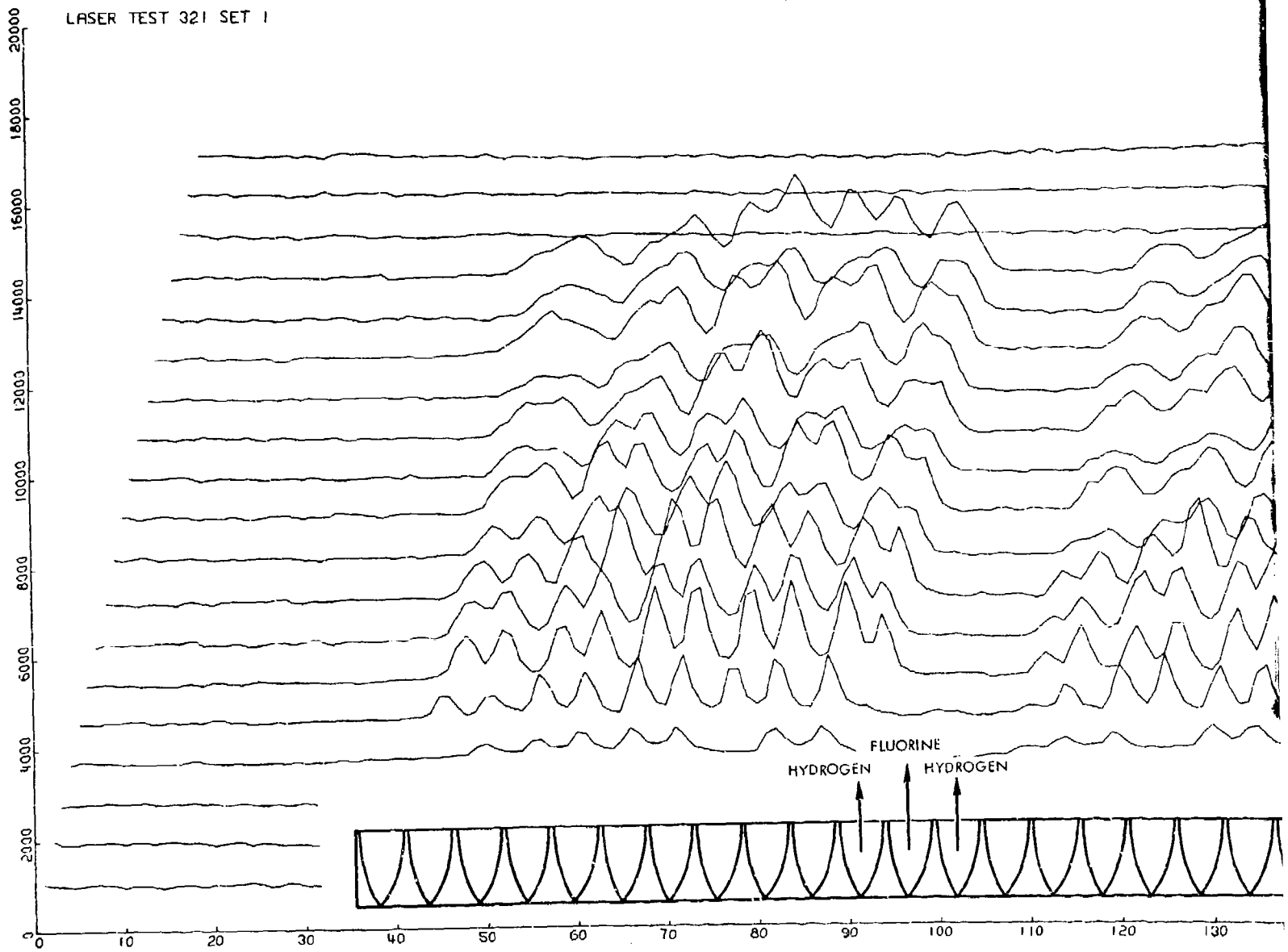

Figure 47. IR Intensity Distribution--Te

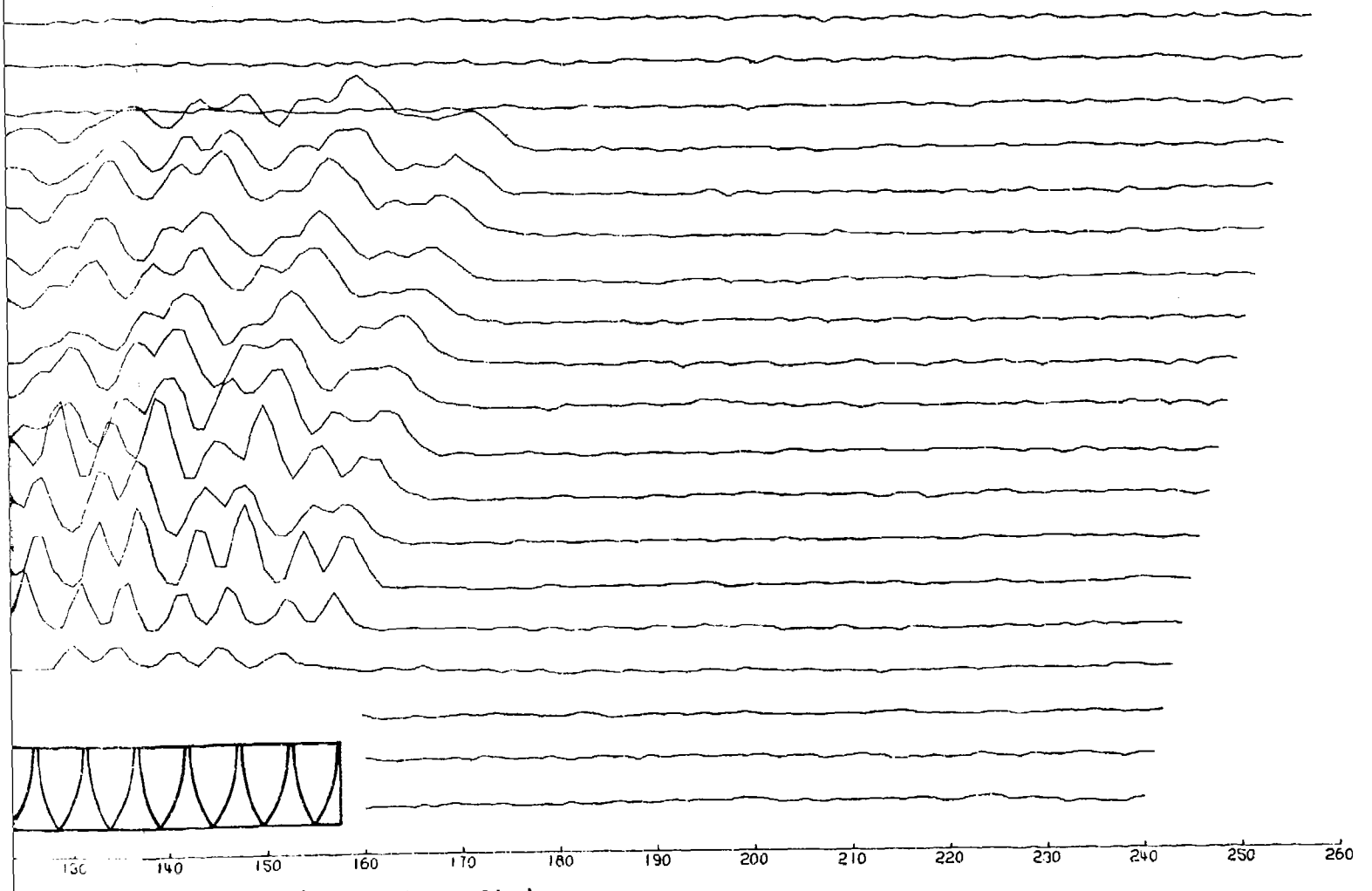

ribution--Test 321, Set 1 (every 10th scan line)

2

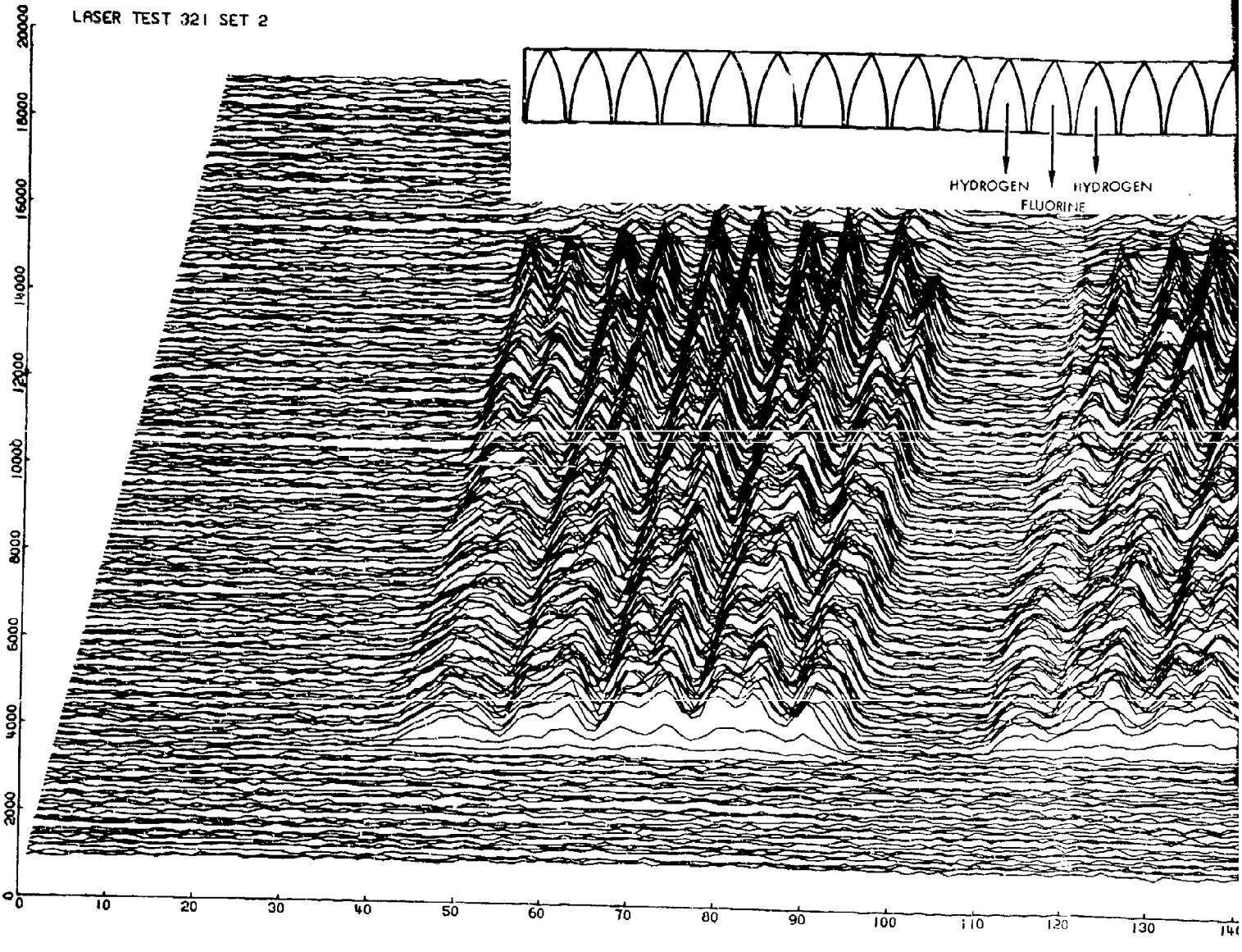

Figure 48. IR Intensity Distributi

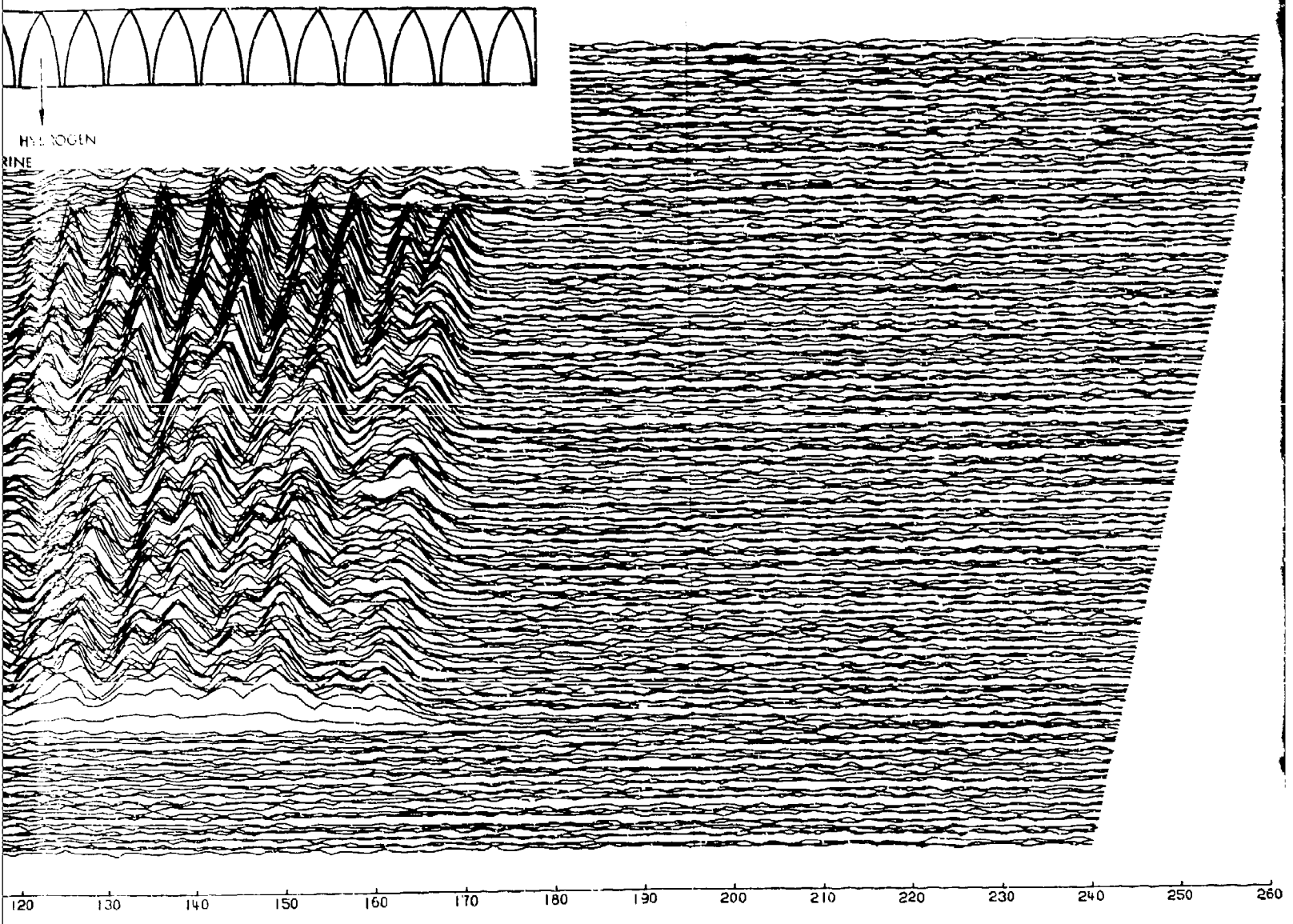

Intensity Distribution--Test 321, Set 2

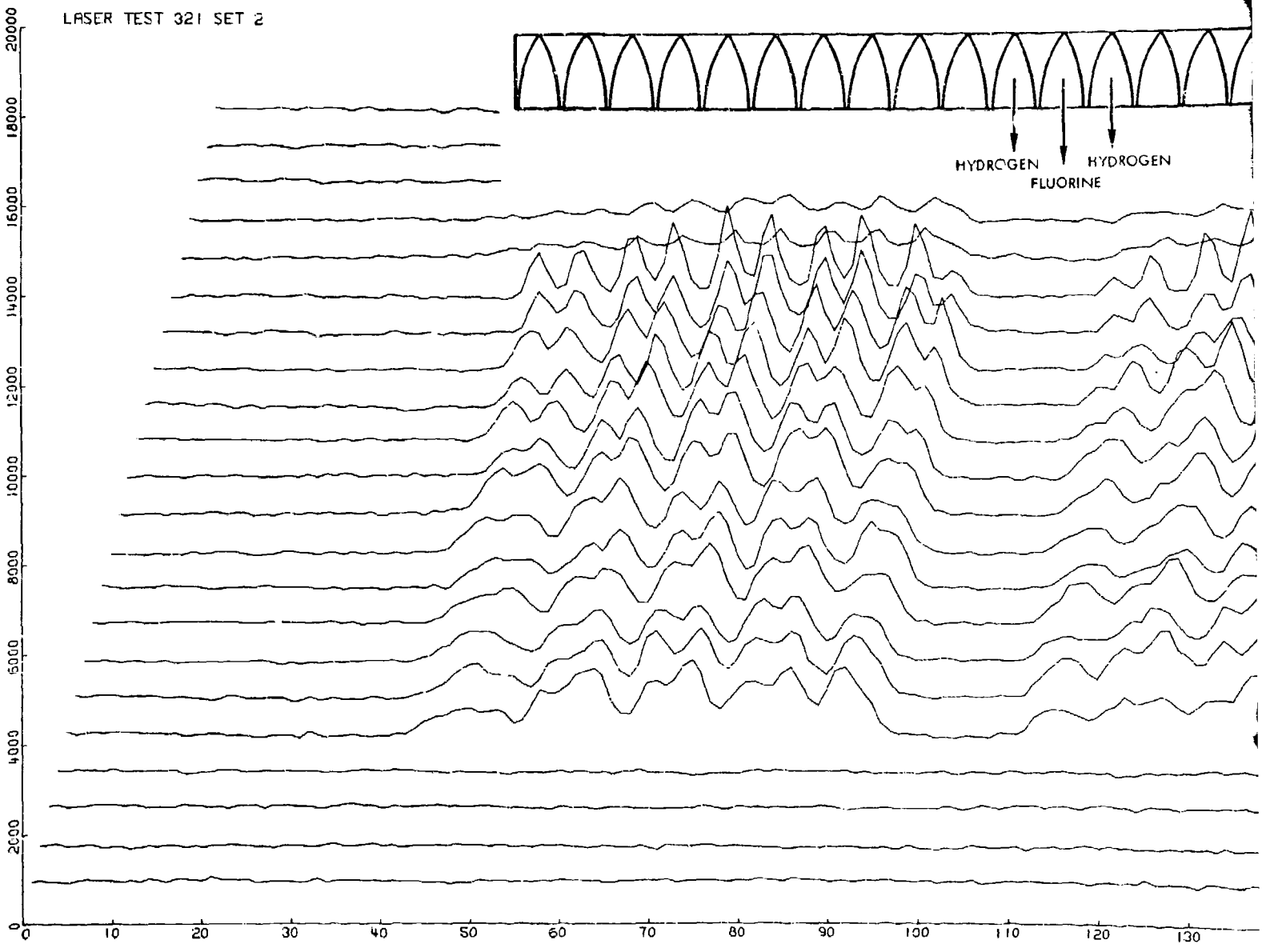

Figure 49. IR Intensity Distribution--Test

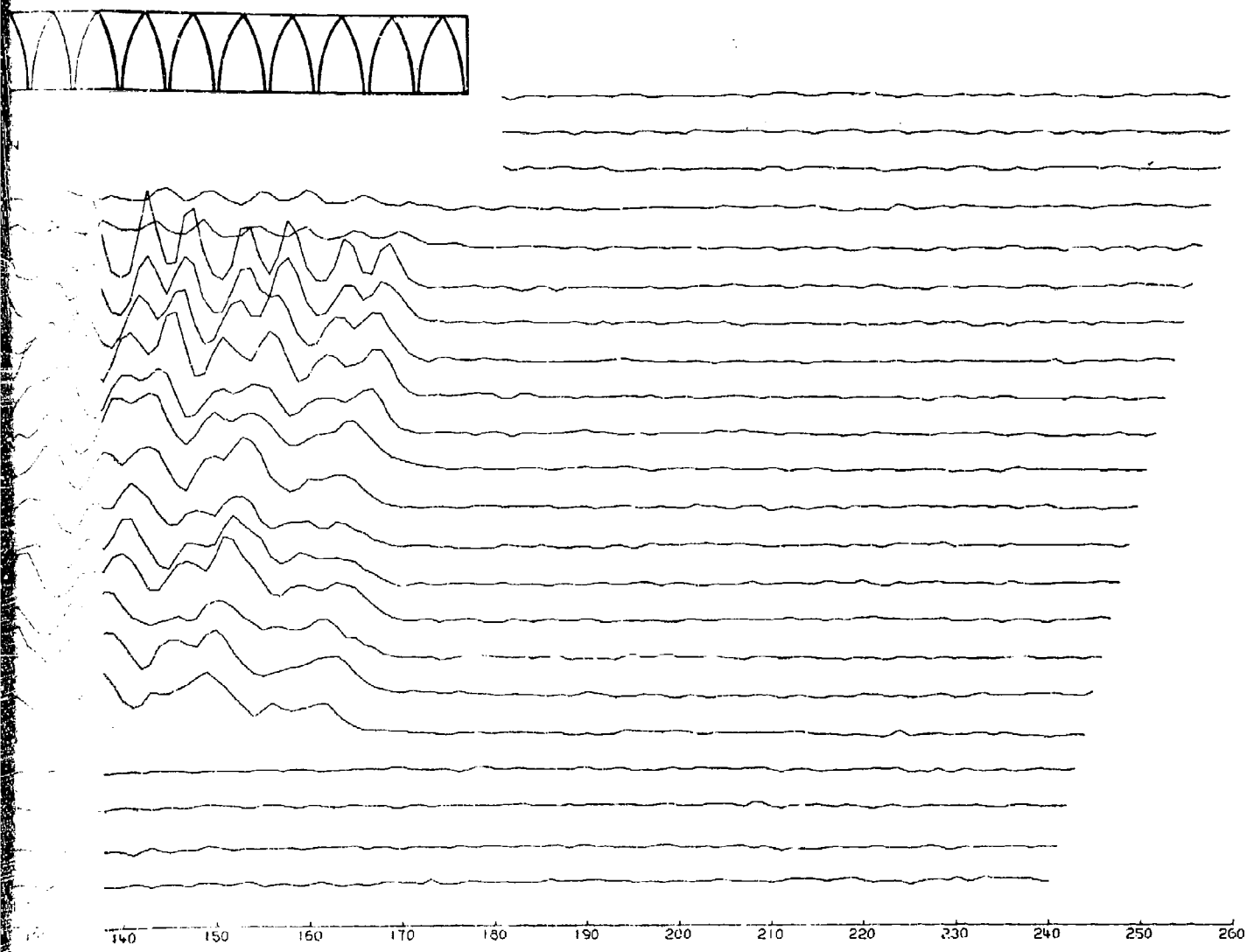

Ilion--Test 321, Set 2 (every 10th scan line)

2

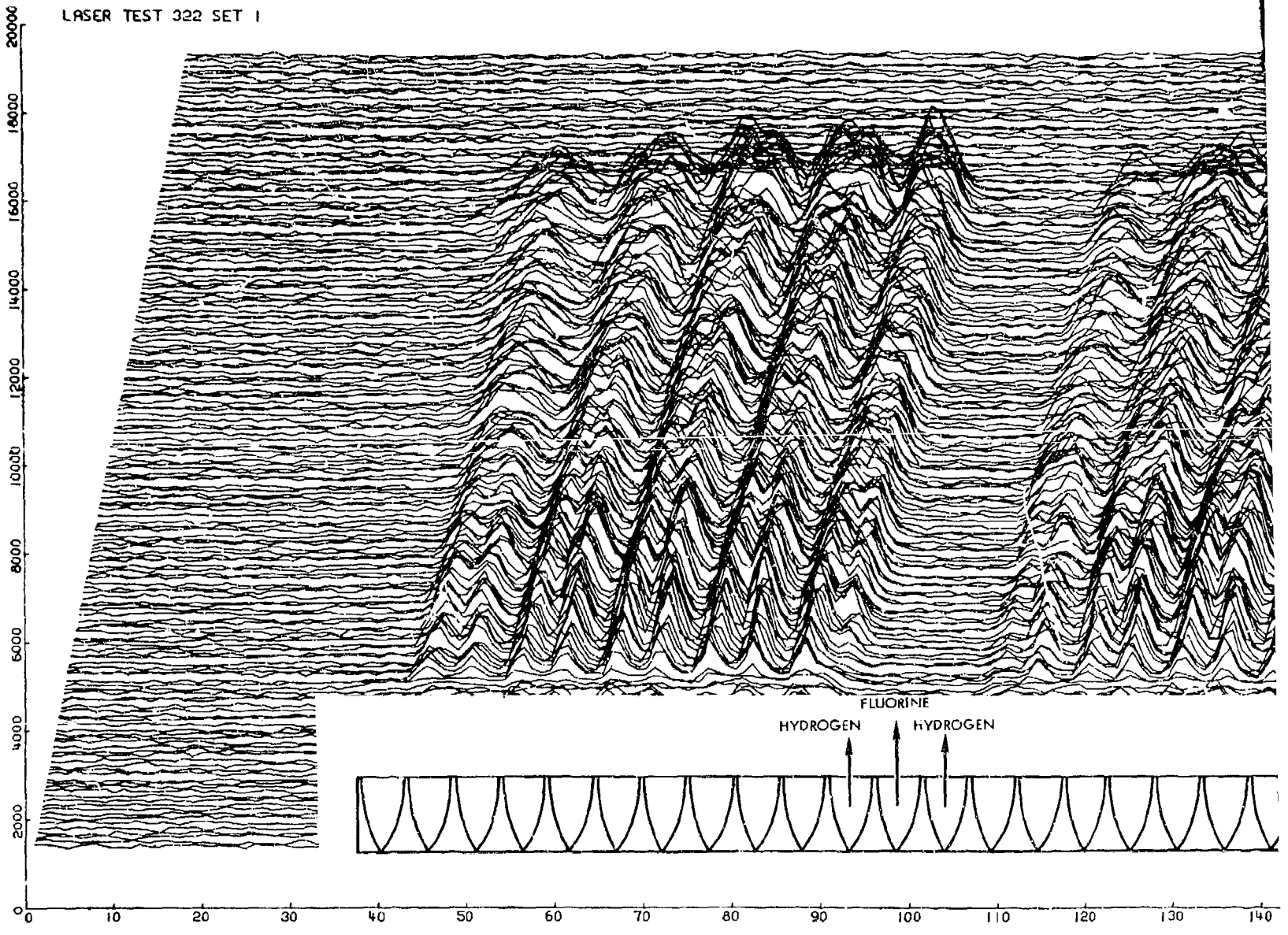

Figure 50. IR Intensity Distribution--Test 32

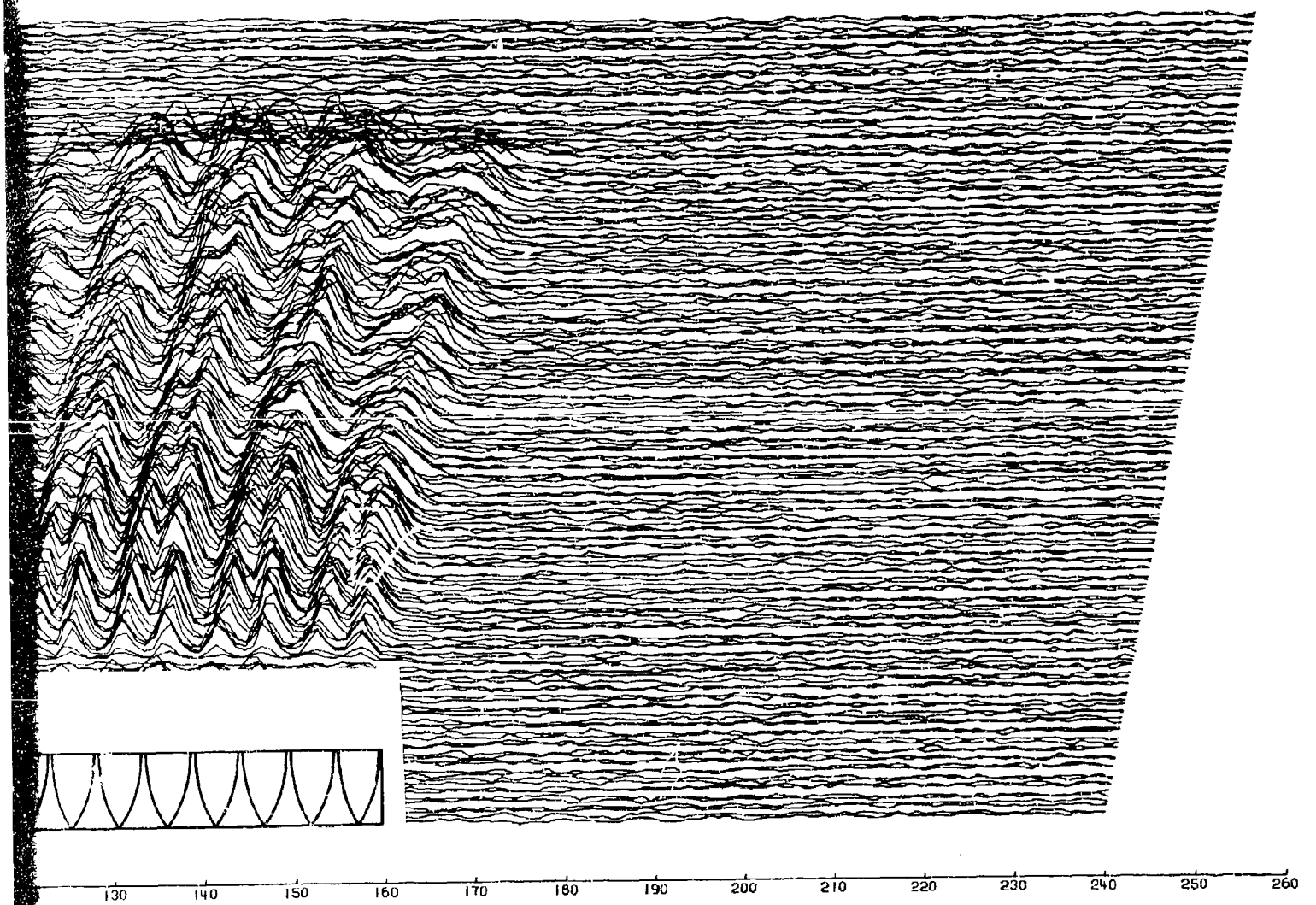

istribution--Test 322, Set 1

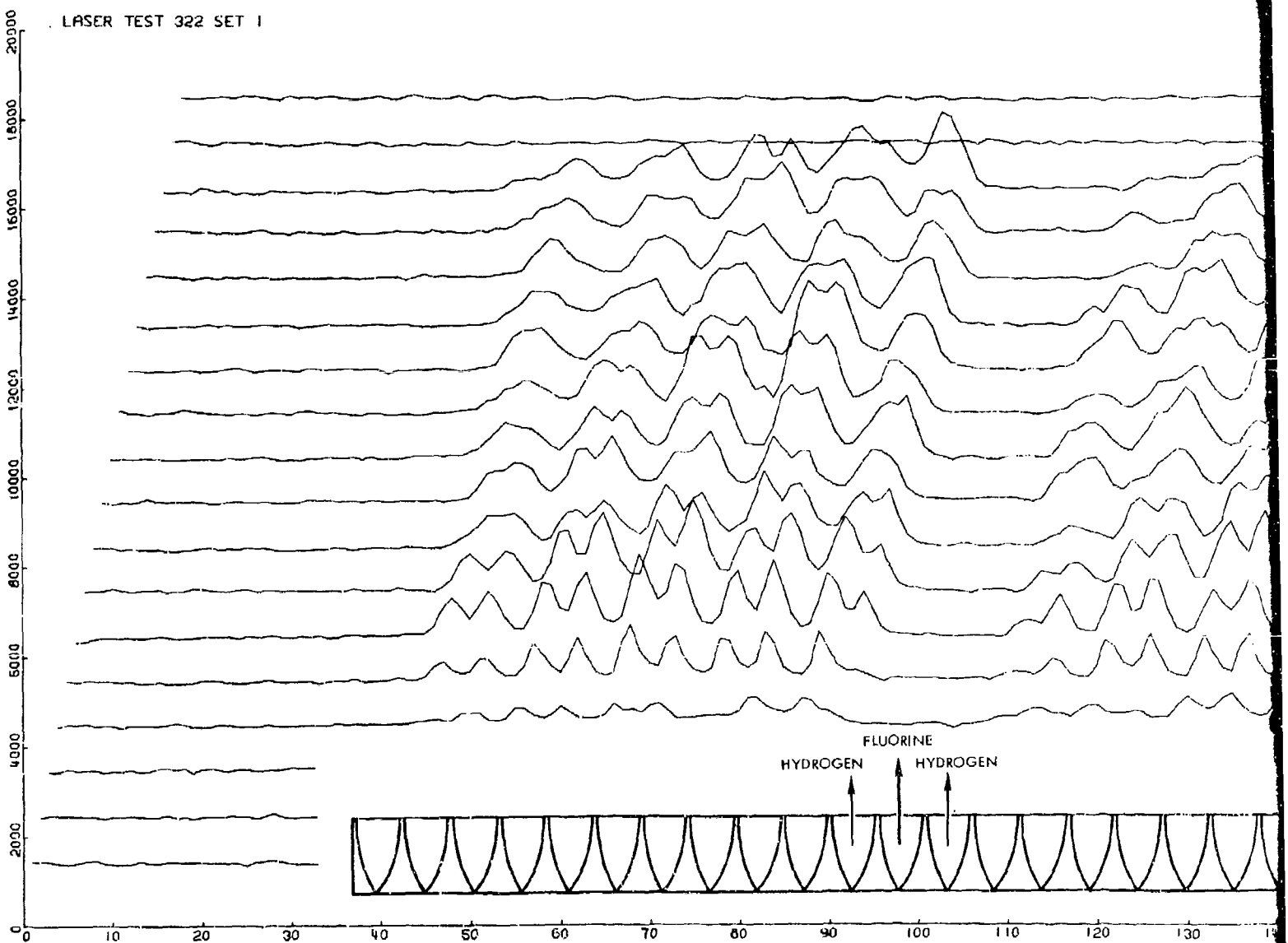

Figure 51. IR Intensity Distribution--Test

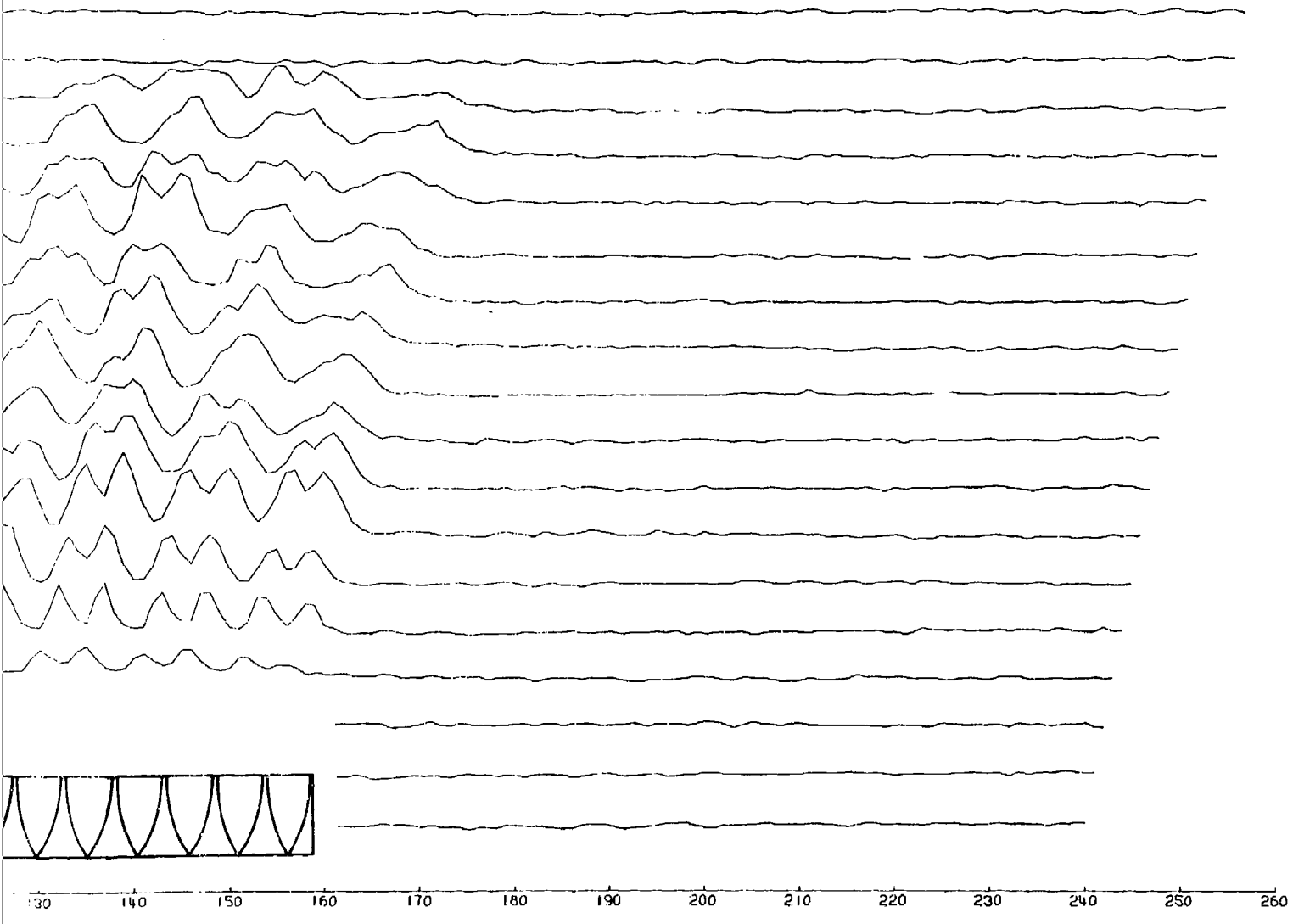

ution--Test 322, Set 1 (every 10th scan line)

2

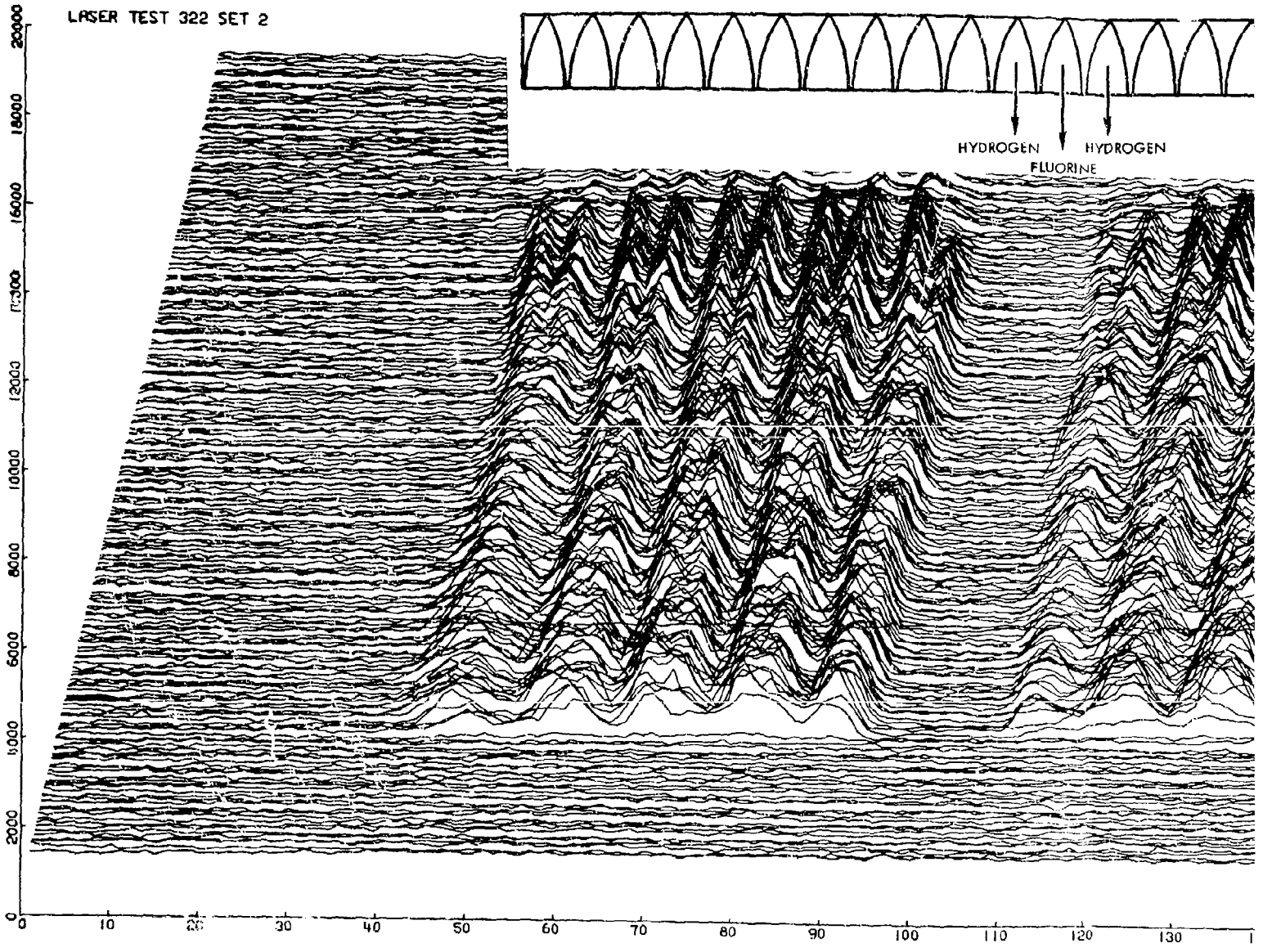

Figure 52. IR Intensity Distribut

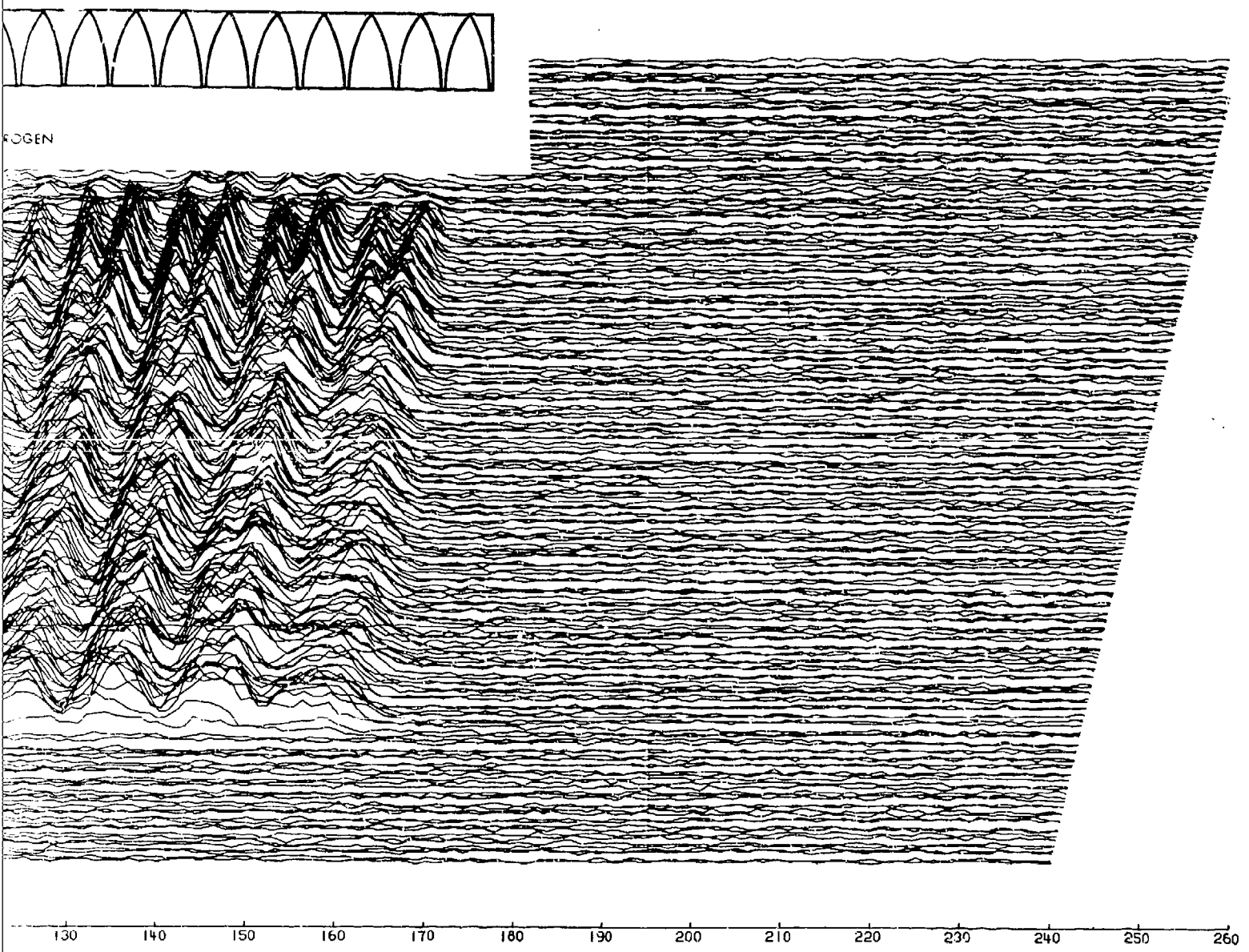

nsity Distribution--Test 322, Set 2

2

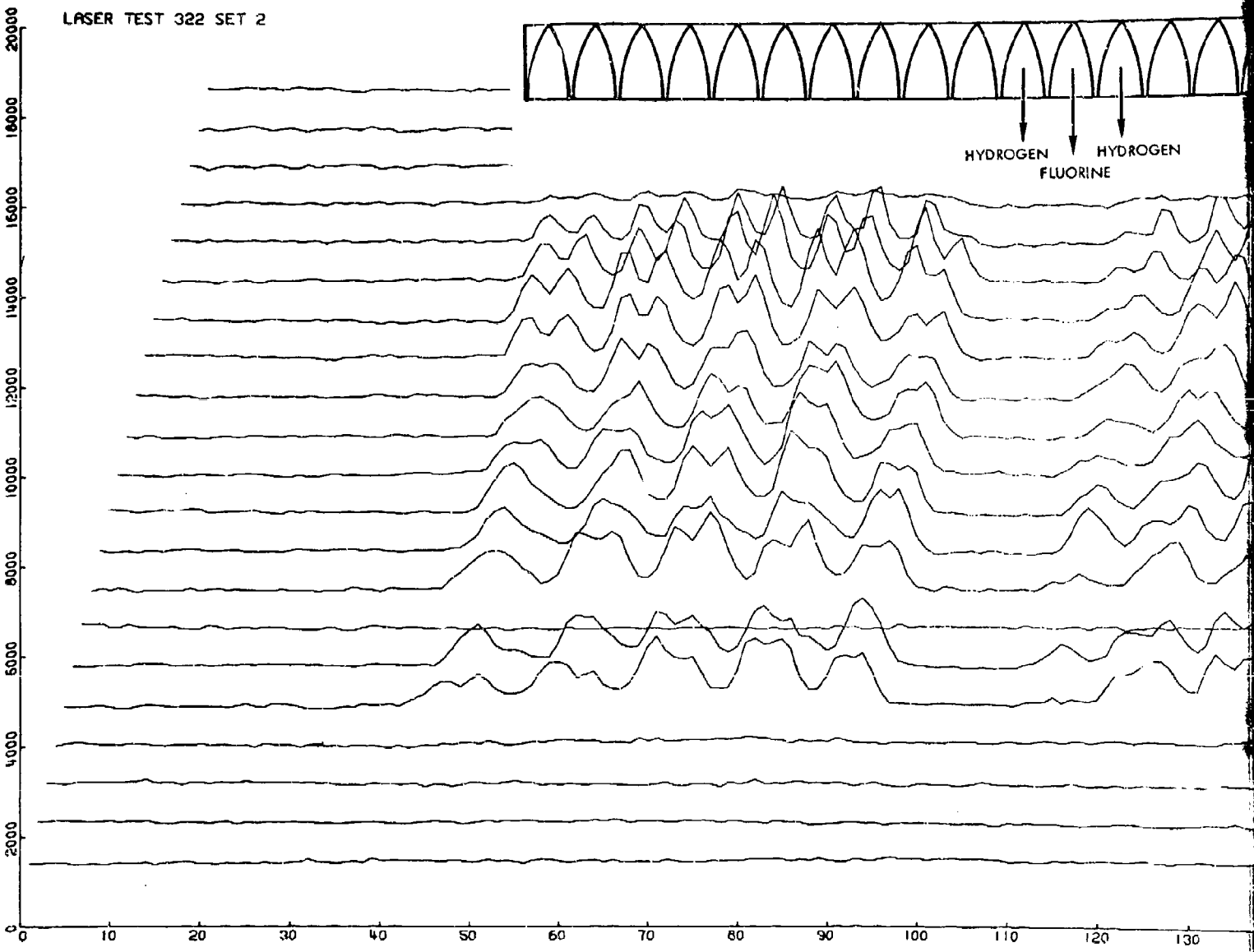

Figure 53. IR Intensity Distribution

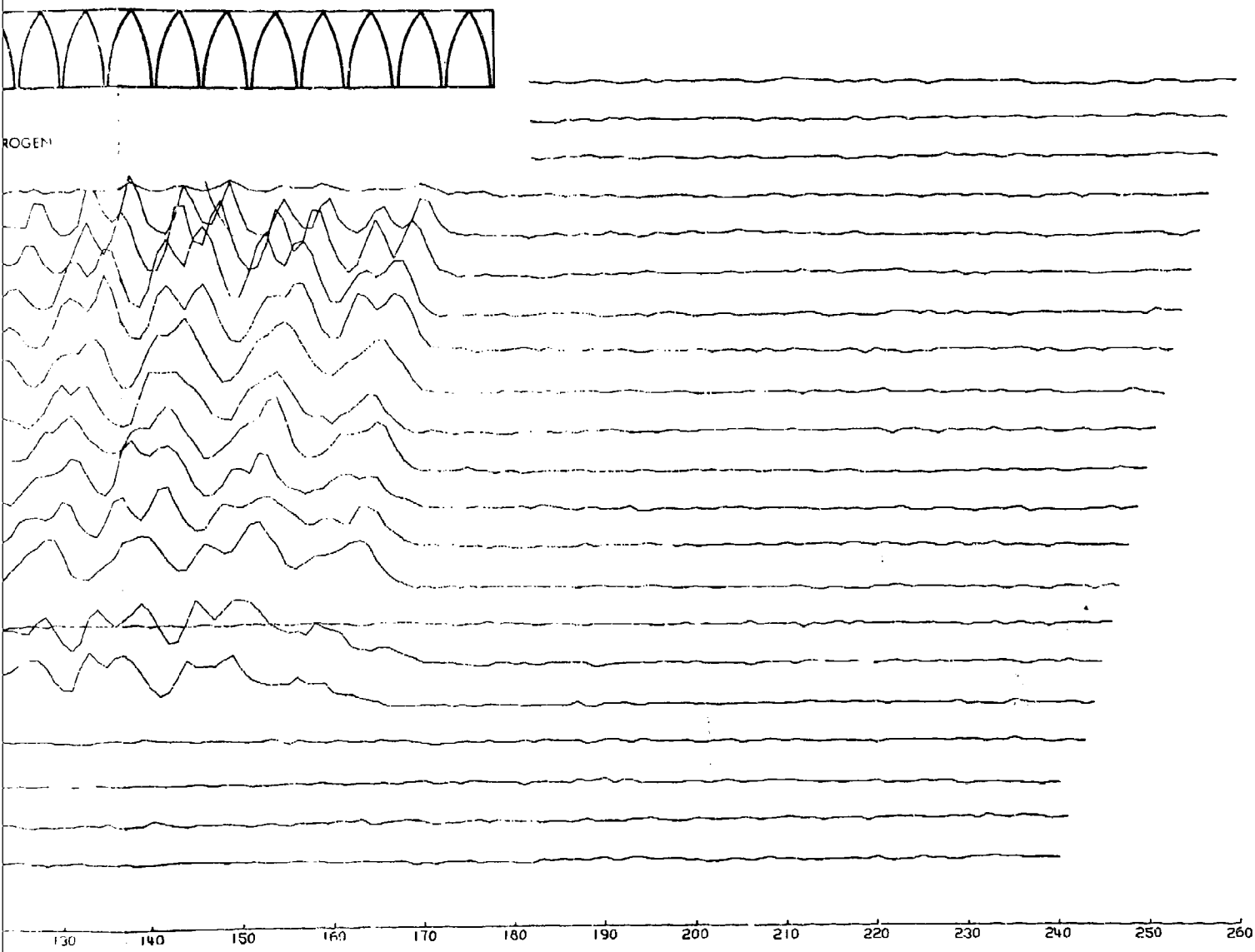

Distribution--Test 322, Set 2 (every 10th scan line)

2

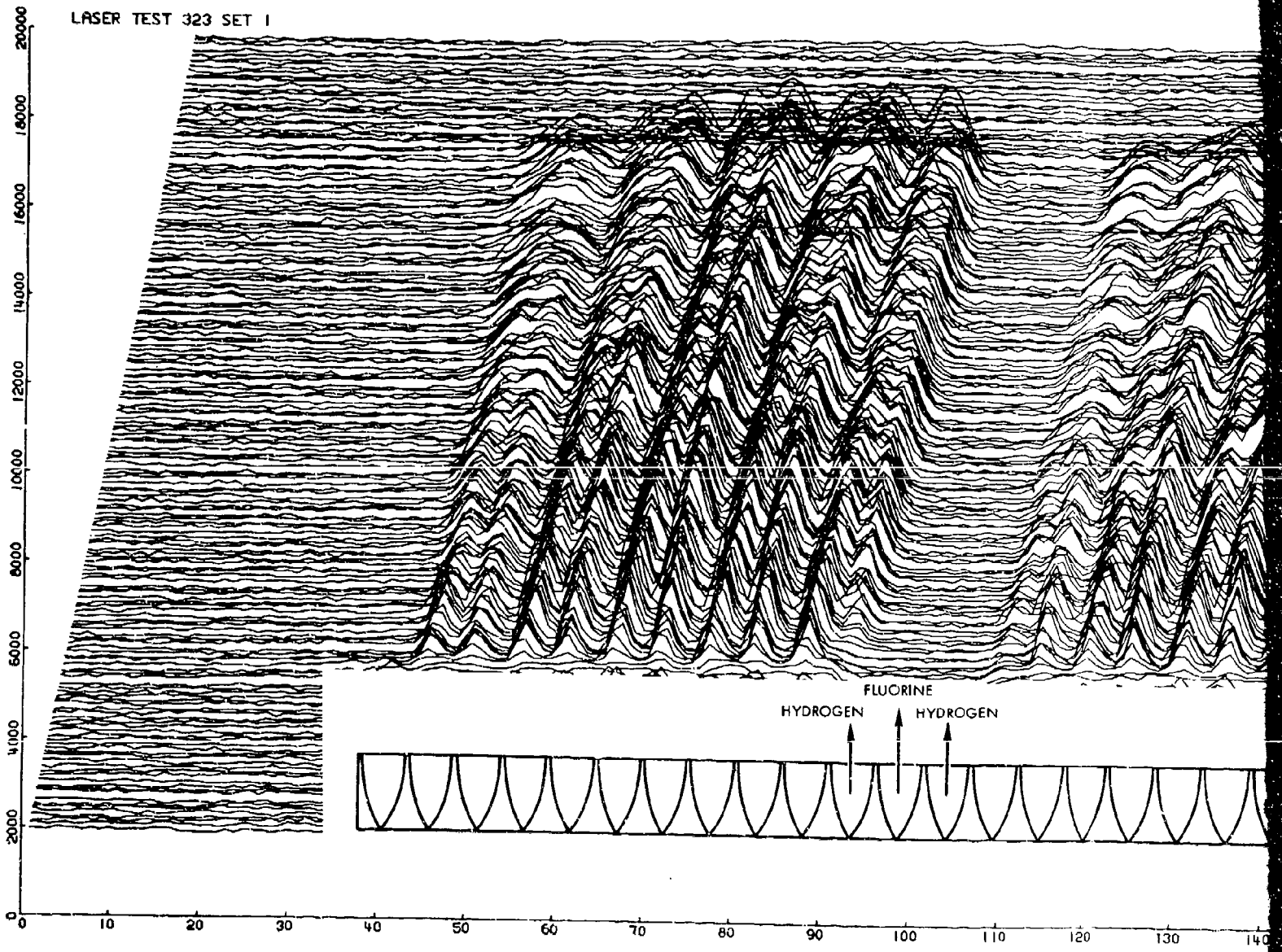

Figure 54. IR Intensity Distribut

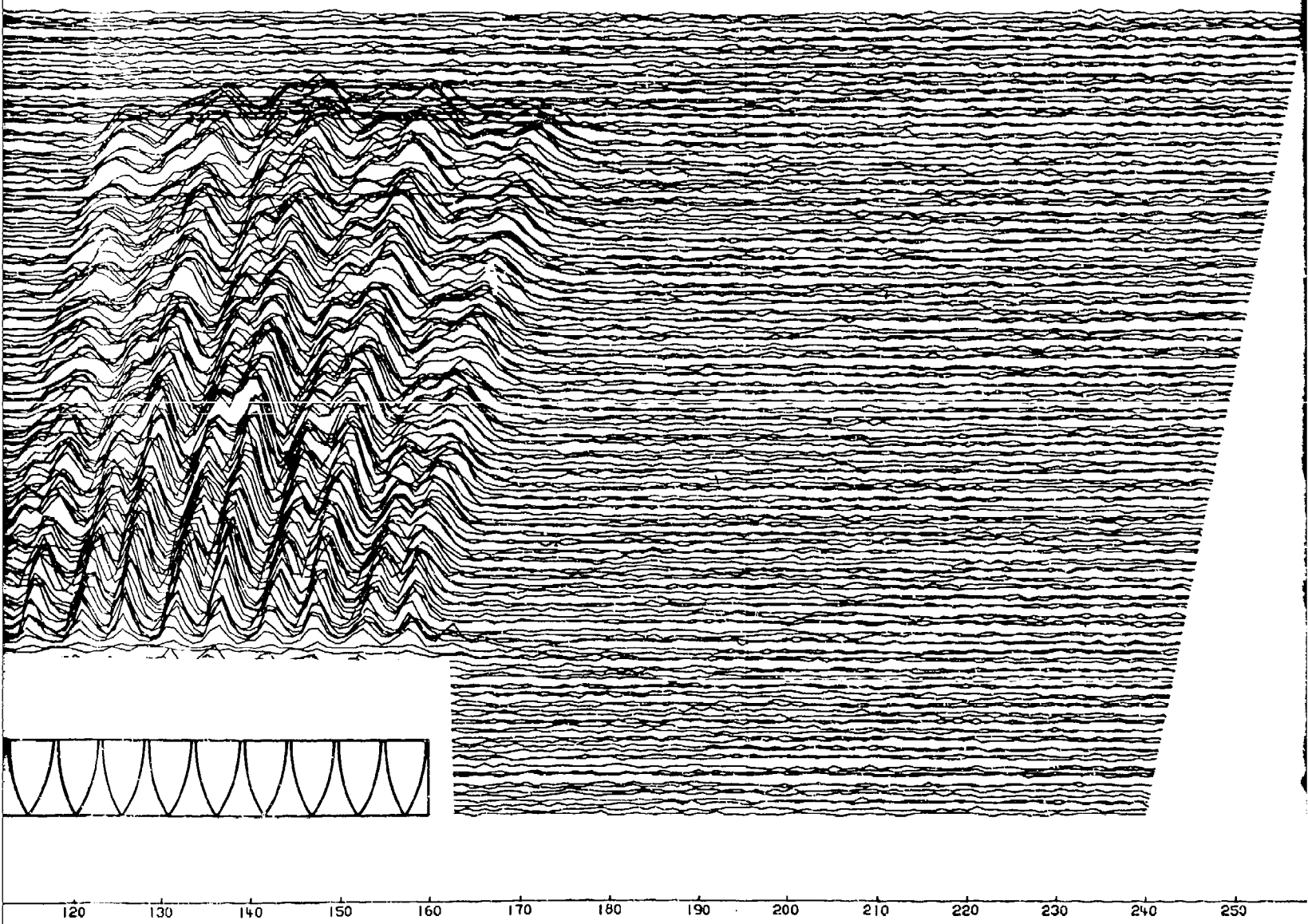

4. IR Intensity Distribution--Test 323, Set 1

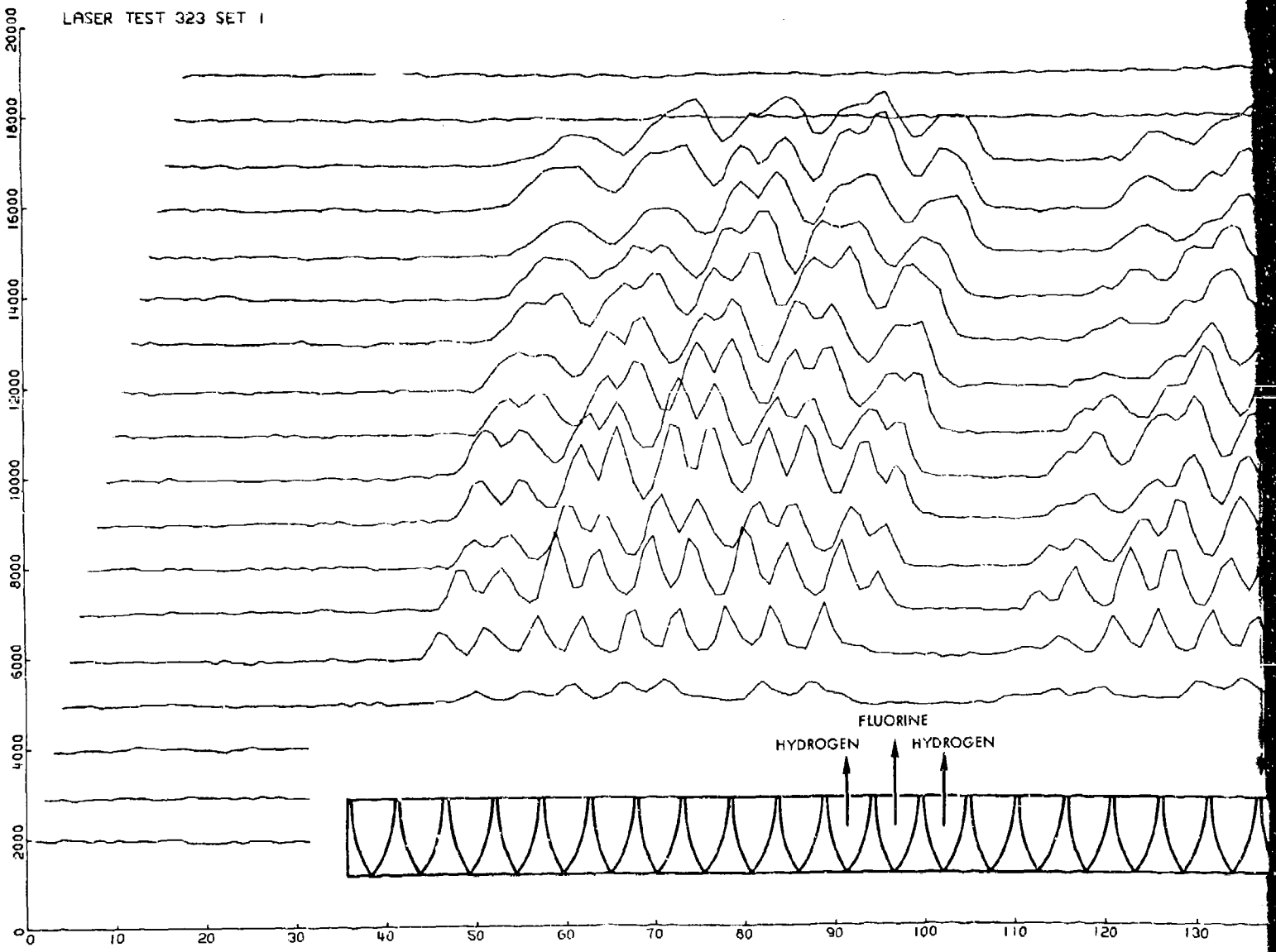

Figure 55. IR Intensity Distribution--

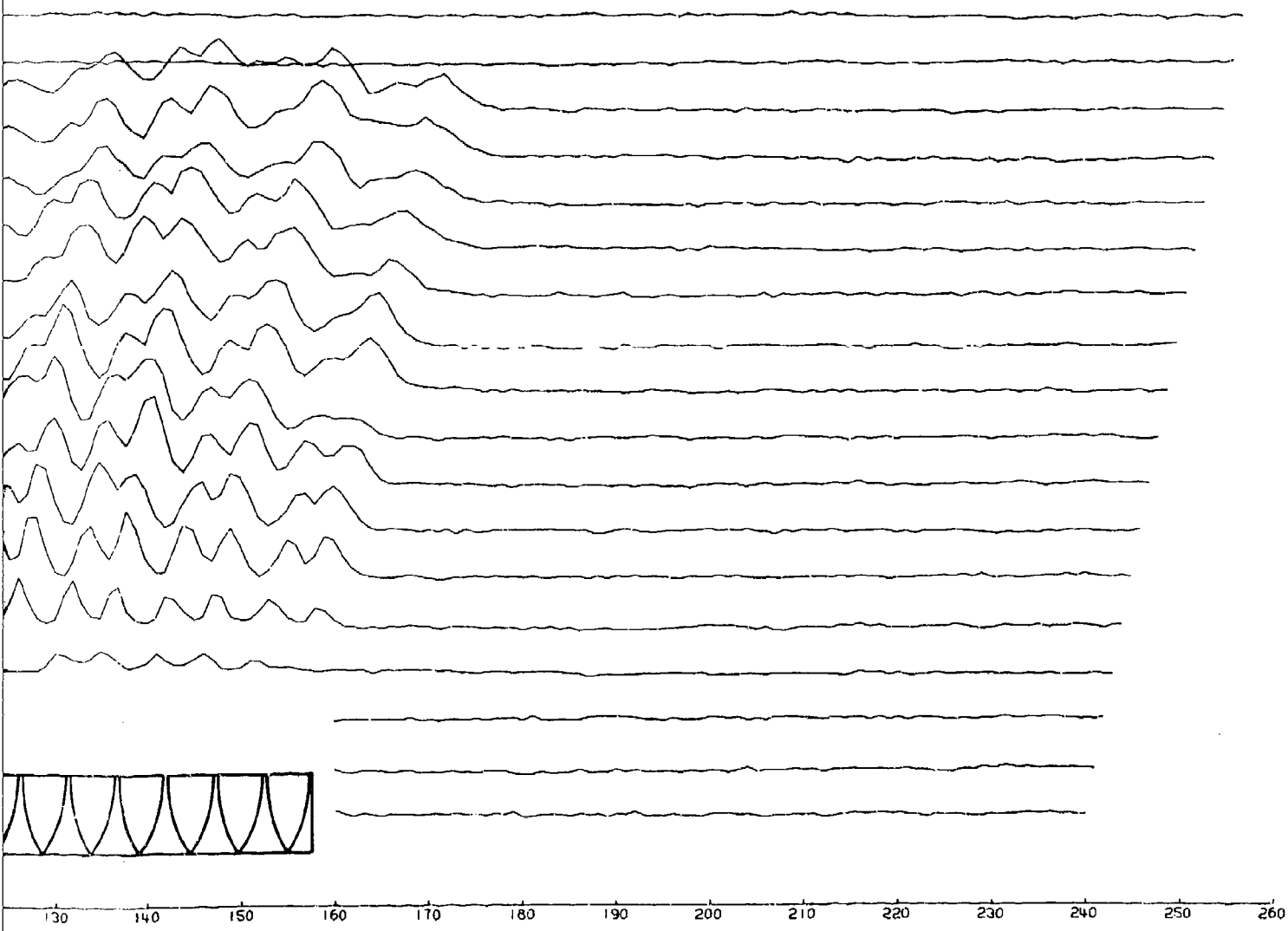

stribution--Test 323, Set 1 (every 10th scan line)

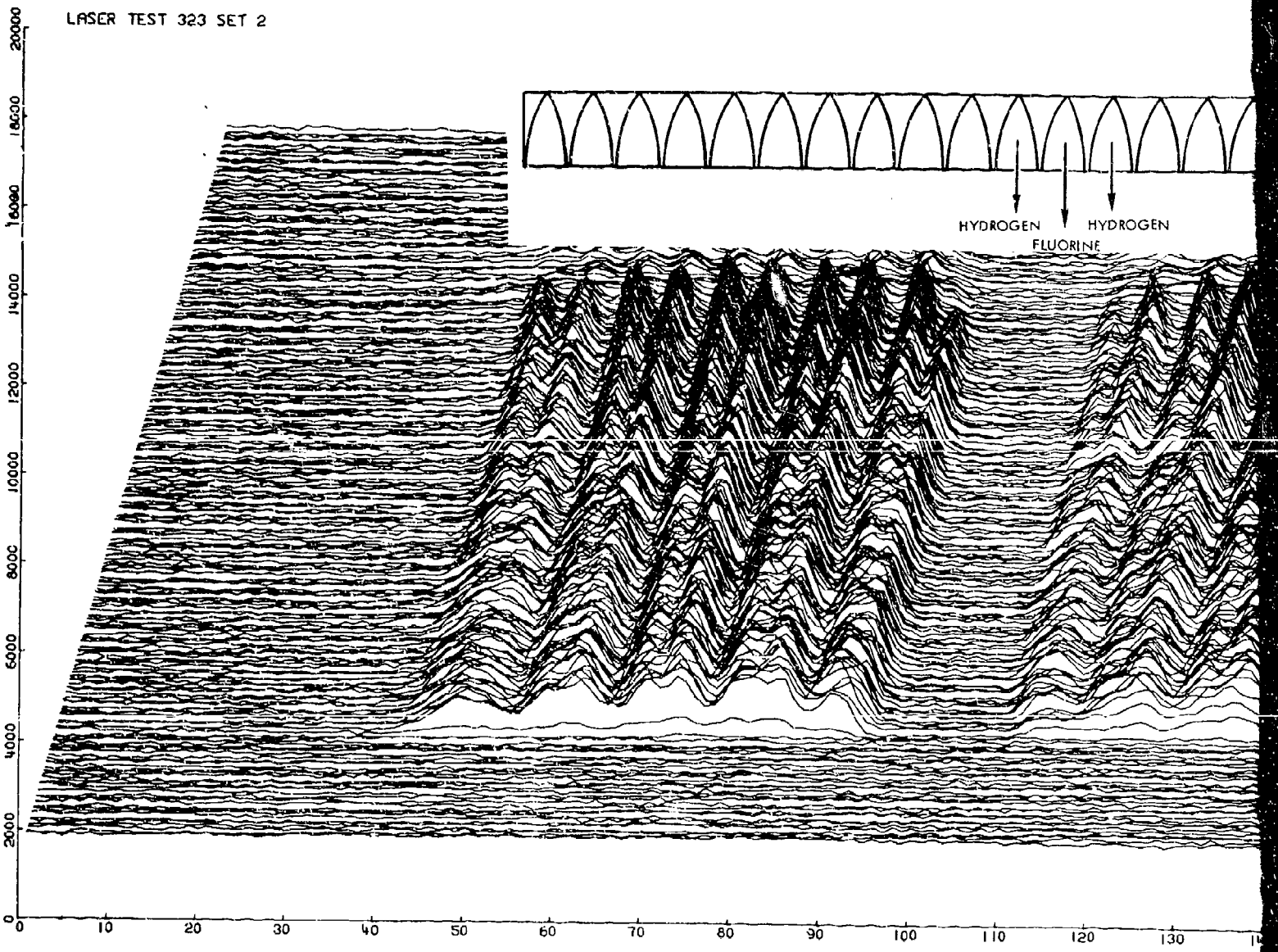

Figure 56. IR Intensity Distributio

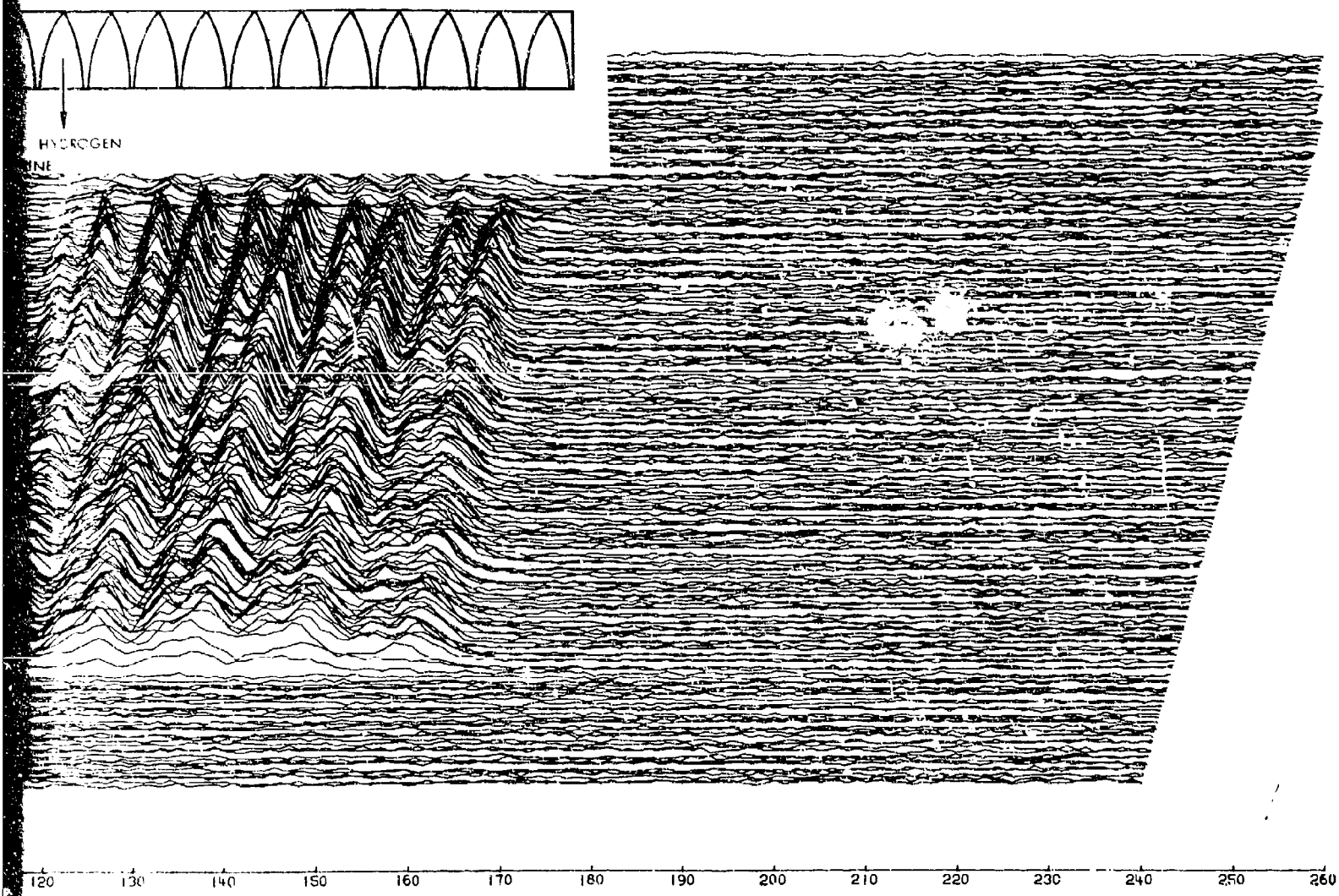

ntensity Distribution--Test 323, Set 2

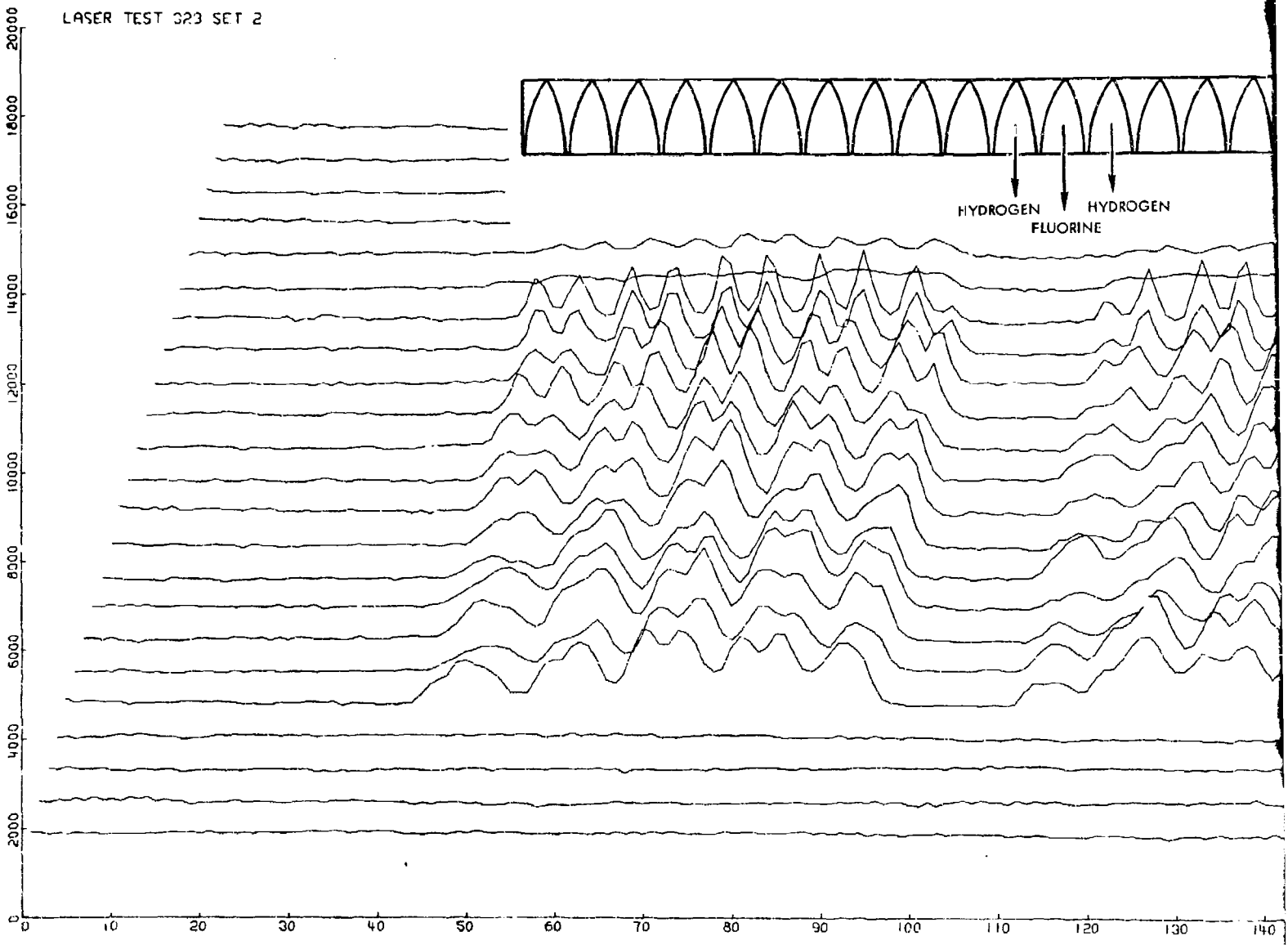

Figure 57. IR Intensity Distribution--Test

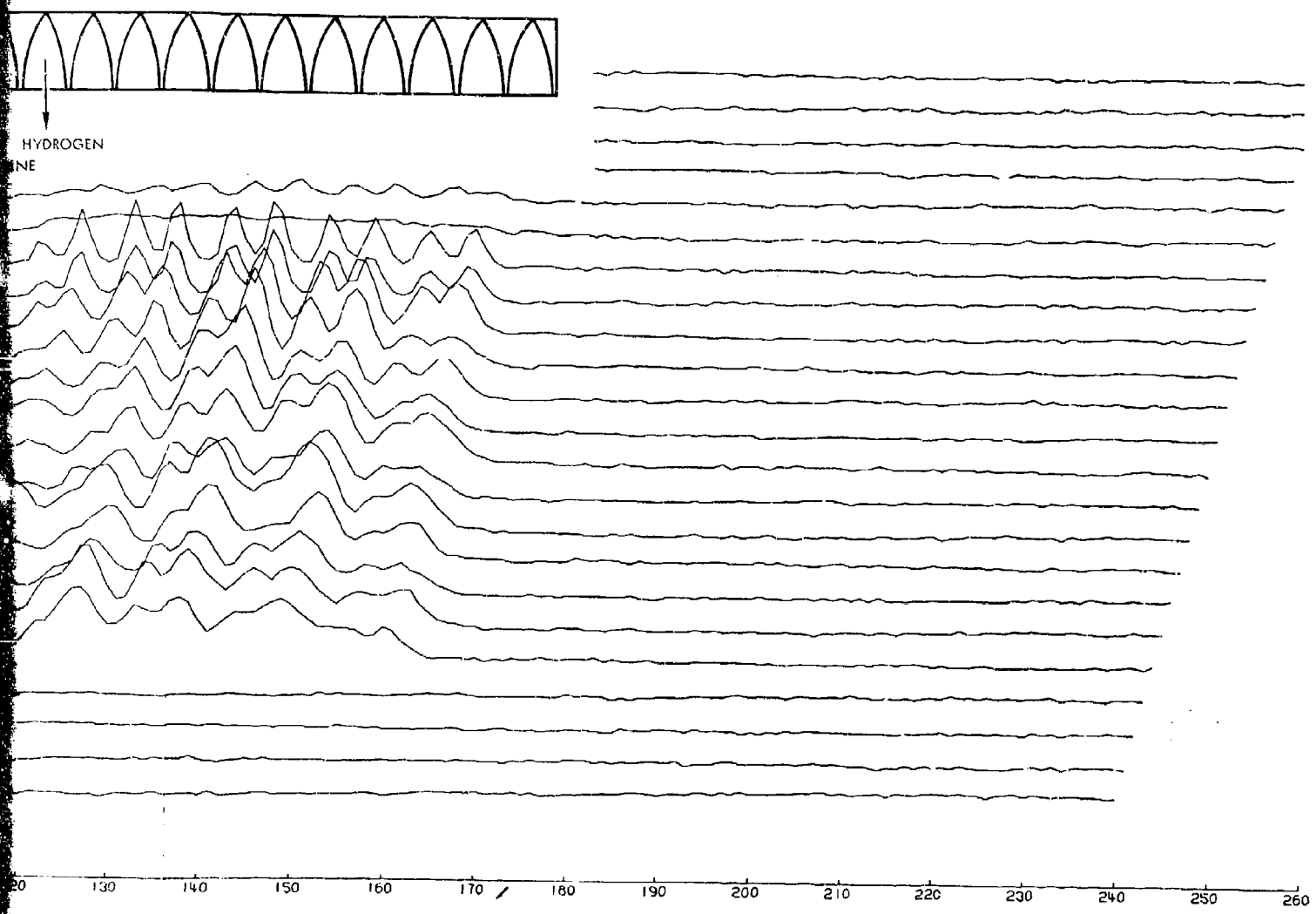

ty Distribution--Test 323, Set 2 (every 10th scan line)

2

UNCLASSIFIED
Security Classification

DOCUMENT CONTROL DATA - R & D

(Security classification of title, body of abstract and indexing annotation must be entered when the overall report is classified)

1. ORIGINATING ACTIVITY *(Corporate author)*

TRW Systems Group
Redondo Beach, California 90278

2a. REPORT SECURITY CLASSIFICATION
UNCLASSIFIED

2b. GROUP

3. REPORT TITLE

HYDROGEN FLUORIDE LASER TECHNOLOGY STUDY (CCN)

4. DESCRIPTIVE NOTES *(Type of report and inclusive dates)*
9 November 1972-9 March 1972

5. AUTHOR(S) *(First name, middle initial, last name)*
T. A. Jacobs; J. E. Broadwell; D. L. Hook; R. F. Wuerker; F. N. Mastrup

6. REPORT DATE
October 1972

7a. TOTAL NO. OF PAGES
130

7b. NO. OF REFS
21

8a. CONTRACT OR GRANT NO. F29601-71-C-0070

b. PROJECT NO. 3326

c. Task No. 6

d.

9a. ORIGINATOR'S REPORT NUMBER(S)
AFWL-TR-72-82

9b. OTHER REPORT NO(S) *(Any other numbers that may be assigned this report)*

10. DISTRIBUTION STATEMENT
Distribution limited to US Government agencies only because test and evaluation information is discussed in the report (Oct 72). Other requests for this document must be referred to AFWL (LRT), Kirtland AFB, NM, 87117.

11. SUPPLEMENTARY NOTES

12. SPONSORING MILITARY ACTIVITY
AFWL (LRT)
Kirtland AFB, NM 87117

13. ABSTRACT

(Distribution Limitation Statement B)
In the course of performing the work discussed in this report, the basic feasibility of Rayleigh Scattering, Raman Scattering and Holographic Interferometry as HF/DF laser cavity diagnostic techniques was investigated. A new HF/DF chemical laser system designated CL III was designed, fabricated and underwent preliminary testing to evaluate reactant mixing of parallel, fully developed H_2 and F supersonic flows in the lasing cavity and scaling to higher power while maintaining good potential for pressure recovery.

DD FORM 1 NOV 65 1473

UNCLASSIFIED
Security Classification

UNCLASSIFIED
Security Classification

14. KEY WORDS	LINK A ROLE	LINK A WT	LINK B ROLE	LINK B WT	LINK C ROLE	LINK C WT
Combustion-driven HF/DF chemical laser						
Chemical laser diagnostic techniques						
Chemical laser supersonic mixing and reaction						

UNCLASSIFIED
Security Classification